KARADENİZ TECHNICAL UNIVERSITY
THE GRADUATE SCHOOL OF NATURAL AND APPLIED SCIENCES

DEPARTMENT OF CIVIL ENGINEERING

STATIC, DYNAMIC AND STABILITY ANALYSIS OF FUNCTIONALLY GRADED SANDWICH BEAMS WITH POROUS CORE RESTING ON ELASTIC FOUNDATION

DOCTORATE THESIS

Ibrahim ALI MOHAMED

MARCH 2025
TRABZON

KARADENİZ TECHNICAL UNIVERSITY

THE GRADUATE SCHOOL OF NATURAL AND APPLIED SCIENCES

DEPARTMENT OF CIVIL ENGINEERING

STATIC, DYNAMIC AND STABILITY ANALYSIS OF FUNCTIONALLY GRADED SANDWICH BEAMS WITH POROUS CORE RESTING ON ELASTIC FOUNDATION

Ibrahim ALI MOHAMED

This thesis is accepted to give the degree of

DOCTOR OF PHILOSOPHY

By

The Graduate School of Natural and Applied Sciences at
Karadeniz Technical University

The Date of Submission : **10 / 02 /2025**

The Date of Examination : **03 / 03 /2025**

Thesis Supervisor : **Prof. Dr. Volkan KAHYA**

Trabzon 2025

KARADENİZ TECHNICAL UNIVERSITY

THE GRADUATE SCHOOL OF NATURAL AND APPLIED SCIENCES

DEPARTMENT OF CIVIL ENGINEERING

Ibrahim ALI MOHAMED

STATIC, DYNAMIC AND STABILITY ANALYSIS OF FUNCTIONALLY GRADED SANDWICH BEAMS WITH POROUS CORE RESTING ON ELASTIC FOUNDATION

Has been accepted as a thesis of

DOCTOR OF PHILOSOPHY

after the Examination by the Jury Assigned by the Administrative Board of the Graduate School of Natural and Applied Sciences with the Decision Number 2090 dated 12 / 02 / 2025

Approved By

Chairman	**:**	**Prof. Dr. Kurtuluş SOYLUK**	……..……..……
Member	**:**	**Prof. Dr. Volkan KAHYA**	……..……..……
Member	**:**	**Prof. Dr. Hasan GEDİKLİ**	……..……..……
Member	**:**	**Prof. Dr. İsa ÇÖMEZ**	……..……..……
Member	**:**	**Prof. Dr. Murat YAYLACI**	……..……..……

Prof. Dr. Asim KADIOĞLU

Director of Graduate School

PREFACE

This dissertation has been prepared as part of the requirements for a PhD degree at the Graduate School of Natural and Applied Sciences, Department of Civil Engineering. I owe my deepest gratitude to my esteemed advisor, Prof. Dr. Volkan KAHYA, for his unwavering support, insightful guidance, and continuous encouragement throughout my PhD journey. His expertise and dedication have been instrumental in shaping this research and bringing it to fruition.

I extend my heartfelt thanks to my esteemed professors, colleagues, and friends at Karadeniz Technical University, particularly within the Department of Civil Engineering. Their intellectual contributions, stimulating discussions, and support have enriched this study and made this journey a fulfilling experience.

Finally, my deepest appreciation goes to my beloved family and cherished loved ones. Their unconditional love, patience, and unwavering belief in me have been my anchor throughout this journey. This dissertation would not have been possible without their encouragement, understanding, and steadfast support.

I hope this research will contribute meaningfully to the field of civil engineering and serve as a foundation for further advancements in this area.

Ibrahim ALI MOHAMED

Trabzon 2025

THESIS STATEMENT

I hereby declare that I have completed this study, titled *"*Static, Dynamic, and Stability Analysis of Functionally Graded Sandwich Beams with Porous Core Resting on Elastic Foundation*"*, submitted as my PhD dissertation, under the supervision of my advisor Prof. Dr. Volkan KAHYA from start to finish. I confirm that I independently collected the data/samples, conducted the experiments/analyses in the relevant laboratories, and have fully cited and referenced information obtained from other sources within the text and bibliography. I also declare that I have adhered to scientific research and ethical principles throughout the study and accept all legal consequences should any violations be revealed. 03/03/2025

Ibrahim ALI MOHAMED

TABLE OF CONTENTS

Ph.D. Thesis

SUMMARY

STATIC, DYNAMIC, AND STABILITY ANALYSIS OF FUNCTIONALLY GRADED SANDWICH BEAMS WITH POROUS CORE RESTING ON ELASTIC FOUNDATION

Ibrahim ALI MOHAMED

Karadeniz Technical University
The Graduate School of Natural and Applied Sciences
Civil Engineering, Graduate Program
Supervisor: Prof. Dr. Volkan KAHYA
2025, 142 Pages

This thesis presents a comprehensive study of static, dynamic, and stability analyses of functionally graded sandwich beams (FGSBs) with porous core resting on a Winkler-Pasternak elastic foundation. The research focuses on the free vibration, buckling, and bending characteristics of FGSBs with three different core configurations: porous ceramic core, metallic core, and functionally graded (FG) porous core. A power-law distribution is used to model the gradual variation of material properties across the thickness, considering three distinct porosity patterns: uniform, symmetric, and asymmetric. A general theoretical formulation is derived from a quasi-3D deformation theory. The governing equations of motion are obtained using Hamilton's principle and Lagrange's equations. Analytical models, formulated using the Navier and Ritz methods, are complemented by a novel three-node higher-order finite element model. Additionally, a novel FGSB modeling technique is presented using Ansys Mechanical APDL. The accuracy and efficiency of these quasi-3D models are demonstrated and validated through comparisons with existing literature. The study explores the effects of material property homogenization schemes, transverse normal deformation, boundary conditions, structural configurations, porosity characteristics, and foundation parameters on natural frequency, critical buckling, bending, and stress responses. The findings reveal that the introduction of porosity into the core of FGSBs significantly influences their mechanical behavior, with symmetric porosity configurations resulting in superior performance.

Keywords: FG sandwich beams; Quasi-3D theory; Porosity; Elastic foundation; Statics; Free vibration; Buckling; Navier's method; Ritz method; Finite element method; Ansys

Doktora Tezi

ÖZET

ELASTİK TEMEL ÜZERİNE OTURAN GÖZENEKLİ ÇEKİRDEKLİ FONKSİYONEL DERECELENDİRİLMİŞ SANDVİÇ KİRİŞLERİN STATİK, DİNAMİK VE STABİLİTE ANALİZİ

Ibrahim ALI MOHAMED

Karadeniz Teknik Üniversitesi
Fen Bilimleri Enstitüsü
İnşaat Mühendisliği Anabilim Dalı
Danışman: Prof. Dr. Volkan KAHYA
2025, 142 Sayfa

Bu tez, Winkler-Pasternak elastik zemin üzerine otuıran ve gözenekli çekirdeğe sahip fonksiyonel derecelendirilmiş (FD) sandviç kirişlerin statik, dinamik ve stabilite analizine ilişkin kapsamlı bir çalışma sunmaktadır. Araştırma, kirişin serbest titreşim, burkulma ve eğilme özelliklerini inceleyerek, üç farklı çekirdek yapılandırması (gözenekli seramik çekirdek, metal çekirdek ve FD gözenekli çekirdek) için bu davranışları etkileyen temel parametrelerin anlaşılmasını sağlamayı amaçlamaktadır. Malzeme özelliklerinin yükseklik boyunca kademeli değişiminin modellemesinde kuvvet yasası dağılımı kullanılmış olup, üç farklı gözeneklilik deseni (uniform, simetrik ve asimetrik) dikkate alınmıştır. Yer değiştirme alanı hem enine kayma hem de normal deformasyonlarını göz önünde bulundurmaktadır. Hareket denklemleri, Hamilton prensibi ve Lagrange denklemleri kullanılarak türetilmiştir. Navier ve Ritz yöntemleriyle formüle edilen analitik modeller, yenilikçi üç düğümlü yüksek mertebeden sonlu eleman modeli ile desteklenmiştir. Ayrıca, Ansys Mechanical APDL kullanılarak yeni bir FD sandviç kiriş modelleme tekniği sunulmuştur. Doğruluğu ve etkinliği mevcut literatürle yapılan karşılaştırmalarla gösterilmiş ve doğrulanmıştır. Çalışma, malzeme özelliklerinin homojenleştirilmesi yaklaşımları, enine normal deformasyon, sınır koşulları, yapısal konfigürasyonlar, gözeneklilik özellikleri ve diğer temel parametrelerin doğal frekans, kritik burkulma yükü ve statik yer değiştirme ve gerilmeler üzerindeki etkilerini araştırmaktadır. Bulgular, FD sandviç kiriş çekirdeğine gözeneklilik eklenmesinin mekanik davranışı önemli ölçüde etkilediğini.

Anahtar Kelimeler: FD sandviç kiriş; Yarı-3D teori; Gözeneklilik; Elastik zemin; Statik analiz; Serbest titreşim; Burkulma; Navier yöntem; Ritz yöntem; Sonlu eleman yöntem; Ansys

LIST OF FIGURES

Page No

LIST OF TABLES

Page No

LIST OF SYMBOLS

e_0	:	Porosity coefficient
e_m	:	Mass density
$f(z)$	:	Shear shape function
h	:	Thickness
k_{w}	:	Winkler constant
k_p	:	Pasternak constant
p	:	Power index
$q(x)$	:	Transverse load
$u(x,z,t)$	:	Displacement in x-direction
$w(x,z,t)$	:	Displacement in z-direction
$\bar{w}$	:	Nondimensional vertical displacement
$E(z)$	:	Elastic modulus
$\mathbf{F}$	:	Force
$\mathbf{G}$	:	Geometric stiffness matrix
K	:	Kinetic energy
K_w	:	Nondimensional Winkler constant
K_p	:	Nondimensional Pasternak constant
$\mathbf{K}$	:	Stiffness matrix
L	:	Length
$\mathbf{M}$	:	Mass matrix
N_0	:	Axial force
$\overline{N}_{cr}$	:	Nondimensional critical buckling load
U	:	Strain energy
U_F	:	Strain energy induced by elastic foundations
V	:	Potential energy
$V_c(z)$	:	Volume fraction
δ	:	Variational operator
ε	:	Strain
$\rho(z)$	:	Mass density

σ	:	Stress
$\bar{\sigma}$	:	Nondimensional stress
τ	:	Shear stress
υ	:	Poisson's ratio
$\varphi_i(x)$	:	Shape function
ϕ	:	Slope
$\psi_i(x)$	:	Shape function
ω	:	Natural frequency
$\bar{\omega}$	:	Nondimensional natural frequency
$\boldsymbol{\Delta}$	:	Vector of unknown coefficients.
Π	:	Total potential energy

1. GENERAL INFORMATION

1.1. Overview

The industrial world is in a state of constant evolution driven by the quest for perfection. This progression and pursuit for excellence cannot be realized without scientific advancement, which provides industry with cutting-edge research outcomes, facilitating the conception and implementation of innovative processes that drive industrial development. Historically, the driving force behind the discovery of new materials has largely adhered to a dual paradigm associated with the pragmatic challenges humans face in their material existence, and their intellectual imperative to comprehend and elucidate the world around them. Consequently, a significant subset of materials has been engineered to address specific technological exigencies.

The necessity to discover or synthesize novel materials has intensified significantly with the progression of scientific knowledge and technological advancement, driving the transformation of materials from monolithic forms to alloys, and subsequently, to the creation of composite materials. Composite materials are an innovative class of materials formed by combining two or more distinct substances, each with unique properties. This combination allows the composite to leverage the best characteristics of its components, resulting in improved overall performance. Conventional composites are typically composed of multiple layers bonded together at interfaces with fiber orientations that can be tailored to achieve desired structural performance characteristics. This tailoring leads to improved properties, such as enhanced stiffness, improved fatigue and corrosion resistance, increased wear resistance, and weight reduction. However, a significant challenge associated with conventional composite materials is the presence of discontinuities at the layer interfaces, leading to stress concentrations, matrix cracking, debonding, and delamination, particularly under elevated temperature conditions.

In the quest to overcome the limitations of conventional composites, engineers and researchers have directed their attention toward functionally graded materials (FGMs). Initially proposed by Japanese scientists in 1984 these new-generation inhomogeneous advanced composite materials are featured with gradual and continuous change in the characteristics of their constituent elements along a specified axis. Unlike traditional

composites with sharp interfaces, FGMs feature gradient interfaces, enabling a smooth transition between different materials and mitigating interfacial effects. This unique property of FGMs minimizes stress concentrations, residual stresses, matrix cracking, debonding, and delamination, thereby enhancing structural durability and preventing catastrophic failures. FGMs are often crafted from a combination of ceramics and metals, leveraging the strengths of both materials. This ingenious pairing capitalizes on the ceramics' excellent thermal properties, wear resistance, and corrosion resilience, while simultaneously harnessing the superior toughness and mechanical strength inherent to metals. Consequently, they offer significant potential in high-temperature environments and sensitive applications.

The evolution of FGMs has led to the emergence of functionally graded porous materials (FGPMs), which incorporate porosity into the material gradient. In addition to the benefits of typical FGMs, FGPMs have important characteristics such as being lightweight, possessing high strength, demonstrating superior energy dissipation, and enhancing thermal and acoustic characteristics. These attributes have sparked interest in their potential applications across various engineering sectors such as civil, aerospace, automotive, energy, and environmental engineering. The pursuit of enhanced performance has driven the development of various advanced beam structures, including functionally graded porous (FGP) beams, FGP sandwich beams, and functionally graded sandwich beams (FGSBs) with porous cores.

Their numerous advantages have attracted significant research interest over the past few decades, resulting in extensive studies on their mechanical behaviors utilizing a range of displacement-based theories including classical beam theory (CBT), first-order shear deformation theory (FSDT), higher-order shear deformation theories (HSDTs), and quasi-3D deformation theories. Although CBT provides a simple method for beam analysis, its omission of transverse shear deformation limits its accuracy to slender beams. To address the limitations of CBT, Timoshenko proposed the FSDT in 1921. The FSDT model considers shear deformation effects, offering more precise outcomes for thick beams in contrast to CBT. However, the utilization of a suitable shear correction factor is imperative in FSDT to adequately account for transverse shear deformation. To eliminate the necessity for the shear correction factor, HSDTs have been introduced. Furthermore, quasi-3D deformation theories, developed as an extension of HSDTs, incorporate thickness-stretching effects, leading to enhanced accuracy.

The computational approaches employed to predict the beam behavior can be categorized into analytical and numerical methods. Among the analytical approaches, Navier's method stands out as the simplest and most well-established analytical technique. However, its applicability and effectiveness are limited to boundary conditions. To overcome the limitations of the Navier approach, the Ritz method has emerged as an alternative analytical technique that can account for various BCs. The precision of this technique, however, relies on the appropriate selection of the approximate shape functions. Due to the limitations of analytical methods, numerical techniques have gained prominence, with the finite element method (FEM) establishing itself as the preeminent computational approach.

This section presents a comprehensive overview of FGMs and FGPMs. An extensive review of recent literature on the mechanical behavior of FGP beams and FGP sandwich beams is presented, revealing the growing interest in such structures and the diverse range of studies conducted on their static, dynamic, and stability behaviors. The review identifies significant research gaps, including the limited application of the Ritz method and FEM solutions based on HSNDTs in FGSBs analysis. It also emphasizes the need for further research on FGSBs with porous cores on elastic foundations. The chapter provides an overview of displacement-based theories, including CBT, FSDT, HSDT, and quasi-3D models, employed in FGSBs analysis. It also evaluates analytical approaches such as Navier and Ritz methods, numerical techniques like FEM, and elastic foundation models used in conjunction with these theories.

1.2. Literature Review

1.2.1. Review of Mechanical Analysis of FGP Beams

FGP beams have been widely studied due to their potential for improved mechanical performance in various engineering applications. The literature includes extensive analyses of static bending, buckling, and vibration behaviors, with researchers utilizing diverse deformation theories and solution methods. This section synthesizes key contributions from recent studies, highlighting the progression of knowledge and gaps in understanding.

Early studies predominantly employed Timoshenko beam theory (TBT) and FSDT to model mechanical behavior. Ton (2022) and To (2022) examined the influence of porosity

distributions on the bending and free vibration behaviors of FGP beams using FEM based on TBT. Building upon this, Chen et al. (2022) expanded the scope by investigating buckling and vibration behaviors using multiscale modeling with the Ritz method and TBT. Focusing on FSDT, Van Vinh et al. (2022) introduced a novel mixed FE model to analyze the bending behavior of FGP beams, while Akbaş et al. (2022) used FEM to analyze the vibration response of thick FGP beams under dynamic sine pulse loads Subsequent studies explored dynamic responses and viscoelastic effects in FGP beams. Medjdoubi et al. (2023) developed an analytical model to look into the effect of porosity on the shear correction factors. Ong et al. (2023) studied the vibrational response of viscoelastic FGP carbon nanotube (CNT) reinforced double beams using FEM and FSDT. Zhang et al. (2023) introduced a unified variational method based on FSDT for analyzing the vibration of FGP beams with variable curvature under arbitrary boundary conditions. In a related direction, Chen et al. (2023) conducted structural uncertainty analysis on FGP beams using AI-enhanced FE multiscale modeling with TBT and the Ritz method, while Turan et al. (2023) investigated the free vibration and buckling behaviors of FGP beams using the Ritz method, FEM, and artificial neural networks with FSDT, complementing earlier findings on porosity effects. Similarly, Fallah et al. (2024) used physics-informed neural networks to analyze the bending and free vibration of three-dimensional (3D) FGP beams. Uzun et al. (2024) explored the vibrational behavior of carbon nanobeam on an elastic foundation, considering various gradation rules. Burlayenko et al. (2024) focused on modal characteristics of FGP beams with variable cross-sections using the differential transform method and TBT. Belabed et al. (2024) formulated a novel beam FE model to investigate the buckling and free vibration behavior of FGP beams supported by elastic foundations. Vikrant and Sarangi (2024) explored the elastic buckling and static bending of FGP beams with varying porosity distributions under different conditions. Rasooli et al. (2024) presented a novel method using complementary functions to analyze the static behavior of FGPB-column frames using TBT. Bagheri et al. (2024), examined the impact of porosity on the free vibration and buckling of non-uniform FGP beams using FSDT. Wu et al. (2024) compared beam theories for predicting buckling and vibration of FGP beams. Heshmati et al. (2024) carried out a time-domain analysis of wave propagation in FGP beams using FSDT. Ahmed et al. (2024) introduced a novel analytical model to study the impact of porosity on shear correction factors in FGP beams. These studies collectively

demonstrated a progressive refinement in understanding the mechanical behavior of FGP beams.

As research progressed, HSDTs emerged as effective tools for precise analysis of FGP beams, addressing the limitations of lower-order theories. Initial studies by Fazzolari (2018) explored the free vibration and elastic stability of 3D-FGP sandwich beams on Winkler-Pasternak foundations. Su et al. (2019) used third-order shear deformation theory (TSDT) in investigating the impact of surface on the bending behavior of FGP nanobeams. Hadji et al. (2019) developed a novel HSDT model for analyzing the bending and vibration behaviors of FGP beams with the Navier method, providing a robust framework for later works. Harsha et al. (2021) employed the Ritz method to investigate the influence of porosity distributions on the buckling and vibration behavior of FG beams under axially variable loads (AVLs), while Priyanka et al. (2022) extended this by focusing on AVL effects in FGP beams using the same method. Zghal et al. (2022) utilized enhanced mixed FEM to study the effects of porosity distributions on the static bending characteristics of FGP beams. Sayyad et al. (2022) applied the Navier method with HSDT to evaluate circular FGP beams' mechanical responses, advancing earlier models by addressing more complex geometries. Adıyaman (2022) performed free vibration analysis using FEM and HSDT, refining the understanding of FGP beam dynamic characteristics. Nguyen et al. (2022) introduced two-variable shear deformation theory for comprehensive buckling, bending, and vibration analyses. Mellal et al. (2023) extended these by studying the vibration and buckling of FGP beams on variable foundations using the HSDT and Navier technique. Pham et al. (2023) studied the vibration of 2D-FGP nanobeams on elastic foundations under hygrothermal conditions using nonlocal strain gradient theory-based FEM. Hadji et al. (2023) analyzed bending and free vibration responses of FGP beams using HSDT and Navier methods, focusing on elastic foundation effects. Nguyen et al. (2023) developed a Legendre-Ritz method to study FGP beams' mechanical characteristics on elastic foundations, demonstrating the versatility of HSDT. Abdelbari et al. (2023) explored free vibration of imperfect FGP beams on Winkler-Pasternak foundations under thermal loading using HSDT. Turan and Adiyaman (2023) analyzed the static response of 2D-FGP beams with HSDT, while Geetha et al. (2023) presented a Navier-type analytical model based on HSDT for analyzing the bending response of 2D-FGP beams, considering various porosity distributions and material property modifications along its dimensions Geetha et al. (2023) performed numerical vibrational analysis on FGP beams using a TSDT

under various boundary conditions., with Dahmane et al. (2023) exploring wave propagation in bidirectional FGP beams using HSDT. Attia and Shanab (2024) integrated surface stress and microstructure effects into 2D-FGP nanobeam dynamics with the Ritz method and HSDT, while Kannaiyan et al. (2024) employed the Kuhn-Tucker technique for vibrational studies using TSDT and R-program. Similarly, Adıyaman and Turan (2024) carried out the bending and buckling of exponentially 2D-FGP beams using HSDT. Djebbour et al. (2024) conducted a detailed analysis of the free vibration behavior of FGP-CNT beams supported by an arbitrary orthotropic variable elastic foundation using HSDT. Uzun and Yaylı (2024) evaluated the dynamic response of FG nanobeams with pores using modified couple stress theory. Amir and Kim (2024) calculated the natural frequencies of FGP curved beams using deterministic and stochastic FE models based on HSDT. Zhang et al. (2024) addressed hygrothermal effects on FGP magneto-electro-elastic microbeams using the differential transformation method and modified couple stress theory, highlighting multi-physics integration in FGP modeling. The consistent thread throughout these studies is the use of HSDT and various numerical methods to provide an increasingly precise and nuanced understanding of FGP beam behaviors.

To enhance the predictive accuracy of FG beam behavior and account for transverse normal stresses, quasi-3D theories extend HSDTs by incorporating thickness-stretching effects through higher-order shear shape functions. Atmane et al. (2017) were among the first to apply quasi-3D theory to study the free vibration, bending, and buckling behavior of FG beams on elastic foundations. Their work highlighted the significant influence of porosity on these mechanical responses. Fahsi et al. (2019) extended the application of quasi-3D theory by introducing a new formulation to analyze the mechanical behavior of FGP beams on elastic foundations, focusing on enhanced modeling of transverse stresses. Taleb et al. (2024) further expanded the scope of quasi-3D theory by investigating the free vibration behavior of temperature-dependent 2D-FGP curved beams. These studies utilizing quasi-3D theory underscore its robustness in capturing the mechanical responses of FGP beams. Upon the understanding of FGP beams, the researchers turn their focus to FGSBs, which introduce an additional layer of complexity and potential for innovative applications due to their distinct structural configurations and material gradation.

1.2.2. Review of Mechanical Analysis of FGP Sandwich Beams

In recent decades, FGSBs with porosity have been of interest to many researchers due to their numerous advantages, leading to extensive studies focusing on their mechanical characteristics using various theories and computational methods (Wu et al., 2020b). Early studies focused on fundamental mechanical analyses using FSDT. Bamdad et al. (2019) pioneered investigations into the vibration and buckling response of FGP sandwich beams with porous cores, establishing a foundational understanding of their mechanical behavior. Building upon this groundwork, Alambeigi et al. (2020) expanded the research by incorporating shape memory alloy composite face sheets, demonstrating the potential for more sophisticated material configurations. Njim et al. (2022) and Al-Itbi and Noori (2022) further extended this work using Ansys-based simulations, quantifying the effects of porosity and material gradation on bending behavior. Taşkin and Demir (2023) further extended FSDT for curved sandwich beams with viscoelastic cores, incorporating damping effects into vibration analyses. Similarly, Mesmoudi et al. (2023) proposed an efficient mesh-free approach based on buckling and post-buckling analysis of FGP sandwich beams, while Mesmoudi et al. (2023) assessed the nonlinear response of FGP isotropic and sandwich Timoshenko beams by combining the radial point interpolation approach with variable shape parameters and high-order continuation methods.

As research progressed, scholars began exploring more advanced theoretical frameworks. HSDTs have been extensively used for detailed analyses of FGP sandwich beams, particularly for capturing shear deformation effects without the need for shear correction factors. Hung and Truong (2018) conducted a comparative study using various HSDTs to investigate free vibration of beams resting on elastic foundations, providing benchmarks for future work. The computational landscape evolved rapidly, with researchers developing increasingly sophisticated numerical methods. Matinfar et al. (2019) studied the impact of a hygrothermal environment on the static bending of a 2D-FGP sandwich beam resting on a Winkler-Pasternak foundation, utilizing layerwise theory and the Chebyshev Tau method. Chinh et al. (2021) utilized a polynomial-based point interpolation method combined with HSDT for static flexural analysis, enhancing solution accuracy for stress distribution. Srikarun et al. (2021) investigated both linear and nonlinear bending behaviors of sandwich beams with FG porous core using TSDT. Hamed

et al. (2020) applied HSDT to optimize critical buckling loads under axial loads, while Patil et al. (2023) examined bending and vibration behaviors under viscoelastic boundary conditions. Derikvand et al. (2023) advanced the application of HSDT to analyze buckling in FGSBs with porous core, emphasizing porosity distribution's influence on stability. Subsequent researchers like Li et al. (2023) utilized nonlinear FE simulations and Carrera's unified formulation to investigate the nonlinear vibration response of FGSBs with porous core in thermal environments, while Mohammadimehr (2022) focused on the buckling and free vibration characteristics of FGSBs with porous core, utilizing non-local stress-strain elasticity theory.

The most recent research demonstrates a trend toward a highly specialized and more comprehensive computational framework for analyzing FGP sandwich beams with quasi-3D theory accounting for thickness stretching effects. Fang et al. (2019) employed quasi-3D theory-based isogeometric analysis to study bending and vibration behaviors, demonstrating the theory's capability for complex geometries. Hung et al. (2022) explored free vibration under thermal effects using quasi-3D theories in a mesh-free framework. Xin and Kiani (2023) employed quasi-3D theory and the Navier solution method to analyze the vibration behavior of thick sandwich beams featuring FG porous core and resting on elastic foundations. Eiadtrong et al. (2024) utilized quasi-3D theory with the Gram-Schmidt-Ritz method, while Ermis et al. (2024) developed innovative techniques using peridynamic differential operators and refined zigzag theory. These studies reveal a clear trajectory of increasing complexity and precision in understanding FGP sandwich beam mechanics. However, several critical gaps persist in the current literature, necessitating further exploration to address these challenges comprehensively.

1.2.3. Research Gaps

The comprehensive literature survey summarized above reveals significant research gaps in the characterization and analysis of FGSBs with porosity, specifically in the following key areas:

1. While HSDTs predominate current research, analytical and numerical solutions based on higher-order shear and normal deformation theories (HSNDTs) are scarce.

2. Navier's method is commonly employed for analytical solutions, however, the application of the Ritz method within the HSNDT framework remains limited.
3. The implementation of FEM using HSNDTs is restricted due to difficulties in satisfying C^1-continuity requirements, especially for complex problems.
4. Despite significantly considerable research on single-layer FG porous beams, there is a dearth of studies on FGSBs comprising FG face sheets with isotropic porous cores, or isotropic face sheets with FG porous cores. The effect of porosity on the strength and stiffness of FGMs, particularly in sandwich structures, is not well understood and requires further investigation.
5. There is limited research on the performance of sandwich beams supported by elastic foundations. Most studies utilize the Winkler foundation model, however, more comprehensive models are scarcely explored.
6. A limited number of studies have concentrated on FGSBs with porous cores resting on elastic foundations. A comprehensive understanding of the combined impacts of core porosity and elastic foundations on mechanical behavior necessitates further investigation, including shear and normal deformation effects.

1.3. Theoretical Background

1.3.1. Materials Gradation Laws

Several homogenization laws have been proposed to effectively model the gradual change in material properties of FGMs. Among them, the power law, exponential law, and sigmoid law are the most frequently employed to characterize the volume fractions of constituent materials in FGMs, as noted in the most recent reviews by Sayyad and Ghugal (2019b). This section explores the application of the most widespread and popular analytical homogenization for modeling FGSBs which is the power law. To illustrate these rules, a three-layered FGSB is considered as seen in Figure 1. This beam, composed of ceramic and metal materials with continuous variation through the thickness, is examined in three configurations: Type A features FG face layers with a homogeneous ceramic core, Type B consists of FG face layers with a homogeneous metal core, and Type C made of homogeneous face layers and an FG core.

(a) Power-law distribution. The material gradation in FGMs is commonly modeled using the rule of mixtures, a straightforward and popular approach. It assumes the property of an FGM is approximately a volume-weighted average of its constituent materials' properties. Among them, the power-law distribution, initially proposed by Wakashima et al. (1990) has become a popular choice among researchers for modeling and analyzing FG structures due to its flexibility and relative simplicity. The effective material properties of an FGSB throughout its thickness can be explicitly characterized by (Avcar et al., 2021):

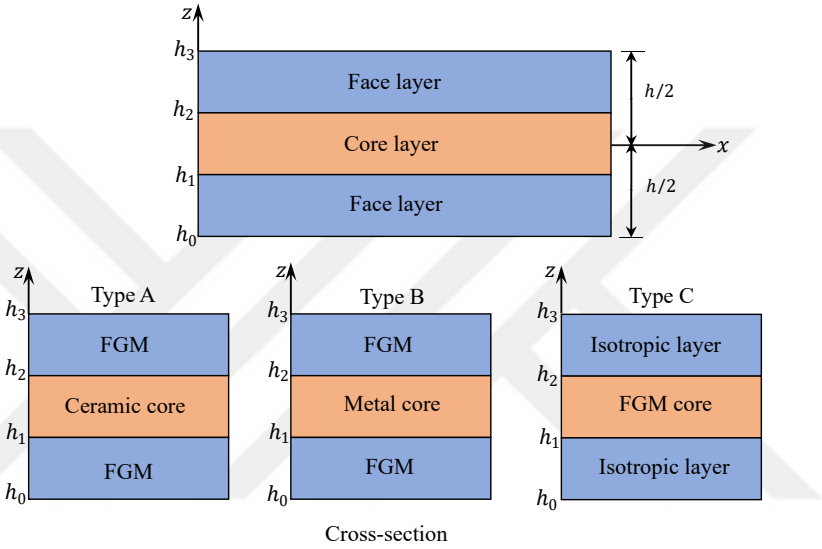

Figure 1. FG sandwich beams layout

(i) For Type A and Type C,

$$E(z) = E_m + (E_c - E_m)V_c(z)$$
$$\rho(z) = \rho_m + (\rho_c - \rho_m)V_c(z) \quad (1)$$

(ii) For Type B,

$$E(z) = E_c + (E_m - E_c)V_c(z)$$
$$\rho(z) = \rho_c + (\rho_m - \rho_c)V_c(z) \quad (2)$$

In Eqs. (1) and (2), the Young's modulus and density of the material are represented by $E(z)$ and $\rho(z)$, with subscripts m and c denoting the metal and ceramic components,

respectively. The expressions for the volume fraction which represented by $V_c(z)$ are as follows (Avcar et al., 2021):

(i) For Types A and B,

$$V_c(z) = \left(\frac{z-h_0}{h_1-h_0}\right)^p \text{ for } z \in [h_0, h_1]$$
$$V_c(z) = 1 \text{ for } z \in [h_1, h_2] \tag{3}$$
$$V_c(z) = \left(\frac{z-h_3}{h_2-h_3}\right)^p \text{ for } z \in [h_2, h_3]$$

(ii) For Type C,

$$V_c(z) = 0 \text{ for } z \in [h_0, h_1]$$
$$V_c(z) = \left(\frac{z-h_1}{h_2-h_1}\right)^p \text{ for } z \in [h_1, h_2] \tag{4}$$
$$V_c(z) = 1 \text{ for } z \in [h_2, h_3]$$

where p is the power-law index. Figure 2 provides a visual representation of volume variation for four symmetric configurations of the Type A FGSBs.

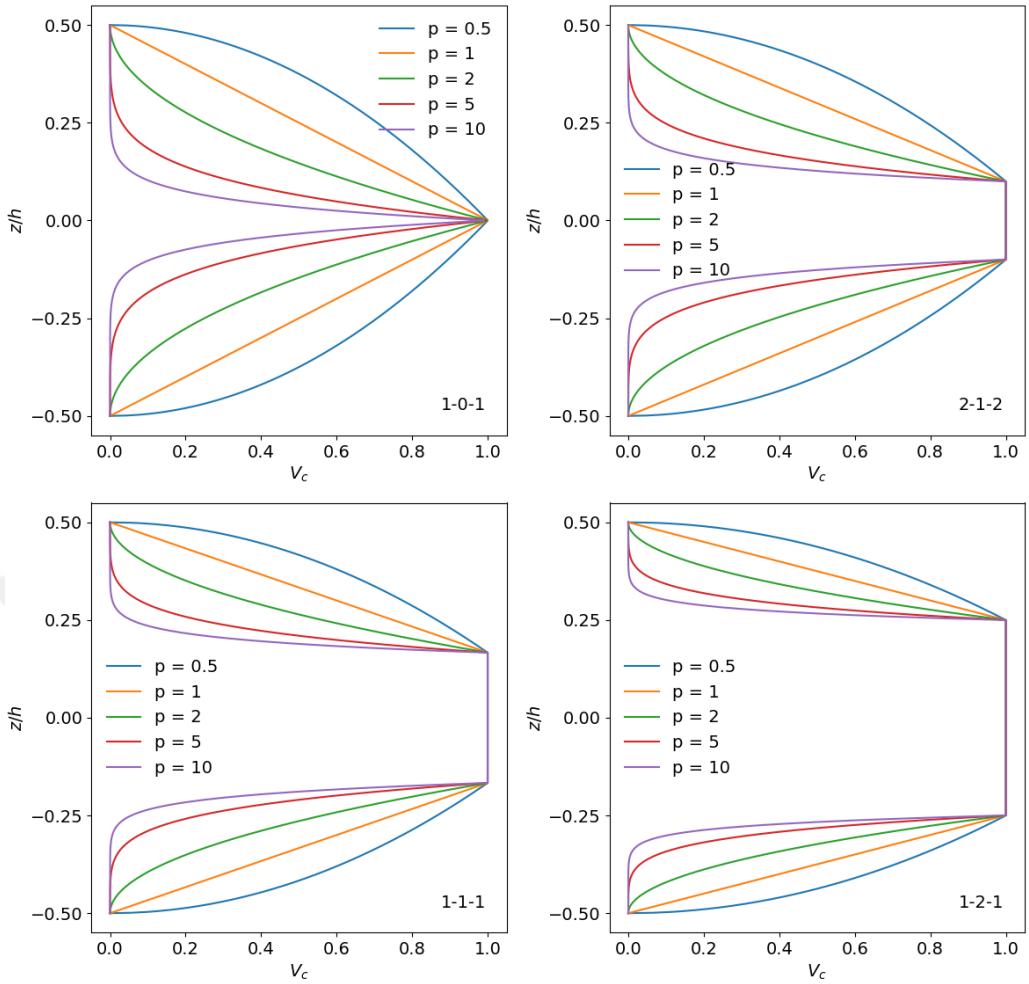

Figure 2. Volume fraction distribution for Type A beams with respect to the power-index

(b) Exponential distribution law. The exponential law has gained significant attention in studies focusing on the fracture of FG structures. This gradation law was introduced by Delale and Erdogan (1983) and Zhang et al. (2003), offering an alternative mathematical description of property variation in FGM structures. The volume fraction functions are as defined in Eqs. (3) and (4). The exponential law for material properties distribution in FGSBs can be expressed in general form as follows (Garg et al., 2021a):

(i) For Types A and C,

$$E(z) = E_m e^{\left(\ln\left(\frac{E_c}{E_m}\right)V_c(z)\right)}$$
$$\rho(z) = \rho_m e^{\ln\left(\frac{\rho_c}{\rho_m}\right)V_c(z)} \tag{5}$$

(ii) For Type B,

$$E(z) = E_c e^{\ln\left(\frac{E_m}{E_c}\right)V_c(z)}$$
$$\rho(z) = \rho_c e^{\ln\left(\frac{\rho_m}{\rho_c}\right)V_c(z)} \quad (6)$$

Based on the above expressions, Figure 3 shows Young's modulus variation for the Type A beam as an example.

(c) Sigmoid distribution law. The utilization of the sigmoid law presents a more sophisticated technique for characterizing the distribution of material properties, particularly in bilayered FG beams. The application of a basic power law could lead to abrupt changes in stress at the interface between layers. To maintain stress continuity at these interfaces, Chi and Chung (2006) proposed the sigmoid law, combining two power-law functions to model the gradual material properties variation. The first law defines the variation from $z = h/2$ to $z = 0$, and the second one governs the variation from $z = 0$ to $z = h/2$. This dual-function approach allows for a smooth transition of properties across the beam's thickness, effectively eliminating stress discontinuities at layer interfaces. The volume fraction of FGSBs following the sigmoid law function through the thickness can be expressed as follows (Garg et al., 2020):

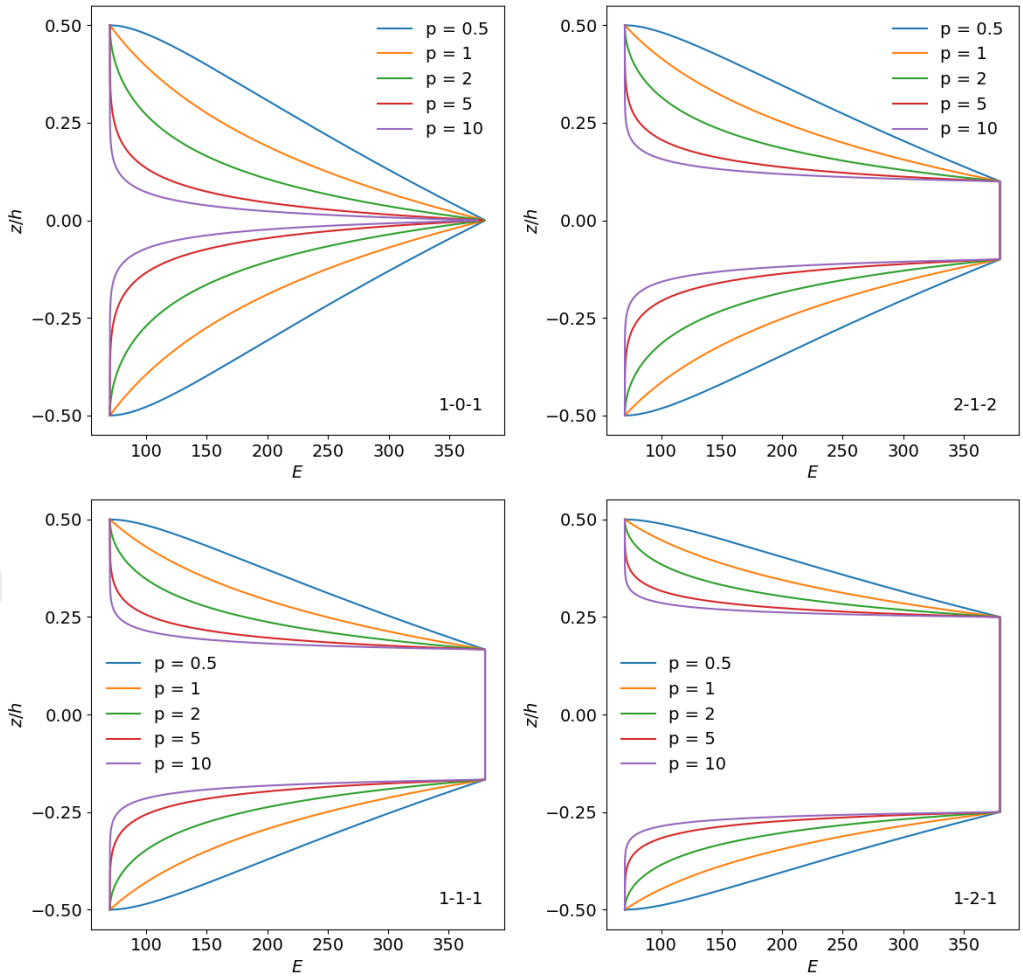

Figure 3. Variation in Young's modulus of Type A beams through the thickness by exponential law

(i) For Types A and B,

$$V_c(z) = 0.5\left(\frac{z-h_0}{h_{m1}-h_0}\right)^p \text{ for } z \in [h_0, h_{m1}]$$

$$V_c(z) = 1 - 0.5\left(\frac{z-h_1}{h_{m1}-h_1}\right)^p \text{ for } z \in [h_{m1}, h_1]$$

$$V_c(z) = 1 \text{ for } z \in [h_1, h_2] \tag{7}$$

$$V_c(z) = 1 - 0.5\left(\frac{z-h_2}{h_{m2}-h_2}\right)^p \text{ for } z \in [h_2, h_{m2}]$$

$$V_c(z) = 0.5\left(\frac{z-h_3}{h_{m2}-h_3}\right)^p \text{ for } z \in [h_{m2}, h_3]$$

where $h_{m1} = \frac{(h_0+h_1)}{2}$ and $h_{m2} = \frac{(h_2+h_3)}{2}$.

(ii) For Type C,

$$
\begin{aligned}
V_c(z) &= 0 \text{ for } z \in [h_0, h_1] \\
V_c(z) &= 0.5\left(\frac{z-h_1}{h_{m3}-h_1}\right)^p \text{ for } z \in [h_1, h_{m3}] \\
V_c(z) &= 1 - 0.5\left(\frac{z-h_2}{h_{m3}-h_2}\right)^p \text{ for } z \in [h_{m3}, h_2] \\
V_c(z) &= 1 \text{ for } z \in [h_2, h_3]
\end{aligned}
\tag{8}
$$

where $h_{m3} = \frac{(h_1+h_2)}{2}$. The effective material properties are defined in a similar manner to the power law. Figure 4 visually represents the volume fraction variation based on the sigmoid law for Type A beam.

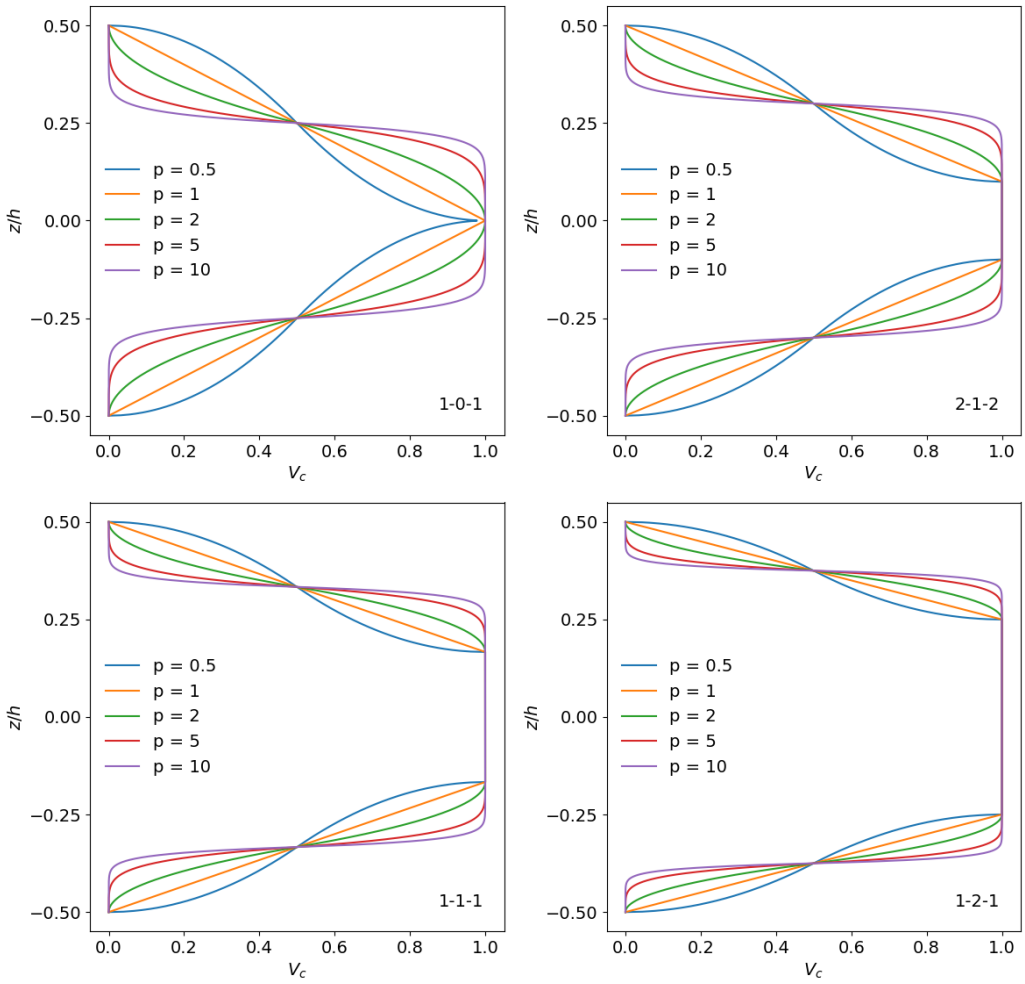

Figure 4. Volume fraction variation of Type A beams by the sigmoid law

1.3.2. Porosity Distribution

FG porous material (FGPM) is a novel material concept that effectively merges the principles of FGMs and porous materials, enabling continuous microstructure and porosity gradients along any specified direction (Babaei et al., 2022). This integration enhances the material's versatility and performance by incorporating both the gradual variation of material properties seen in conventional FGMs with porosity as another variable in the gradient of the material. In FGPMs, pores are distributed throughout the base material with varying porosity. This variation in porosity may arise due to alterations in pore arrangement and size (Kiarasi et al., 2021).

Figure 5 shows three main patterns of porosity distributions that are commonly discussed in the literature (Chen et al., 2018). In a uniform distribution (UD), porosity is evenly distributed throughout the porous body, resulting in consistent properties across the material. Symmetrical distribution (SD) is characterized by porosity that continuously decreases or increases from the mid-plane to the surfaces, creating a balanced gradient. In contrast, asymmetrical distribution (ASD) features porosity that gradually changes from the top surface to the bottom, offering a directional gradient of properties. These distribution patterns allow for tailored material properties to suit specific application requirements. In an FGSB with porous core, Young's modulus and mass density variation can be modeled in the following way (Chen et al., 2016).

(i) Uniform porosity distribution (UD):

$$\begin{aligned} E(z) &= E_{max}[1 - e_0\alpha] \\ \rho(z) &= \rho_{max}\sqrt{1 - e_0\alpha} \end{aligned} \tag{9}$$

(ii) Symmetric porosity distribution (SD):

$$\begin{aligned} E(z) &= E_{max}\left[1 - e_0 cos\left(\frac{\pi z}{h_2 - h_1}\right)\right] \\ \rho(z) &= \rho_{max}\left[1 - e_m cos\left(\frac{\pi z}{h_2 - h_1}\right)\right]] \end{aligned} \tag{10}$$

(iii) Asymmetric porosity distribution (ASD):

$$E(z) = E_{max}\left[1 - e_0 cos\left(\frac{\pi z}{2(h_2 - h_1)} + \frac{\pi}{4}\right)\right]$$
$$\rho(z) = \rho_{max}\left[1 - e_m cos\left(\frac{\pi z}{2(h_2 - h_1)} + \frac{\pi}{4}\right)\right] \quad (11)$$

where the symbols e_0 and e_m represent the porosity and mass density coefficients, respectively, while $E_{max}(z)$ and $\rho_{max}(z)$ denote the corresponding maximum values of the Young's modulus and material density. The coefficients α and e_m can be determined using the following approach.

$$\alpha = \frac{1}{e_0} - \frac{1}{e_0}\left(\frac{2}{\pi}\sqrt{1 - e_0} - \frac{2}{\pi} + 1\right)^2$$
$$e_m = 1 - \sqrt{1 - e_0} \quad (12)$$

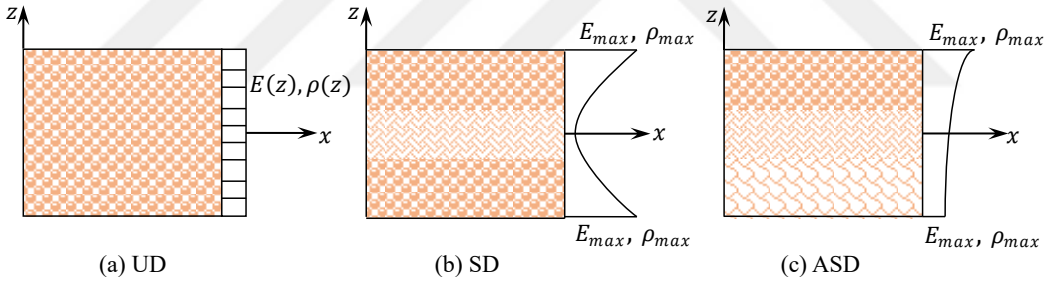

(a) UD (b) SD (c) ASD

Figure 5. Porosity distribution patterns

1.3.3. Theories for Modeling and Analysis

Extensive research has been conducted on FGSBs in recent years, with a focus on their behavioral characteristics, according to the recent reviews by Garg et al. (2021). Birman and Kardomateas (2018) provided a comprehensive overview of the various theories used to assess the structural responses of such types of beams, categorizing them primarily as CBT, FSDT, HSDT, and quasi-3D deformation theories.

(1) Classical Beam Theory (CBT). The CBT, also referred to as the Euler-Bernoulli beam theory, stands as the most basic approach for analyzing beams (Yang et al., 2013). This basic model operates on the principle that cross-sections originally perpendicular to

the beam's neutral axis maintain their planarity and remain normal to this axis even when the beam undergoes bending deformation. However, it is important to note that this theory does not account for the transverse shear deformation effects, limiting its applicability to slender beam analysis. The CBT displacement field can be mathematically represented as follows (Yang et al., 2013):

$$\begin{aligned} u(x,z,t) &= u_0(x,t) - z\frac{\partial w_o}{\partial x} \\ w(x,z,t) &= w_0(x,t) \end{aligned} \tag{13}$$

where u and w denote the displacements in the x- and z- directions, respectively. u_0 and w_0 are the displacements at the beam's midplane.

(2) First-order Shear Deformation Theory (FSDT). The FSDT addresses the limitations of CBT through the incorporation of shear deformation effects, assumed to be constant across the beam's thickness. It also assumes that cross-sections remain planar after bending but may not stay perpendicular to the neutral axis. FSDT provides more accurate results for thick and anisotropic beams compared to CBT. Nonetheless, accurate representation of transverse shear deformation in FSDT necessitates the use of a shear correction factor. The theory's displacement field can be mathematically expressed as (Van Vinh et al., 2022):

$$\begin{aligned} u(x,z,t) &= u_0(x,t) - z\phi(x,t) \\ w(x,z,t) &= w_0(x,t) \end{aligned} \tag{14}$$

where ϕ is the rotation of the cross-section.

(3) Higher-order Shear Deformation Theories (HSDTs). Driven by the need to eliminate the requirement for a shear correction factor in FSDT, HSDTs emerged as a significant advancement in the study of beam structures. HSDTs employ higher-order shape functions, which can be polynomial or non-polynomial, to more accurately model transverse shear deformation. This results in a more realistic representation of transverse shear stress variation across the beam's thickness. By incorporating higher-order terms, HSDTs offer enhanced accuracy in predicting beam behavior, especially for thicker beams

where shear deformation is significant. The displacement fields for various HSDTs can be generally expressed as (Sayyad et al., 2022):

$$u(x,z,t) = u_0(x,t) - z\frac{\partial w_o}{\partial x} + f(z)\phi(x,t)$$
$$w(x,z,t) = w_0(x,t) \tag{15}$$

where $f(z)$ is the shear shape function. Numerous HSDTs have been developed using polynomial or non-polynomial shape functions. A summary of some available shear-shape functions is provided in Table 1.

Table 1. Shear shape functions used in various HSDTs

References	$f(z)$
Reddy (1984); Murthy (1903); Levinson (1980)	$f(z) = z\left(1 - \frac{4z^2}{3h^2}\right)$
Panc (1975); Reissner (1975); Kruszewski and Kruszewski (1949)	$(z) = z\left(\frac{5}{4} - \frac{5z^2}{3h^2}\right)$
Ambartsumian (1960)	$f(z) = \frac{h^2}{8}z - \frac{z^3}{6}$
Nguyen-Xuan et al. (2013)	$f(z) = \frac{7}{8}z - \frac{2z^3}{h^2} + \frac{2z^5}{h^4}$
Nguyen et al. (2014)	$f(z) = h\tan\left(\frac{h}{z}\right) - \frac{16z^3}{15h^3}$
Arya et al. (2002); Ferreira et al. (2005)	$f(z) = \sin\left(\frac{\pi z}{h}\right)$
Stein (1986)	$f(z) = \frac{h}{\pi}\sin\left(\frac{\pi z}{h}\right)$
Akavci & Tanrikulu (2008)	$f(z) = \frac{3\pi}{2}h\tanh\left(\frac{z}{h}\right) - \frac{3\pi}{2}z\,\mathrm{sech}^2\left(\frac{1}{2}\right)$
Soldatos (1992)	$f(z) = h\sinh\left(\frac{z}{h}\right) - z\cosh\left(\frac{1}{2}\right)$
Grover et al. (2013)	$f(z) = \sinh^{-1}\left(\frac{rz}{h}\right) - \frac{z}{h}\left(\frac{2r}{\sqrt{r^2+4}}\right)$
Mahi et al. (2015)	$f(z) = \frac{h}{2}\tanh\left(\frac{2z}{h}\right) - \frac{4}{3}\left(\frac{z}{h}\right)^3\frac{1}{\cosh^2(1)}$
Karama et al. (2009)	$f(z) = ze^{-2(z/h)^2}$

(4) Quasi-3D Deformation Theories (HSNDTs). Quasi-3D theories represent an extension of HSDTs, incorporating the effect of transverse normal stress for a more comprehensive investigation. By incorporating thickness-stretching effects into the transverse displacement through higher-order shape functions, quasi-3D theories account for both transverse shear and normal deformations, resulting in more accurate predictions. In general, the unified displacement field for quasi-3D beam deformation theory is represented as follows (Fang et al., 2019):

$$\begin{aligned} u(x,z,t) &= u_0(x,t) - z\frac{dw_o}{dx} + f(z)\phi_y(x,t) \\ w(x,z,t) &= w_0(x,t) + f'(z)\phi_z(x,t) \end{aligned} \tag{16}$$

where the shear slopes associated with the transverse shear and normal deformations are represented by ϕ_y and ϕ_z, respectively

1.3.4. Analytical and Numerical Solutions Methods

Over time, various analytical and numerical approaches have been developed to study FGSBs. Despite their high accuracy, analytical approaches are typically restricted to problems with simplified geometries, boundary conditions, and loading scenarios. As a result, there has been a noticeable increase in the application of numerical techniques to more complex problems. This section focuses on the implementation and effectiveness of some of the most popular and commonly used methods in the analysis of FGSBs.

(1) Navier's method. Among the analytical approaches, Navier's method stands out as the simplest and most well-established analytical solution technique. Its straightforward implementation and reliable results have led to extensive use in the literature (Abed and Bousahla, 2022; Osofero et al., 2016; Sayyad et al., 2017; Sayyad and Avhad, 2019; Sayyad and Ghugal, 2019a; Turan and Kahya, 2021). However, this approach is primarily effective with simple supported boundary conditions. This method approximates unknown displacement variables using trigonometric functions that satisfy the boundary conditions. For simply supported beams, these functions typically take the form of sine or cosine series, which inherently meet the zero displacement and moment conditions at the

supports. For instance, the displacement variables in the quasi-3D theory can be expressed as (Sayyad et al., 2017)

$$\begin{aligned} u_0(x,t) &= \sum_{m=1}^{\infty} U_m \cos(\alpha x) e^{i\omega t} \\ w_0(x,t) &= \sum_{m=1}^{\infty} W_m \sin(\alpha x)\, e^{i\omega t} \\ \phi_y(x,t) &= \sum_{m=1}^{\infty} \phi_{ym} \cos(\alpha x)\, e^{i\omega t} \\ \phi_z(x,t) &= \sum_{m=1}^{\infty} \phi_{zm} \sin(\alpha x) e^{i\omega t} \end{aligned} \tag{17}$$

where U_m, W_m, ϕ_{ym} and ϕ_{zm} are unknown coefficients, ω refers to the beam's natural frequency, $\alpha = m\pi/L$ is nondimensional parameter, m presents a positive integer, which is taken as $m = 1$, and $\sqrt{i} = -1$ represents the imaginary unit.

(2) Ritz method. The Ritz method, based on energy principles, has emerged as a more effective alternative to the Navier method in the analysis of FGSBs with complex boundary conditions. The Ritz method offers greater flexibility in handling various boundary conditions, making it a valuable tool for studying more complex beam configurations. It has been increasingly employed in recent studies (Arefi and Najafitabar, 2021; Karamanli and Aydogdu, 2020; Karamanlı, 2018; Nguyen et al., 2016; Rezaiee-Pajand et al., 2018; Vo, Osofero, et al., 2014) to analyze the static, dynamic, and buckling behavior of various FGSBs configurations using a variety of displacement-based theories. The Ritz method uses admissible functions that can be approximated to satisfy essential boundary conditions. These admissible shape functions can be in polynomial, trigonometric, exponential, or hybrid form. However, improper shape functions may reduce the rate of convergence and lead to numerical instabilities. For instance, the unknown displacements of a quasi-3D theory can be presented as follows (Karamanlı, 2018b):

$$u_0(x,t) = \sum_{j=1}^{m} a_j \psi_{j,x}(x) e^{i\omega t}$$
$$w_0(x,t) = \sum_{j=1}^{m} b_j \psi_j(x) e^{i\omega t}$$
$$\phi_y(x,t) = \sum_{j=1}^{m} c_j \psi_{j,x}(x) e^{i\omega t} \quad (18)$$
$$\phi_z(x,t) = \sum_{j=1}^{m} d_j \psi_j(x) e^{i\omega t}$$

where $\psi_j(x)$ represents the admissible shape function that satisfies the kinematic boundary conditions, and (a_j, b_j, c_j and d_j) indicate the unknown coefficients to be determined. It is essential to note that the number of terms included in the series approximation as well as the choice of admissible functions has significant effects on the accuracy of the Ritz method.

(3) Finite Elements Method (FEM). FEM has emerged as the preferred numerical approach for analyzing FGSBs due to its versatility in handling complex engineering challenges. The implementation of FEM for FGSBs typically involves several key steps: (i) discretizing the beam into finite elements (ii) formulating elements using polynomial shape functions to approximate the displacement field, (iii) incorporating FG material properties, and (iv) assembling element matrices into global ones. The method's flexibility in handling various boundary conditions and its capability to account for non-linear behavior make it a powerful tool for analyzing the complex nature of FGSBs. Numerous studies have demonstrated the efficacy of FEM in analyzing FGSBs across various aspects. In mechanical analysis, researchers like Van Vinh (2021), Belarbi et al. (2021, 2022), Kahya and Turan (2018), Vo et al. (2014, 2015), Li et al. (2019), and Koutoati et al. (2021) have proposed novel FE models for buckling, free vibration, and static bending analysis using different deformation theories.

Displacements on individual elements are approximated through the utilization of shape functions and the corresponding nodal values. Generalized displacements throughout the element based on a quasi-3D theory are stated as (Vo et al., 2015):

$$
\begin{aligned}
u_0(x,t) &= \sum_{i=1}^{n} \psi_i(x)\, u_i \\
w_0(x,t) &= \sum_{i=1}^{n} \varphi_i(x)\, w_i \\
\phi_y(x,t) &= \sum_{i=1}^{n} \psi_i(x)\, \phi_{yi} \\
\phi_z(x,t) &= \sum_{i=1}^{n} \psi_i(x)\, \phi_{zi}
\end{aligned}
\tag{19}
$$

where the generalized nodal displacement variables are represented by u_i, w_i, ϕ_{yi}, and ϕ_{zi} where i indicates the node. The corresponding shape functions for each node are $\psi_i(x)$ and $\varphi_i(x)$. A linear polynomial interpolation function $\psi_i(x)$ satisfying continuous conditions which satisfy C^0-continuity is used to approximate the unknown displacements u_0, ϕ_y and ϕ_z. Meanwhile a Hermite-cubic polynomial interpolation function $\varphi_i(x)$, which satisfy C^1-continuity condition is used to approximate w_0.

1.3.5. Elastic Foundation Models

Elastic foundation models are crucial in structural engineering for analyzing the interaction between structures and their supports. Winkler, Pasternak, and Kerr models are among the most commonly used to describe this interaction in beams.

The Winkler elastic foundation introduced in 1867, is a simplified model that assumes a series of independent vertical springs (Winkler, 1967). Each spring supports a small segment of the beam and behaves independently of the others. The model assumes a linear elastic foundation behavior, where the beam deflection is directly proportional to the applied load. This relationship can be mathematically expressed as (Winkler, 1967):

$$F_w = k_{\mathrm{w}} w \tag{20}$$

where F_w is the foundation reaction, k_{w} is the Winkler constant, and w is the deflection of the beam. The simplicity of the Winkler model makes it easy to use, but it has limitations,

particularly in its neglect of shear interactions between soil elements. To address these shortcomings, more advanced models have been developed.

The Pasternak model extends the Winkler model by introducing additional springs that represent the shear interaction between adjacent supports (Pasternak, 1954). This is achieved by adding shear layers that connect the vertical springs, allowing the foundation to exhibit non-linear behavior and account for coupling effects between vertical and horizontal deformations. The force induced by the Pasternak foundation is given by (Pasternak, 1954):

$$F_p = k_{\mathrm{w}} w - k_p \left(\frac{dw}{\partial x}\right)^2 \tag{21}$$

where k_p is the Pasternak constant. This model is more accurate than the Winkler model as it considers the shear interactions, making it suitable for problems where the foundation exhibits significant shear behavior.

Kerr Foundation is a three-parameter elastic model introduced in 1964 as a further extension that aims to capture more complex interactions within the foundation (Kneifati, 1985). This model combines elements of both the Winkler and Pasternak models and introduces two spring layers with different stiffnesses, connected by a shear layer. The distributed reaction of the Kerr foundation model is defined as follows (Kneifati, 1985):

$$F_k = \left(\frac{k_l k_u}{k_l + k_u}\right) w - \left(\frac{k_s k_u}{k_l + k_u}\right) \left(\frac{\partial w}{\partial x}\right)^2 \tag{22}$$

where k_u is the stiffness of the upper layer, k_s the stiffness of the spring layer, and k_l is the stiffness of the lower layer. The Kerr model offers a more accurate representation of complex interactions within the foundation and can model both local and global deformations. Figure 6 illustrates a schematic representation of the Winkler, Pasternak, and Kerr models.

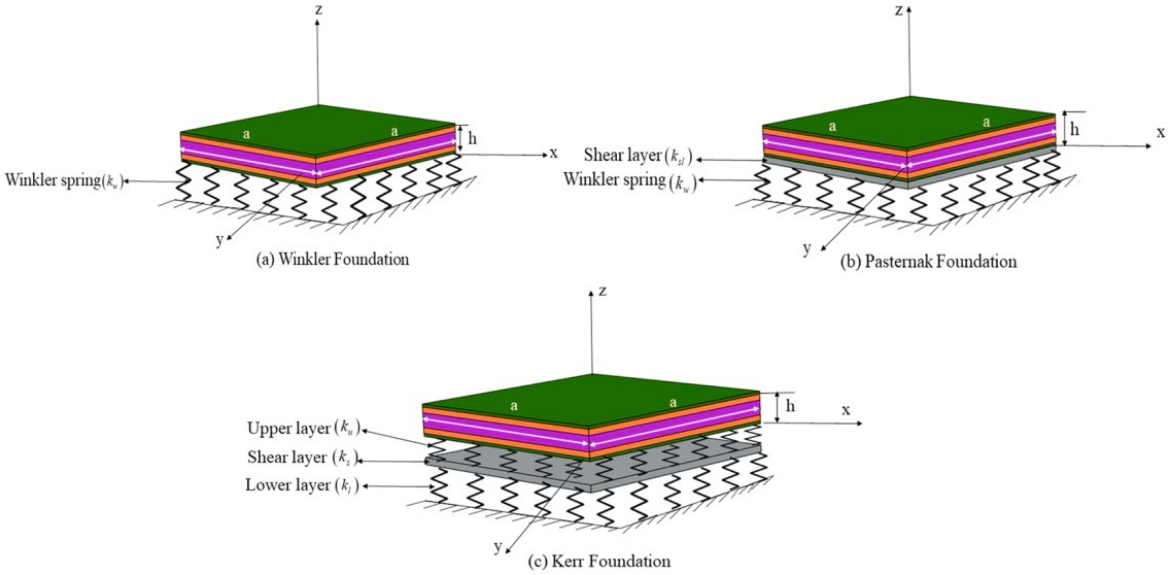

Figure 6. Schematic of elastic foundation models: (a) Winkler, (b) Pasternak, and (c) Kerr (Kumar & Harsha, 2022)

1.4. Thesis Objectives

This research aims to comprehensively investigate the mechanical characteristics of FGSBs with porous core resting on Winkler-Pasternak elastic foundations. The study focuses on static, dynamic, and stability characteristics of three different beam configurations featuring porous ceramic core, metallic core, and FG porous core, aiming to provide an accurate understanding of the governing parameters. This research presents quasi-3D-based theoretical frameworks that account for transverse shear and normal deformations. Analytical models are formulated using the Navier and Ritz method. Furthermore, a novel three-node higher-order FE model with five degrees of freedom per node is introduced. To complement the theoretical models, a novel modeling technique is developed using Ansys Mechanical APDL for FGSBs with porous core. To demonstrate the accuracy and effectiveness of the proposed models, numerical examples are presented that explore the influence of key parameters on the free vibration, buckling, and static response of FGSBs wth porous core. These include transverse normal deformation, boundary conditions, geometric properties, material properties, porosity characteristics, and foundation parameters.

1.5. Novelty and Contributions

The research aims to understand the combined effects of core porosity and elastic foundation on the behavior of FGSBs by examining static, dynamic, and stability aspects. This investigation utilizes quasi-3D theory to provide a more thorough understanding of FGSBs behavior, addressing a significant gap in research where the application of quasi-3D theories has been limited, particularly in FEM due to the C^1-continuity challenges. To address this limitation, this research formulates a new quasi-3D higher-order FE model to accurately predict FGSB responses. Furthermore, the current research presents an innovative computational methodology for accurately representing the gradual changes in material composition within FGSBs, adhering to the exact mathematical equations governing material distribution laws using Ansys Mechanical APDL.

This research is expected to yield valuable insights into the mechanical behavior of FGSBs with porous cores, ultimately informing the design and optimization of these beams for enhanced efficiency and cost-effectiveness in construction and various engineering applications. The presented benchmark results can also be referenced for further research in this field.

1.6. Thesis Structure

The dissertation comprises four chapters that meticulously outline the progression and examination procedures. The arrangement is outlined below:

Chapter 1 begins with a general introduction that provides an overview of advanced composites and their associated computational theories and methods. Then, it provides a literature review of existing research on the mechanical analysis of FGP beams and FGP sandwich beams. To guide the research direction, the chapter highlights the main research gaps identified in the literature. The theoretical framework is then discussed, covering commonly used gradation laws, porosity distributions, kinematic theories, and solution methods in predicting their behavior, along with elastic foundation models. The main objectives and contributions of the current research are then outlined.

Chapter 2 presents the theoretical framework and quasi-3D theory formulation, including mathematical modeling and governing equations. The chapter also proposes analytical models based on the Navier and Ritz methods. Furthermore, a novel three-node

FE model with five degrees of freedom per node is introduced, along with a new modeling technique using Ansys Mechanical APDL.

Chapter 3 presents numerical results from both analytical and numerical solutions, validating the proposed models while investigating the influence of various parameters on the mechanical responses of the beams.

Chapter 4 concludes the thesis by presenting the important findings of the research and outlining potential directions for future investigations.

2. RESEARCH METHODOLOGY

2.1. Introduction

This chapter develops quasi-3D theory-based models for FGSBs with porous core resting on a Winkler-Pasternak elastic foundation. The comprehensive theoretical formulation, including mathematical modeling and governing equations, is detailed herein. A power-law distribution governs the gradual variation of FG material properties through the beam thickness. Three distinct porosity patterns are considered such as uniform, symmetric, and asymmetric. Herein, analytical solutions using Navier and Ritz methods, along with a novel three-node higher-order FE model are also developed. Furthermore, a novel modeling technique using Ansys Mechanical APDL for FGSBs with porous core is presented.

2.2. Governing Equations

Consider an FGSB consisting of three layers with a rectangular cross-section (thickness h, width b, and length L) as shown in Figure 7. The beam is supported by a Winkler-Pasternak elastic foundation. The top and bottom faces are located at $z = \pm h/2$. Three types of FGSBs are investigated: (i) Type A with FG face layers and a porous ceramic core, (ii) Type B with FG face layers and a porous metal core, and (iii) Type C with homogeneous face layers and an FG porous core. The beam's volume fractions and material properties follow a power law distribution, as detailed in Section 1.3.1, resulting in a gradual and continuous variation through its thickness. Three distinct porosity configurations, as illustrated in Section 1.3.2, are considered in this study.

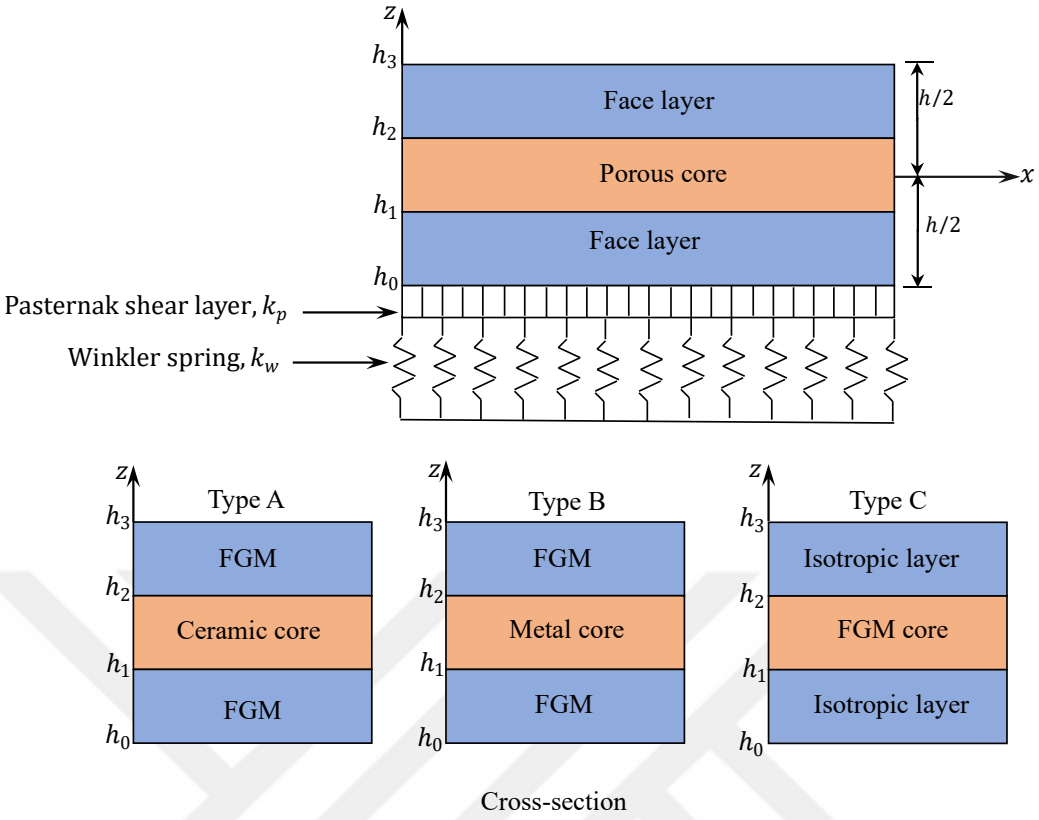

Figure 7. Schematic of FGSBs with porous core on elastic foundation

The quasi-3D deformation theory's displacement field is presented as follows:

$$u(x,z,t) = u_0(x) - z\frac{dw_o}{dx} + f(z)\phi_y(x)$$
$$w(x,z,t) = w_0(x) + g(z)\phi_z(x) \tag{23}$$

where u and w represent the displacements in x- and z-directions. The displacements at the beam's mid-plane are denoted by u_0 and w_0. The shear slopes associated with the transverse shear and normal deformations are represented by ϕ_y and ϕ_z, respectively. $g(z) = f'(z)$.The function $f(z)$ denotes the shear shape function and is defined as:

$$f(z) = z - \frac{4z^3}{3h^2} \tag{24}$$

The strain field is formulated based on the strain-displacement relationship, as detailed below.

$$\begin{aligned}\varepsilon_x &= \varepsilon_x^0 - zk_x + f\varepsilon_x^1 \\ \varepsilon_z &= g'(z)\phi_z(x) \\ \gamma_{xz} &= g(z)\gamma_{xz}^0\end{aligned} \tag{25}$$

where

$$\varepsilon_x^0 = \frac{\partial u_0}{\partial x}, \qquad k_x = \frac{\partial^2 w_0}{\partial x^2}, \qquad \varepsilon_x^1 = \frac{\partial \phi_y}{\partial x}, \qquad \gamma_{xz}^0 = \phi_y + \frac{\partial \phi_z}{\partial x} \tag{26}$$

The following represents the stress-strain relationship of the FG sandwich beam:

$$\begin{Bmatrix}\sigma_x \\ \sigma_z \\ \tau_{xz}\end{Bmatrix} = \begin{bmatrix}Q_{11}(z) & Q_{13}(z) & 0 \\ Q_{13}(z) & Q_{33}(z) & 0 \\ 0 & 0 & Q_{55}(z)\end{bmatrix}\begin{Bmatrix}\varepsilon_x \\ \varepsilon_z \\ \gamma_{xz}\end{Bmatrix} \tag{27}$$

where

$$\begin{aligned}Q_{11}(z) = Q_{33}(z) &= \frac{E(z)}{1-\upsilon^2} \\ Q_{13}(z) &= \frac{\upsilon E(z)}{1-\upsilon^2} \\ Q_{55}(z) &= \frac{E(z)}{2(1+\upsilon)}\end{aligned} \tag{28}$$

where E is Young's modulus and υ is Poisson's ratio.

The strain energy variation of the beam is defined as follows:

$$\begin{aligned}\delta U &= \int_0^L \int_{-h/2}^{h/2} (\sigma_x \delta\varepsilon_x + \sigma_z \delta\varepsilon_z + \tau_{xz}\delta\gamma_{xz}) dz\, dx \\ &= \int_0^L \Bigg(N_x \frac{\partial \delta u_0}{\partial x} - M_x^b \frac{\partial^2 \delta w_0}{\partial x^2} + M_x^s \frac{\partial \delta \psi_x}{\partial x} + Q_z^s \delta\psi_z + Q_{xz}\delta\phi_y \\ &\qquad + Q_{xz}\frac{\partial \delta \phi_z}{\partial x}\Bigg) dx\end{aligned} \tag{29}$$

where the symbol δ indicates the variational operator. N_x, M_x^b, M_x^s, Q_{xz} and Q_z^s are force and moment resultants defined by:

$$
\begin{aligned}
[N_x, M_x^b, M_x^s] &= \int_{-h/2}^{h/2} \sigma_x [1, z, f(z)] dz \\
Q_{xz} &= \int_{-h/2}^{h/2} \tau_{xz} g(z) dz \\
Q_z^s &= \int_{-h/2}^{h/2} \sigma_z g'(z) dz
\end{aligned}
\tag{30}
$$

Substituting Eqs. (23), (24), (26), and (27) into Eq. (29) yields,

$$
\begin{aligned}
N_x &= A_{11} \frac{\partial u_0}{\partial x} - B_{11} \frac{\partial^2 w_0}{\partial x^2} + C_{11} \frac{\partial \phi_y}{\partial x} + D_{13} \phi_z \\
M_x^b &= B_{11} \frac{\partial u_0}{\partial x} - A_{S11} \frac{\partial^2 w_0}{\partial x^2} + B_{S11} \frac{\partial \phi_y}{\partial x} + C_{S13} \phi_z \\
M_x^s &= C_{11} \frac{\partial u_0}{\partial x} - B_{S11} \frac{\partial^2 w_0}{\partial x^2} + D_{S11} \frac{\partial \phi_z}{\partial x} + E_{13} \phi_z \\
Q_z^s &= D_{13} \frac{\partial u_0}{\partial x} - C_{S13} \frac{\partial^2 w_0}{\partial x^2} + E_{13} \frac{\partial \phi_y}{\partial x} + F_{33} \phi_z \\
Q_{xz} &= E_{55} \left(\phi_y + \frac{\partial \phi_z}{\partial x} \right)
\end{aligned}
\tag{31}
$$

where

$$
\begin{aligned}
&[A_{11}, B_{11}, C_{11}, A_{S11}, B_{S11}, D_{S11}, F_{33}] \\
&\quad = \int_{-h/2}^{h/2} Q_{11}(z) [1, z, f(z), z^2, zf(z), f^2(z), [g'(z)]^2] dz \\
&\left[D_{13}, E_{13}, C_{S13} \right] = \int_{-h/2}^{h/2} Q_{13}(z) g'(z) [1, f(z), z] dz \\
&E_{S55} = \int_{-h/2}^{h/2} Q_{55}(z) [g(z)]^2 dz
\end{aligned}
\tag{32}
$$

The kinetic energy variation can be stated as,

$$\begin{aligned}\delta K &= \int_0^L \int_{-h/2}^{h/2} \rho(z)\left(\frac{\partial u}{\partial t}\frac{\partial \delta u}{\partial t} + \frac{\partial w}{\partial t}\frac{\partial \delta w}{\partial t}\right) dz dx \\ &= \int_0^L \left(I_1 \frac{\partial^2 u_0}{\partial t^2} - I_2 \frac{\partial w_0}{\partial x \partial t^2} + I_4 \frac{\partial^2 \phi_y}{\partial t^2}\right) \delta u_0 dx \\ &+ \int_0^L \left(-I_2 \frac{\partial^2 u_0}{\partial t^2} - I_3 \frac{\partial^3 w_0}{\partial x \partial t^2} - I_5 \frac{\partial^2 \phi_y}{\partial t^2}\right) \frac{\partial \delta w_o}{\partial x} dx \\ &+ \int_0^L \left(I_4 \frac{\partial^2 u_0}{\partial t^2} - I_5 \frac{\partial^3 w_0}{\partial x \partial t^2} + I_6 \frac{\partial^2 \phi_y}{\partial t^2}\right) \delta \phi_z dx \\ &+ \int_0^L \left(I_1 \frac{\partial^2 w_0}{\partial t^2} + I_7 \frac{\partial^2 \phi_z}{\partial t^2}\right) \delta w_0 dx \\ &+ \int_0^L \left(I_7 \frac{\partial^2 w_0}{\partial t^2} + I_8 \frac{\partial^2 \phi_z}{\partial t^2}\right) \delta \phi_z dx\end{aligned} \tag{33}$$

where

$$[I_1, I_2, I_3, I_4, I_5, I_6, I_7, I_8] = \int_{-h/2}^{h/2} \rho(z)[1, z, z^2, f(z), zf(z), f^2(z), g(z), g^2(z)] dz \tag{34}$$

The potential energy variation due to an external axial force is given by,

$$\delta V = \int_0^L N_0 \frac{\partial^2 w_0}{\partial x^2} \delta w_0 dx - \int_0^L q \delta w_0 dx \tag{35}$$

where N_0 and q represent the axial force and transverse load.

The strain energy variation resulting from the elastic foundation can be written as

$$\delta U_F = -\int_0^L \left(k_{\mathrm{w}} w - k_p \frac{\partial^2 w}{\partial x^2} \right) \delta w dx \tag{36}$$

where k_{w} and k_p are the Winkler and Pasternak constants.

The governing differential equations of the proposed theory are obtained by applying Hamilton's principle, which states:

$$\int_0^T (\delta U + \delta U_F + \delta V - \delta K) dt = 0 \tag{37}$$

Substituting Eqs. (29), (33), (35), and (36) into Eq. (37), performing integration by parts, collecting the resulting expressions into the same brackets of the coefficients of the unknown displacement variables δu_0, δw_0, $\delta \phi_y$, and $\delta \phi_z$, respectively, and setting each bracket equal to zero, the following equations of motion can thus be obtained.

$$\begin{aligned}
\delta u_0: \quad & \frac{\partial N_x}{\partial x} = I_1 \frac{\partial^2 u_0}{\partial t^2} - I_2 \frac{\partial^3 w_0}{\partial t^2 \partial x} + I_4 \frac{\partial^2 \phi_y}{\partial t^2} \\
\delta w_0: \quad & \frac{\partial^2 M_x^b}{\partial x^2} + N_0 \frac{d^2 w_0}{dx^2} - q - k_w (w_0 + g\phi_z) + k_p \frac{d^2 (w_0 + g\phi_z)}{dx^2} + \\
& \qquad = I_2 \frac{\partial^3 u_0}{\partial t^2 \partial x} - I_3 \frac{\partial^4 w_0}{\partial t^2 \partial x^2} + I_5 \frac{\partial^3 \phi_y}{\partial t^2 \partial x} + I_1 \frac{\partial^2 w_0}{\partial t^2} + I_7 \frac{\partial^2 \phi_z}{\partial t^2} \\
\delta \phi_y: \quad & \frac{\partial M_x^s}{\partial x} - Q_{xz} = I_4 \frac{\partial^2 u_0}{\partial t^2} - I_5 \frac{\partial^3 w_0}{\partial t^2 \partial x} + I_6 \frac{\partial^2 \phi_y}{\partial t^2} \\
\delta \phi_z: \quad & \frac{\partial Q_{xz}}{\partial x} + g \left(-k_w (w_0 + g\phi_z) + k_p \frac{d^2 (w_0 + g\phi_z)}{dx^2} \right) - Q_z^s \\
& \qquad = I_7 \frac{\partial^2 w_0}{\partial t^2} + I_8 \frac{\partial^2 \phi_z}{\partial t^2}
\end{aligned} \tag{38}$$

2.3. Navier's Solution

Navier's method provides the analytical solution for simply supported FG beams by assuming the displacement variables in the form of a Fourier series as illustrated in Eq. (17). Additionally, the transverse load $q(x)$ is expressed as a Fourier series for a uniformly distributed load q_0 in the form of

$$q(x) = \sum_{m=1,3,5}^{\infty} \frac{4q_0}{m\pi} \sin \alpha x \tag{39}$$

Substituting Eq. (17) into Eq. (38), the following solution matrix for free vibration, buckling, and static bending analysis is obtained:

$$[\mathbf{K} - \omega^2 \mathbf{M} - N_0 \mathbf{G}]\mathbf{\Delta} = \{\mathbf{F}\} \tag{40}$$

where $\mathbf{K}$ represents the stiffness matrix, $\mathbf{M}$ the mass matrix, $\mathbf{G}$ the geometric stiffness matrix, $\mathbf{F}$ the vector of uniformly distributed load, and $\mathbf{\Delta}$ the vector of unknown coefficients. Explicit forms of these matrices are given by

$$\mathbf{K} = \begin{bmatrix} K_{11} & K_{12} & K_{13} & K_{14} \\ K_{12} & K_{22} & K_{23} & K_{24} \\ K_{13} & K_{23} & K_{33} & K_{34} \\ K_{14} & K_{24} & K_{34} & K_{44} \end{bmatrix}$$

$$\mathbf{M} = \begin{bmatrix} I_1 & -I_2\alpha & I_4 & 0 \\ -I_2\alpha & I_3\alpha^2 + I_1 & -I_5\alpha & I_7 \\ I_4 & -I_5\alpha & I_6 & 0 \\ 0 & I_7 & 0 & I_8 \end{bmatrix} \tag{41}$$

$$\boldsymbol{G} = \begin{bmatrix} 0 & 0 & 0 & 0 \\ 0 & \alpha^2 & 0 & 0 \\ 0 & 0 & 0 & 0 \\ 0 & 0 & 0 & 0 \end{bmatrix}$$

$$\boldsymbol{\Delta} = \begin{Bmatrix} U_m \\ W_m \\ \psi_{xm} \\ \psi_{zm} \end{Bmatrix}, \qquad \mathbf{F} = \begin{Bmatrix} 0 \\ \dfrac{4q_0}{m\pi} \\ 0 \\ 0 \end{Bmatrix}$$

where

$$\begin{aligned} K_{11} &= A_{11}\alpha^2, & K_{12} &= -B_{11}\alpha^3, \\ K_{13} &= C_{11}\alpha^2, & K_{14} &= -D_{13}\alpha, \\ K_{22} &= A_{S11}\alpha^4 + A_{S11}\alpha^4 + k_w + k_p\alpha^2, & & \\ K_{23} &= -B_{S11}\alpha^3, & K_{24} &= C_{S13}\alpha^2 + g(k_w + k_p\alpha^2), \\ K_{33} &= (D_{S11}\alpha^2 + E_{S55}), & K_{34} &= (E_{S55} - E_{13})\alpha, \\ K_{44} &= (E_{S55}\alpha^2 + F_{33}) + g^2(k_w + k_p\alpha^2) & & \end{aligned} \tag{42}$$

2.4. Ritz Solution

The Ritz method is formulated by applying the principle of total potential energy Π which is defined as

$$\Pi = U + U_F + V - K \tag{43}$$

where U denotes the strain energy, U_F is the strain energy due to elastic foundation, V represents the potential energy, and K is the kinetic energy.

The strain energy can be defined by

$$U = \frac{1}{2}\int_0^L \int_{-h/2}^{h/2} (\sigma_x \varepsilon_x + \sigma_z \varepsilon_z + \tau_{xz}\gamma_{xz}) dz dx \tag{44}$$

The kinetic energy is given by

$$K = \frac{1}{2}\int_0^L \int_{-h/2}^{h/2} \rho(z)\left(\dot{U}^2 + \dot{W}^2\right) dz dx \tag{45}$$

The potential energy resulting from an external axial force can be stated as

$$V = -\frac{1}{2}\int_0^L N_0 \left(\frac{\partial w_0}{\partial x}\right)^2 dx - \frac{1}{2}\int_0^L q w_0 dx \tag{46}$$

The elastic foundation's strain energy is given by

$$U_F = \frac{1}{2}\int_0^L \left(k_w w^2 + k_p \left(\frac{\partial w}{\partial x}\right)^2\right) dx \tag{47}$$

Polynomial series fulfilling the kinematic boundary conditions are used to define the displacement functions as given in Eq. (18). Polynomial and exponential shape functions satisfying different BCs, including simple supported (SS), clamped-clamped (CC), and clamped-free (CF) are employed to obtain analytical solutions, as detailed in Table 2.

Table 2. Ritz method shape functions for various BCs

BCs	$\psi_j(x)$	$x = 0$	$x = L$
SS	$\frac{x}{L}\left(1 - \frac{x}{L}\right) e^{-jx/L}$	$w_0 = 0, \phi_z = 0$	$w_0 = 0, \phi_z = 0$
CC	$\left(\frac{x}{L}\right)^2 \left(1 - \frac{x}{L}\right)^2 e^{-jx/L}$	$u_0 = 0, w_0 = 0, w_{,x} = 0$ $\phi_y = 0, \phi_z = 0$	$u_0 = 0, w_0 = 0, w_{,x} = 0$ $\phi_y = 0, \phi_z = 0$
CF	$\left(\frac{x}{L}\right)^2 e^{-jx/L}$	$u_0 = 0, w_0 = 0, w_{,x} = 0$ $\phi_y = 0, \phi_z = 0$	-

By substituting Eq. (18) into Eq. (43), the equations of motion can be derived using Lagrange's equation given by

$$\frac{d}{dt}\left(\frac{\partial \Pi}{\partial \dot{q}_j}\right) - \frac{\partial \Pi}{\partial q_j} = 0 \tag{48}$$

where the generalized coordinate vector is represented by q_j with an overdot indicating the time derivative. The resulting mass, stiffness, geometric stiffness matrices, and unknowns and force vectors are given by

$$\mathbf{K} = \begin{bmatrix} K_{11} & K_{12} & K_{13} & K_{14} \\ K_{12} & K_{22} & K_{23} & K_{24} \\ K_{13} & K_{23} & K_{33} & K_{34} \\ K_{14} & K_{24} & K_{34} & K_{44} \end{bmatrix}$$

$$\mathbf{M} = \begin{bmatrix} M_{11} & M_{12} & M_{13} & M_{14} \\ M_{12} & M_{22} & M_{23} & M_{24} \\ M_{13} & M_{23} & M_{33} & M_{34} \\ M_{14} & M_{24} & M_{34} & M_{44} \end{bmatrix}$$

$$\boldsymbol{G} = \begin{bmatrix} 0 & 0 & 0 & 0 \\ 0 & N_{22} & 0 & 0 \\ 0 & 0 & 0 & 0 \\ 0 & 0 & 0 & 0 \end{bmatrix} \tag{49}$$

$$\boldsymbol{\Delta} = \begin{Bmatrix} a \\ b \\ c \\ d \end{Bmatrix}, \quad \mathbf{F} = \begin{Bmatrix} 0 \\ F_i \\ 0 \\ 0 \end{Bmatrix}$$

where

$$K_{11}(i,j) = A_{11}\int_0^L \psi_{i,xx}\,\psi_{j,xx}dx, \qquad K_{12}(i,j) = -B_{11}\int_0^L \psi_{i,xx}\,\psi_{j,xx}dx,$$

$$K_{13}(i,j) = C_{11}\int_0^L \psi_{i,xx}\,\psi_{j,xx}dx\,, \quad K_{14}(i,j) = B_{S13}\int_0^L \psi_{i,xx}\,\psi_j dx$$

$$K_{22}(i,j) = E_{11}\int_0^L \psi_{i,xx}\psi_{j,xx}\,dx + k_w\int_0^L \psi_i\psi_j\,dx + k_p\int_0^L \psi_{i,x}\psi_{j,x}\,dx$$

$$K_{23}(i,j) = -D_{11}\int_0^L \psi_{i,xx}\,\psi_{j,xx}dx$$

$$K_{24}(i,j) = -C_{S13}\int_0^L \psi_{i,xx}\,\psi_j dx + gk_w\int_0^L \psi_i\,\psi_j dx + gk_p\int_0^L \psi_{i,x}\,\psi_{j,x}dx$$

$$K_{33}(i,j) = F_{11}\int_0^L \psi_{i,xx}\,\psi_{j,xx}dx + A_{s55}\int_0^L \psi_{i,x}\,\psi_{j,x}dx$$

$$K_{34}(i,j) = E_{S13}\int_0^L \psi_{i,xx}\,\psi_j dx + A_{s55}\int_0^L \psi_{i,x}\,\psi_{j,x}dx$$

$$K_{44}(i,j) = D_{S33}\int_0^L \psi_i\,\psi_j dx$$

$$+ A_{s55}\int_0^L \psi_{i,x}\,\psi_{j,x}dx + g^2k_w\int_0^L \psi_i\,\psi_j dx + g^2k_p\int_0^L \psi_{i,x}\,\psi_{j,x}dx \tag{50}$$

$$M_{11}(i,j) = I_1\int_0^L \psi_{i,x}\,\psi_{j,x}dx, \qquad M_{12}(i,j) = -I_2\int_0^L \psi_{i,x}\,\psi_{j,x}dx,$$

$$M_{13}(i,j) = I_4\int_0^L \psi_{i,x}\,\psi_{xj}dx \qquad M_{14}(i,j) = 0$$

$$M_{22}(i,j) = I_1\int_0^L \psi_i\psi_j\,dx + I_3\int_0^L \psi_{i,x}\psi_{j,x}\,dx$$

$$M_{23}(i,j) = -I_5\int_0^L \psi_{i,x}\,\psi_{j,x}dx \qquad M_{24}(i,j) = I_7\int_0^L \psi_i\,\psi_j dx$$

$$M_{33}(i,j) = I_6\int_0^L \psi_{i,x}\,\psi_{j,x}dx \qquad M_{34}(i,j) = 0 \qquad M_{44}(i,j) = I_8\int_0^L \psi_i\,\psi_j dx$$

$$N_{22}(i,j) = N_0\int_0^L \psi_{i,x}\psi_{j,x}$$

$$F_i(i) = \int_0^L q\psi_j dx$$

2.5. Novel Higher-Order Finite Element Model

A new higher-order FE model with three nodes, featuring a total of 15 degrees of freedom (DOFs) as illustrated in Figure 8, is developed to analyze the mechanical behavior of the beam. A linear polynomial interpolation function, $\psi_i(x)$, is used to estimate the displacement unknowns u_0, ϕ_y and ϕ_z, while a Hermite-cubic polynomial interpolation function $\varphi_i(x)$ is used to approximate w_0. The element's generalized displacements are as expressed in Eq. (19). The corresponding shape functions for each node are $\psi_i(x)$ and $\varphi_i(x)$, which are given as follows:

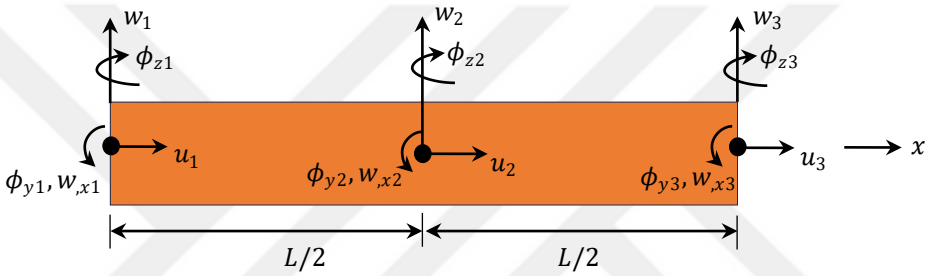

Figure 8. Three-node beam element

$$
\begin{aligned}
\psi_1 &= 1 - 3\xi + 2\xi^2 \\
\psi_2 &= 4\xi - 4\xi^2 \\
\psi_3 &= -\xi + 2\xi^2 \\
\varphi_1 &= 1 - 23\xi^2 + 66\xi^3 - 68\xi^4 + 24\xi^5 \\
\varphi_2 &= L\xi(1 - 6\xi + 13\xi^2 - 12\xi^3 + 4\xi^4) \\
\varphi_3 &= 16\xi^2 - 32\xi^3 + 16\xi^4 \\
\varphi_4 &= L\xi(-8\xi + 32\xi^2 - 40\xi^3 + 16\xi^4) \\
\varphi_5 &= 7\xi^2 - 34\xi^3 + 52\xi^4 - 24\xi^5 \\
\varphi_6 &= L\xi(-\xi + 5\xi^2 - 8\xi^3 + 4\xi^4)
\end{aligned}
\tag{51}
$$

where

$$
\xi = \frac{x}{L} \tag{52}
$$

The FE model leverages the same energy formulations expressed in Eqs. (43)–(48) for deriving the equations of motion, as described in the Ritz method (Section 2.4). The general solution matrix in Eq. (40) for mechanical analysis is obtained by substituting Eq. (19) into Eq. (43) and applying it in Eq. (48), following the same matrix formulation as in the Ritz method. The matrix components K, M, N, and F are defined as follows:

$$
\begin{aligned}
K_{11}(i,j) &= A_{11}\int_0^L \psi_{i,x}\,\psi_{j,x}dx \\
K_{12}(i,j) &= -B_{11}\int_0^L \psi_{i,x}\,\varphi_{j,xx}dx \\
K_{13}(i,j) &= C_{11}\int_0^L \psi_{i,x}\,\psi_{j,x}dx \\
K_{14}(i,j) &= B_{S13}\int_0^L \psi_{i,x}\,\psi_j dx \\
K_{22}(i,j) &= E_{11}\int_0^L \varphi_{i,xx}\varphi_{j,xx}\,dx + k_w\int_0^L \varphi_i\varphi_j\,dx + k_p\int_0^L \varphi_{i,x}\varphi_{j,x}\,dx \\
K_{23}(i,j) &= -D_{11}\int_0^L \varphi_{i,xx}\,\psi_{j,x}dx \\
K_{24}(i,j) &= -C_{S13}\int_0^L \varphi_{i,xx}\,\psi_j dx + gk_w\int_0^L \varphi_i\,\psi_j dx + gk_p\int_0^L \varphi_{i,x}\,\psi_{j,x}dx \\
K_{33}(i,j) &= F_{11}\int_0^L \psi_{i,x}\,\psi_{j,x}dx + A_{s55}\int_0^L \psi_i\,\psi_j dx \\
K_{34}(i,j) &= E_{S13}\int_0^L \psi_{i,x}\,\psi_j dx + A_{s55}\int_0^L \psi_i\,\psi_{j,x}dx \\
K_{44}(i,j) &= D_{S33}\int_0^L \psi_i\,\psi_j dx \\
&\quad + A_{s55}\int_0^L \psi_{i,x}\,\psi_{j,x}dx + g^2k_w\int_0^L \psi_i\,\psi_j dx + g^2k_p\int_0^L \psi_{i,x}\,\psi_{j,x}dx \\
M_{11}(i,j) &= I_1\int_0^L \psi_i\,\psi_j dx \\
M_{12}(i,j) &= -I_2\int_0^L \psi_i\,\varphi_{j,x}dx \\
M_{13}(i,j) &= I_4\int_0^L \psi_i\,\psi_j dx
\end{aligned}
\tag{53}
$$

$$
\begin{aligned}
M_{14}(i,j) &= M_{34}(i,j) = 0 \\
M_{22}(i,j) &= I_1 \int_0^L \varphi_i \varphi_j \, dx + I_3 \int_0^L \varphi_{i,x} \varphi_{j,x} \, dx \\
M_{23}(i,j) &= -I_5 \int_0^L \varphi_{i,x} \, \psi_j dx \\
M_{23}(i,j) &= -I_5 \int_0^L \varphi_{i,x} \, \psi_j dx \\
M_{24}(i,j) &= I_7 \int_0^L \varphi_i \, \psi_j dx \\
M_{33}(i,j) &= I_6 \int_0^L \psi_i \, \psi_j dx \\
M_{44}(i,j) &= I_8 \int_0^L \psi_i \, \psi_j dx \\
N_{22}(i,j) &= N_0 \int_0^L \varphi_{i,x} \varphi_{j,x} \, dx \\
F_i(i) &= \int_0^L q w_0 dx
\end{aligned}
\tag{53}
$$

2.6. Computational Modeling of Material Gradation Using Ansys APDL

In recent decades, the FEM has garnered considerable attention among the computational methods for the analysis of FGSBs. The approach involving layerwise gradation is identified as the leading computational modeling strategy for FG sandwich structures in Ansys or other FE software. (Al-Itbi and Noori, 2022; Demir et al., 2013; Grygorowicz et al., 2015; Njim et al., 2022; Soltani and Asgarian, 2019). However, this approach contradicts the fundamental concept of functional gradation, which implies a continuous variation of material properties. This study addresses this gap by introducing a novel computational approach in Ansys Mechanical APDL, enabling the effective modeling of gradually varying properties in FG sandwich structures like beams and plates through direct implementation of material distribution laws.

The modeling of FGSBs with porous core is conducted using Ansys Mechanical APDL by utilizing User-Defined Field (UDF) functionalities. The UDF variables can be customized to suit the initial state of the model, including the initial coordinates of the

nodes. FGSBs can be effectively modeled by relating their gradually varying properties with the coordinates within the UDF. This technique facilitates the continuous assignment of properties throughout the geometry's nodes based on the power law distribution. By implementing this approach, the gradual change in material properties across the thickness can be precisely represented using both 3D solid and 2D plane elements.

In this study, the SOLID186 element is employed to model the beams. SOLID186 is a higher-order, 3D element with 20 nodes and three DOF per node, demonstrating quadratic displacement behavior. The modeling methodology employs a collection of custom-developed APDL scripts, each designed to handle a specific stage of the process. In this framework, a script, referred to as a macro file, is essentially a user-defined function that encapsulates a set of APDL commands tailored to perform a particular task. These scripts are systematically arranged in a centralized repository, known as a macro library. After configuring the library to be recognized by the system, any individual script herein can be executed simply by invoking its assigned name.

The developed macro code starts by defining the main input parameters such as material properties, geometric parameters, the power-law index, and porosity parameters. Following parameter definition, the solid volumetric representation of the FGSB with porous core is constructed by employing the Block command, as depicted in Figure 9. As a next step, effective material properties are defined, incorporating the power law distribution by creating a macro function mat_FG that takes the vertical coordinate y_coord as an argument as given in Algorithm 1. The FG properties are then assigned programmatically through a loop structure facilitated by the *DO commands followed in Algorithm 2.

The *Use command is employed to invoke another macro tasked with implementing the power law criteria. Within the loop, the iterative process traverses through the elements in the z-direction, with each iteration assigning the requisite parameters to individual elements, considering the element length as an argument.

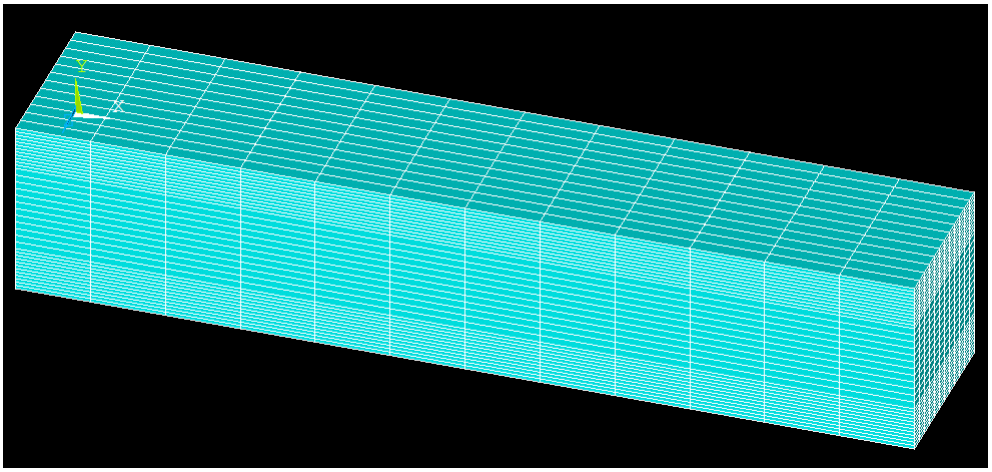

Figure 9. The meshing of an example beam in Ansys using APDL property

Algorithm 1. Defining FG sandwich beam with the porous core in Ansys APDL

```
*CREATE, mat_FG
y_coord = ARG1
!!UD
!EP = (1 – e0*a0)
!DP = SQRT(1 – e0*a0)
!!SD
EP = 1 – e0*(COS(PI*y_coord/(h2 – h1)))
DP = 1 – e1*(COS(PI*y_coord/(h2 – h1)))
!!ASD
!EP = 1 – e0*(COS((PI*y_coord)/(2*(h2 – h1)) + PI/4))
!DP = 1 – e1*(COS((PI*y_coord)/(2*(h2 – h1)) + PI/4))
*IF, y_coord, GE, h0, AND, y_coord, LE, h1, THEN
        V = ((y_coord – h0) / (h1 – h0))**p
        E_FG = (E_c – E_m)*V + E_m
        den_FG = (dens_c – dens_m)*V + dens_m
*ELSEIF, y_coord, GE, h1, AND, y_coord, LE, h2, THEN
        V = 1
        E_FG = ((E_c – E_m)*V + E_m)*EP
        den_FG = ((dens_c – dens_m)*V + dens_m)*DP
*ELSE
        V = ((y_coord– h3) / (h2 – h3))**p
        E_FG = (E_c – E_m)*V + E_m
        den_FG =  (dens_c – dens_m)*V + dens_m
*ENDIF
*END !mat_FG
```

Algorithm 2. Implementation of FG properties in Ansys APDL

```
! FG MATERIAL PROPERTIES
length_e_y = 0.002
ele_numb_y = 1 / length_e_y
locy = –0.5
COUNTER = 1
*DO, j, 1, ele_numb_y + 1, 1
        y_coord = locy + (j – 1) * length_e_y
        *USE, mat_FG, y_coord
        MP, EX, COUNTER, E_FG
        MP, PRXY, COUNTER, n
        MP, DENS, COUNTER, den_FG
        ESEL, S, CENT, Y, locy + (j – 1) * length_e_y, locy + j * length_e_y
        EMODIF, ALL, MAT, COUNTER
        ESEL, ALL
        COUNTER = COUNTER + 1
*ENDDO
```

The porosity distribution patterns are defined and implemented in the core layer of the beam. Then, for meshing, the SOLID186 element is selected to accurately model the gradual property change across the FGSB thickness. To optimize control over mesh quality and size, the LSEL and LESIZE commands are used.

Finally, boundary conditions are imposed on the beam's edges, considering the model's 3D representation. CC and CF boundary conditions are applied. Uniformly distributed surface load and axial force are applied for static and buckling analysis. Subsequently, the mechanical characteristics of the solid model, computed after boundary condition and load applications, are extracted for comparison with those obtained using the developed finite element model, as well as available literature.

3. NUMERICAL RESULTS AND DISCUSSION

3.1. Introduction

This chapter presents numerical examples to validate the proposed models' accuracy, investigating the effects of elastic foundation and core porosity on natural frequencies, buckling load, and static behavior of FGSBs. The influence of several parameters, including power-law index, geometry, boundary conditions, foundation properties, and porosity, on the mechanical characteristics of FGSBs is thoroughly investigated by a parametric study. The material properties used in the study are ceramic (Alumina) with $E_c = 380$ GPa, $\rho_c = 3960\ \text{kg}/m^3$, $\nu_c = 0.3$ and metal (Aluminum) with $E_m = 70$ GPa, $\rho_m = 2702\ \text{kg}/m^3$, $\nu_m = 0.3$. As illustrated in Table 2, three different boundary conditions including simply-supported (SS), clamped-clamped (CC), and clamped-free (CF) are taken into account. This study utilizes nondimensional forms for various parameters including natural frequency, critical buckling load, displacement, normal and shear stresses, and elastic foundation parameters, facilitating analysis and comparison as in the following.

$$\bar{\omega} = \frac{\omega L^2}{h}\sqrt{\frac{\rho_m}{E_m}}, \qquad \bar{N}_{cr} = \frac{12N_{cr}L^2}{E_m h^3}, \qquad \bar{w} = \frac{100E_m h^3}{qL^4}w(x_0, z),$$
$$\bar{\sigma}_x = \frac{h}{qL}\sigma_x(x_0, z), \qquad \bar{\sigma}_z = \frac{h}{qL}\sigma_z(x_0, z), \qquad \bar{\sigma}_{xz} = \frac{h}{qL}\sigma_{xz}(x_0, z) \tag{54}$$
$$K_w = \frac{12k_w L^4}{E_m h^3}, \qquad K_p = \frac{12k_p L^2}{E_m h^3}$$

where $\bar{\omega}$, $\bar{N}_{cr}$, $\bar{w}$ denote the nondimensional natural frequency, critical buckling load, and vertical displacement, respectively. Similarly,$\bar{\sigma}_x$, $\bar{\sigma}_z$, $\bar{\sigma}_{xz}$ represent the axial, vertical, and shear stresses, respectively. The point x_0 specifies the location where the corresponding quantity is evaluated. The parameters K_w and K_p are nondimensional foundation parameters.

3.2. Free Vibration and Buckling Analysis of FGSBs with Navier Method: A Validation Study

This section validates the proposed quasi-3D theory for simply supported FGSBs without an elastic foundation ($K_w = K_p = e_0 = 0$) through free vibration and buckling analysis using a Navier-type analytical solution. The nondimensional fundamental natural frequencies and critical buckling loads of Type A (hardcore) and Type B (softcore) FGSBs are compared in Tables 3-6. The results are benchmarked against previous studies based on HSDT (Vo et al., 2014) and two different quasi-3D theories (Nguyen et al., 2016; Vo et al., 2015a). The present theory shows remarkable concordance with previous investigations that incorporate the impacts of transverse normal deformation phenomena. For Type B beams, comparisons are made only with HSDT due to the lack of available quasi-3D theory results in the literature. The slight differences observed with HSDT are attributed to the transverse normal stress of the present theory, which is neglected in HSDT. Incorporating transverse normal stress generally leads to higher results, highlighting its significance. Additionally, the tables show that an increase in the power-law index reduces the fundamental frequencies and critical buckling loads for Type A beams while increasing them for Type B beams. This behavior is attributed to the changing metal-to-ceramic ratio. A higher power-law index increases the metal fraction in hardcore configurations, making the beams more flexible. Conversely, in softcore configurations, it increases the ceramic fraction, enhancing rigidity.

Figures 10 and 11 illustrate the influence of the power-law index and skin-to-core thickness ratio on fundamental natural frequencies and critical buckling loads. The findings indicate that the skin-core-skin thickness ratios of 1-0-1 and 1-2-1 provide, respectively, the maximum and minimum values of the fundamental natural frequencies and critical buckling loads for Type A and vice versa for Type B. Moreover, the plots reveal that the fundamental natural frequencies and critical buckling loads of Type A beams decrease with increasing power-law index and decreasing core thickness, whereas the opposite trend is evident for Type B beams. These observed trends are attributable to variations in bending stiffness, which exhibit an increase in core thickness and power-law index for Type A beams while demonstrating a decrease for Type B beams.

Table 3. Nondimensional fundamental natural frequencies for Type A beams

p	Theory	$L/h = 5$				$L/h = 20$			
		1-0-1	2-1-2	1-1-1	1-2-1	1-0-1	2-1-2	1-1-1	1-2-1
0	Present	5.1616	5.1616	5.1616	5.1616	5.4610	5.4610	5.4610	5.4610
	HSDT[1]	5.1528	5.1528	5.1528	5.1528	5.4603	5.4603	5.4603	5.4603
	Quasi-3D[1]	5.1620	5.1620	5.1620	5.1620	5.4611	5.4611	5.4611	5.4611
	Quasi-3D[2]	5.1618	5.1618	5.1618	5.1618	5.4610	5.4610	5.4610	5.4610
0.5	Present	4.1342	4.2427	4.3381	4.4879	4.3153	4.4295	4.5330	4.6985
	HSDT[1]	4.1268	4.2351	4.3303	4.4798	4.3148	4.4290	4.5324	4.6979
	Quasi-3D[1]	4.1329	4.2417	4.3373	4.4874	4.3137	4.4284	4.5321	4.6979
	Quasi-3D[2]	4.1344	4.2429	4.3383	4.4881	4.3153	4.4296	4.5330	4.6985
1	Present	3.5801	3.7367	3.8828	4.1183	3.7151	3.8773	4.0333	4.2895
	HSDT[1]	3.5735	3.7298	3.8755	4.1105	3.7147	3.8768	4.0328	4.2889
	Quasi-3D[1]	3.5804	3.7369	3.8830	4.1185	3.7153	3.8774	4.0334	4.2896
	Quasi-3D[2]	3.5803	3.7369	3.883	4.1185	3.7152	3.8773	4.0333	4.2895
2	Present	3.0736	3.2425	3.4255	3.7408	3.1768	3.3469	3.5394	3.8774
	HSDT[1]	3.0680	3.2365	3.4190	3.7334	3.1764	3.3465	3.5389	3.8769
	Quasi-3D[1]	3.0739	3.2428	3.4258	3.7410	3.1769	3.3471	3.5395	3.8775
	Quasi-3D[2]	3.0737	3.2427	3.4257	3.7410	3.1785	3.3488	3.5413	3.8793
5	Present	2.7492	2.8487	3.0236	3.3839	2.8443	2.9314	3.1115	3.4926
	HSDT[1]	2.7446	2.8439	3.0181	3.3771	2.8439	2.9310	3.1111	3.4921
	Quasi-3D[1]	2.7497	2.8491	3.0239	3.3840	2.8444	2.9315	3.1116	3.4927
	Quasi-3D[2]	2.7493	2.8489	3.0238	3.3840	2.8443	2.9314	3.1115	3.4926
10	Present	2.6977	2.7398	2.8858	3.2421	2.8045	2.8191	2.9665	3.3411
	HSDT[1]	2.6932	2.7355	2.8808	3.2356	2.8041	2.8188	2.9662	3.3406
	Quasi-3D[1]	2.6982	2.7402	2.8862	3.2423	2.8046	2.8192	2.9666	3.3412
	Quasi-3D[2]	2.6978	2.7400	2.8860	3.2422	2.8045	2.8191	2.9665	3.3411

HSDT[1] (Vo et al., 2014); Quasi-3D[1] (Nguyen et al., 2016); Quasi-3D[2] (Vo et al., 2015a)

Table 4. Nondimensional fundamental natural frequencies of Type B beams

p	Theory	$L/h = 5$				$L/h = 20$			
		1-0-1	2-1-2	1-1-1	1-2-1	1-0-1	2-1-2	1-1-1	1-2-1
0	Present	2.6819	2.6819	2.6819	2.6819	2.8375	2.8375	2.8375	2.8375
	HSDT[1]	2.6773	2.6773	2.6773	2.6773	2.8371	2.8371	2.8371	2.8371
0.5	Present	4.4501	4.3115	4.1904	3.9979	4.8585	4.7466	4.6300	4.4165
	HSDT[1]	4.4427	4.3046	4.1839	3.9921	4.8579	4.7460	4.6294	4.4160
1	Present	4.8612	4.7260	4.5935	4.3730	5.2997	5.2224	5.1167	4.8944
	HSDT[1]	4.8525	4.7178	4.5858	4.3663	5.2990	5.2217	5.1160	4.8938
2	Present	5.1040	5.0063	4.8828	4.6536	5.5247	5.5120	5.4418	5.2452
	HSDT[1]	5.0945	4.9970	4.8740	4.6459	5.5239	5.5113	5.4410	5.2445
5	Present	5.1976	5.1703	5.0799	4.8650	5.5653	5.6391	5.6250	5.4851
	HSDT[1]	5.1880	5.1603	5.0703	4.8564	5.5645	5.6382	5.6242	5.4843
10	Present	5.1942	5.2066	5.1400	4.9416	5.5309	5.6460	5.6629	5.5583
	HSDT[1]	5.1848	5.1966	5.1301	4.9326	5.5302	5.6452	5.6621	5.5575

HSDT[1] (Vo et al., 2014)

Table 5. Nondimensional critical buckling loads of Type A beams

p	Theory	$L/h = 5$				$L/h = 20$			
		1-0-1	2-1-2	1-1-1	1-2-1	1-0-1	2-1-2	1-1-1	1-2-1
0	Present	49.5906	49.5906	49.5906	49.5906	53.3145	53.3145	53.3145	53.3145
	HSDT[1]	48.5959	48.5959	48.5959	48.5959	53.2364	53.2364	53.2364	53.2364
	Quasi-3D[1]	49.5970	49.5970	49.5970	49.5970	53.3175	53.3175	53.3175	53.3175
	Quasi-3D[2]	49.5906	49.5906	49.5906	49.5906	49.5906	53.3145	53.3145	53.3145
0.5	Present	28.4623	30.6824	32.5698	35.5155	29.7625	32.1021	34.1379	37.3724
	HSDT[1]	27.8574	30.0301	31.8784	34.7653	29.7175	32.2629	34.0862	37.3159
	Quasi-3D[1]	28.4407	30.6650	32.5547	35.5032	29.7410	32.0853	34.1242	37.3626
	Quasi-3D[2]	28.4624	30.6825	32.5699	35.5156	29.7626	32.1022	34.1380	41.8227
1	Present	20.0894	22.7065	25.1075	29.0755	20.7530	23.4572	25.9989	30.2774
	HSDT[1]	19.6525	22.2108	24.5596	28.4447	20.7212	23.4211	25.9588	30.2307
	Quasi-3D[1]	20.0899	22.7061	25.1060	29.0723	20.7541	23.4584	26.0001	30.2785
	Quasi-3D[2]	20.7425	22.7065	25.1075	29.0755	20.7530	23.4572	25.9989	30.2774
2	Present	13.8838	16.2761	18.7772	23.3042	14.2190	16.6307	19.2299	24.0276
	HSDT[1]	13.5801	15.9152	18.3587	22.7863	14.1973	16.6050	19.3116	23.9900
	Quasi-3D[1]	13.8852	16.2761	18.7756	23.3002	14.2199	16.6317	19.2309	24.0284
	Quasi-3D[2]	13.8839	16.2761	18.7772	23.3042	14.2190	16.6307	19.2299	24.0276
5	Present	10.3673	11.9301	14.0352	18.5092	10.6330	12.1068	14.2505	18.9172
	HSDT[1]	10.1460	11.6676	13.7212	18.0914	10.6171	12.0883	14.2284	18.8874
	Quasi-3D[1]	10.3708	11.9320	14.0352	18.5058	10.6341	12.1078	14.2515	18.9180
	Quasi-3D[2]	10.3673	11.9301	14.0353	18.5092	10.6330	12.1068	14.2505	18.9172
10	Present	9.6535	10.7689	12.5393	16.7574	9.9994	10.9239	12.7014	17.0712
	HSDT[1]	9.4515	10.5348	12.2605	16.3783	9.9847	10.9075	12.6819	17.0443
	Quasi-3D[1]	9.6573	10.7715	12.5402	16.7550	10.0003	10.9246	12.7023	17.0723
	Quasi-3D[2]	9.6535	10.7689	12.5393	16.7574	9.9995	10.9239	12.7014	17.0712

HSDT[1] (Vo et al., 2014); Quasi-3D[1] (Nguyen et al., 2016); Quasi-3D[2] (Vo et al., 2015a)

Table 6. Nondimensional critical buckling loads of Type B beams

p	Theory	$L/h = 5$				$L/h = 20$			
		1-0-1	2-1-2	1-1-1	1-2-1	1-0-1	2-1-2	1-1-1	1-2-1
0	Present	9.1351	9.1351	9.1351	9.1351	9.8211	9.8211	9.8211	9.8211
	HSDT[1]	8.9519	8.9519	8.9519	8.9519	9.8067	9.8067	9.8067	9.8067
0.5	Present	28.9557	26.4203	24.4839	21.7615	33.2659	30.8982	28.8571	25.6412
	HSDT[1]	28.4280	25.9503	24.0540	21.3821	33.2187	30.8546	28.8167	25.6086
1	Present	36.8893	33.4917	30.7778	26.9366	42.2413	39.4682	36.8962	32.6255
	HSDT[1]	36.2103	32.8974	30.2449	26.4801	42.1810	39.4124	36.8445	32.5803
2	Present	43.2667	39.5732	36.3395	31.5445	48.7919	46.2696	43.6024	38.7731
	HSDT[1]	42.4501	38.8589	35.7058	31.0152	48.7215	46.2035	43.5408	38.7192
5	Present	47.5776	44.3595	41.0572	35.6386	52.4419	50.8343	48.5858	43.8252
	HSDT[1]	46.6504	43.5338	40.3235	35.0357	52.3655	50.7608	48.5163	43.7637
10	Present	48.7461	45.9842	42.8470	37.3250	53.1108	52.0560	50.1623	45.6685
	HSDT[1]	47.7825	45.1141	42.0693	36.6874	53.0331	51.9804	50.0902	45.6040

HSDT[1] (Vo et al., 2014)

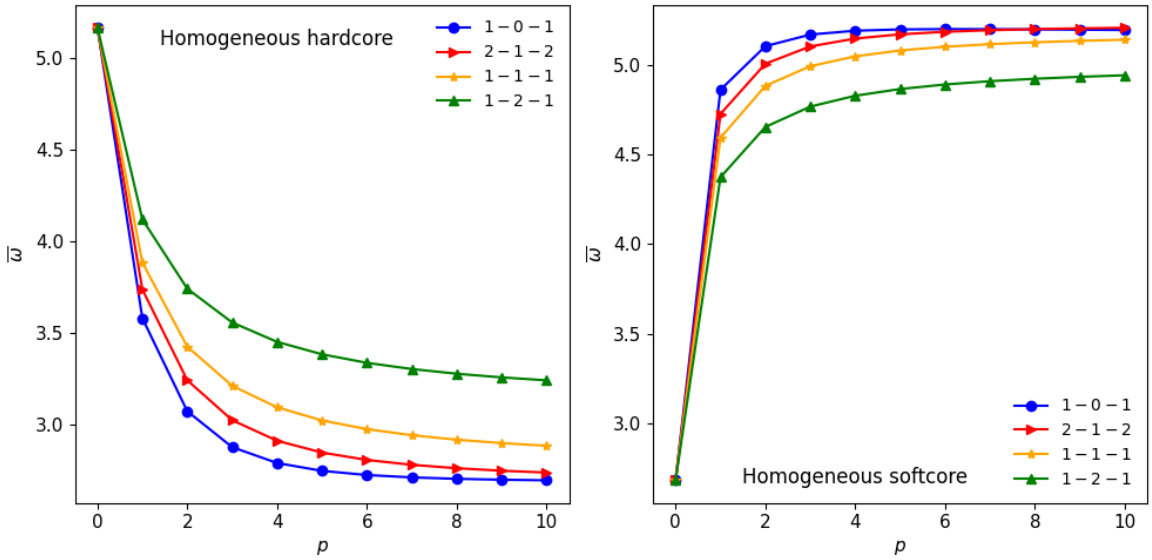

Figure 10. Effect of skin-core-skin thickness ratios on fundamental natural frequencies of FGSBs ($L/h = 5$)

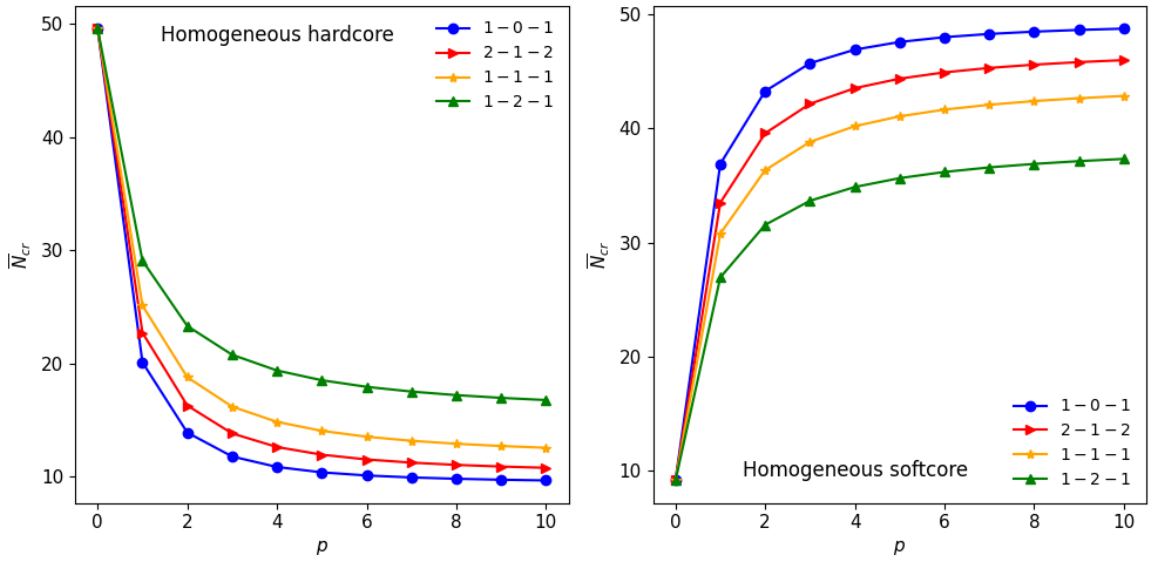

Figure 11. Effect of skin-core-skin thickness ratios on critical buckling loads of FGSBs ($L/h = 5$)

3.3. Free Vibration and Buckling Analysis of FGSBs with Porous Core Resting on Elastic Foundation Using Ritz Method

3.3.1. Convergence and Validation Study

First, free vibration and buckling analyses of FGSBs without elastic foundation ($K_w = K_p = e_0 = 0$) are performed to demonstrate the accuracy of the Ritz solution. In solution,

Type A and Type C beams are considered under different boundary conditions. Tables 7 and 8 evaluate the convergency by comparing results with existing studies and adjusting the number of terms in displacement functions. The results demonstrate strong agreement with previous studies, confirming the accuracy of the proposed method. Rapid convergence for SS beams is achieved with only six polynomial terms for both fundamental natural frequencies and critical buckling loads. In contrast, with CC and CF boundary conditions, a polynomial expansion of ten terms yields consistent outcomes. To ensure accuracy, a polynomial expansion with 12 terms is used in the entire analysis.

Table 7. Convergence study of fundamental natural frequencies of the beams

Beam	Number of terms	$L/h = 5$			$L/h = 20$		
		SS	CC	CF	SS	CC	CF
Type A	2	5.7211	10.5892	1.9446	6.1120	12.7199	1.9904
	4	5.1631	10.3361	1.9232	5.4627	12.5089	1.9676
	6	5.1616	10.2375	1.9158	5.4610	12.4158	1.9572
	8	5.1616	10.2004	1.9083	5.4610	12.3620	1.9551
	10	5.1616	10.1905	1.9060	5.4610	12.3287	1.9535
	12	5.1616	10.1889	1.9053	5.4610	12.2689	1.9529
	14	5.1616	10.1889	1.9051	5.4610	12.2678	1.9525
	HSDT[1]	5.1528	10.0726	1.8953	5.4603	12.2243	1.9496
	Quasi-3D[1]	5.1618	10.1851	1.9055	5.4610	12.2660	1.9527
	Quasi-3D[2]	5.1620	10.1790	1.9053	5.4611	12.2756	1.9530
Type C	2	4.5545	8.7409	1.9237	4.7760	9.9450	1.9814
	4	4.1151	8.5570	1.5385	4.2884	9.7972	1.5848
	6	4.0996	8.4879	1.5176	4.2713	9.7343	1.5631
	8	4.0996	8.4609	1.5064	4.2713	9.6977	1.5425
	10	4.0996	8.4536	1.5022	4.2713	9.6751	1.5316
	12	4.0996	8.4525	1.4976	4.2713	9.6545	1.5254
	14	4.0996	8.4521	1.4967	4.2713	9.6537	1.5247
	HSDT[1]	4.0691	8.3282	1.4840	4.2445	9.5451	1.5145
	Quasi-3D[2]	4.0996	8.4529	1.5001	4.2711	9.6404	1.5264

HSDT[1] (Vo et al., 2014); Quasi-3D[1] (Vo et al., 2015a); Quasi-3D[2] (Nguyen et al., 2016)

Table 8. Convergence study of nondimensional critical buckling loads of the beams

Beam	Number of terms	$L/h = 5$			$L/h = 20$		
		SS	CC	CF	SS	CC	CF
Type A	2	59.9462	169.0097	13.5748	65.7932	237.5850	13.9360
	4	49.6171	160.906	13.2311	53.3455	215.8920	13.4785
	6	49.5906	160.4934	13.1624	53.3145	213.4197	13.4434
	8	49.5906	160.3466	13.1281	53.3145	212.3458	13.4152
	10	49.5906	160.2947	13.1212	53.3145	211.7269	13.4082
	12	49.5906	160.2827	13.1178	53.3145	211.2154	13.3994
	14	49.5906	160.2826	13.116	53.3145	210.7338	13.3986
	HSDT[1]	48.5964	152.1588	13.0595	53.2364	208.9515	13.3730
	Quasi-3D[1]	49.5906	160.278	13.1224	53.3145	210.742	13.3981
	Quasi-3D[2]	49.5970	160.3064	13.1138	53.3175	210.7774	13.3993
Type C	2	34.9926	106.5478	7.7762	36.9892	133.6806	7.9017
	4	28.9944	100.9301	7.5179	30.2468	121.9511	7.6237
	6	28.7881	100.6826	7.4875	30.0195	120.7138	7.5542
	8	28.7881	100.5983	7.4571	30.0195	120.1792	7.5464
	10	28.7881	100.5701	7.4419	30.0195	119.8711	7.5387
	12	28.7881	100.5629	7.4267	30.0195	119.7826	7.5310
	14	28.7881	100.5588	7.4236	30.0195	119.6879	7.5279
	HSDT[1]	27.9314	94.6117	7.3149	29.6120	117.0384	7.4254
	Quasi-3D[2]	28.7884	100.5883	7.4344	30.0168	119.4172	7.5312

HSDT[1] (Vo et al., 2014); Quasi-3D[1] (Vo et al., 2015a); Quasi-3D[2] (Nguyen et al., 2016)

A comparison of fundamental natural frequencies and critical buckling loads of FGSBs is presented in Tables 9-12. Comparison of Ritz solution results with existing HSDT (Vo et al., 2014) and two different Quasi-3D theories (Nguyen et al., 2016; Vo et al., 2015a) demonstrated excellent agreement, similar to the Navier solution, confirming the accuracy of the proposed theory.

For the sake of completeness, Tables 13 and 14 display the first three natural frequencies of 1-2-1 configured FGSBs. The consideration of normal strain effects leads to higher results. This observation underscores the significance of incorporating the normal strain effect.

Table 9. Fundamental natural frequencies of Type A beams

L/h	BC	Theory	p					
			0	0.5	1	2	5	10
5	SS	Present	5.1616	4.4879	4.1183	3.7408	3.3839	3.2421
		HSDT[1]	5.1528	4.4791	4.1105	3.7334	3.3771	3.2357
		Quasi-3D[1]	5.1620	4.4874	4.1185	3.7410	3.3840	3.2423
		Quasi-3D[2]	5.1618	4.4881	4.1185	3.7410	3.3840	3.2422
	CC	Present	10.1889	9.1035	8.4730	7.8074	7.1602	6.8978
		HSDT[1]	10.0726	8.9969	8.3747	7.7149	7.0723	6.8119
		Quasi-3D[1]	10.1790	9.0924	8.4653	7.8008	7.1550	6.8934
		Quasi-3D[2]	10.1851	9.1036	8.4752	7.8114	7.1652	6.9030
	CF	Present	1.9053	1.6470	1.5073	1.3651	1.2298	1.1795
		HSDT[1]	1.8953	1.6383	1.4993	1.3582	1.2258	1.1734
		Quasi-3D[1]	1.9053	1.6467	1.5071	1.3653	1.2323	1.1798
		Quasi-3D[2]	1.9055	1.6474	1.5075	1.3658	1.2329	1.1804
20	SS	Present	5.4610	4.6985	4.2895	3.8774	3.4926	3.3411
		HSDT[1]	5.4603	4.6972	4.2889	3.8769	3.4921	3.3406
		Quasi-3D[1]	5.4611	4.6979	4.2896	3.8775	3.4927	3.3412
		Quasi-3D[2]	5.4610	4.6985	4.2895	3.8774	3.4926	3.3411
	CC	Present	12.3091	10.6204	9.7091	8.7877	7.9246	7.5841
		HSDT[1]	12.2243	10.5455	9.6419	8.7268	7.8696	7.5315
		Quasi-3D[1]	12.2756	10.5924	9.6866	8.7690	7.9092	7.5700
		Quasi-3D[2]	12.2660	10.5842	9.6768	8.7593	7.9000	7.5609
	CF	Present	1.9529	1.6800	1.5331	1.3857	1.2480	1.1938
		HSDT[1]	1.9496	1.6764	1.5304	1.3831	1.2456	1.1915
		Quasi-3D[1]	1.9530	1.6796	1.5335	1.3860	1.2484	1.1943
		Quasi-3D[2]	1.9527	1.6794	1.5329	1.3855	1.2478	1.1937

HSDT[1] (Vo et al., 2014); Quasi-3D[1] (Vo et al., 2015a); Quasi-3D[2] (Nguyen et al., 2016)

Table 10. Fundamental natural frequencies of Type C beams

L/h	BC	Theory	p					
			0	0	0	0	0	0
5	SS	Present	4.0996	3.8439	3.7165	3.6112	3.5512	3.5417
		HSDT[1]	4.0691	3.7976	3.6636	3.553	3.4914	3.483
		Quasi-3D[1]	4.0996	3.8438	3.7172	3.6119	3.5513	3.5413
	CC	Present	8.4525	7.8932	7.5894	7.2903	7.0071	6.8818
		HSDT[1]	8.3282	7.7553	7.4487	7.1485	6.8702	6.7543
		Quasi-3D[1]	8.4529	7.8924	7.5904	7.2898	7.0032	6.8757
	CF	Present	1.4977	1.4054	1.3579	1.3247	1.3085	1.3087
		HSDT[1]	1.484	1.3865	1.3393	1.3022	1.2857	1.2867
		Quasi-3D[1]	1.5001	1.4076	1.3627	1.3273	1.3113	1.3118
20	SS	Present	4.2713	4.0146	3.8916	3.7995	3.7702	3.7826
		HSDT[1]	4.2445	3.9695	3.8387	3.7402	3.7081	3.7214
		Quasi-3D[1]	4.2711	4.0143	3.8923	3.8003	3.7708	3.7831
	CC	Present	9.6546	9.0658	8.7809	8.5613	8.4741	8.488
		HSDT[1]	9.5451	8.9243	8.6264	8.3959	8.3047	8.3205
		Quasi-3D[1]	9.6404	9.0524	8.7701	8.5509	8.4627	8.4755
	CF	Present	1.5255	1.4337	1.3897	1.357	1.3469	1.3516
		HSDT[1]	1.5145	1.4165	1.37	1.335	1.3241	1.3292
		Quasi-3D[1]	1.5264	1.4344	1.3907	1.358	1.3478	1.3525

HSDT[1] (Vo et al., 2014); Quasi-3D[1] (Nguyen et al., 2016)

Table 11. Critical buckling loads of Type A beams

L/h	BC	Theory	p					
			0	0.5	1	2	5	10
5	SS	Present	49.5906	35.5156	29.0755	23.3042	18.5092	16.7574
		HSDT[1]	48.5964	34.7546	28.4440	22.7859	18.0915	16.3789
		Quasi-3D[1]	49.5970	35.5032	29.0723	23.3002	18.5058	16.7550
		Quasi-3D[2]	49.5906	35.5156	29.0755	23.3042	18.5092	16.7574
	CC	Present	160.2823	120.8531	101.5976	83.5970	68.0331	62.1798
		HSDT[1]	152.1588	114.1312	95.7230	78.5570	63.7847	58.2532
		Quasi-3D[1]	160.3064	120.7931	101.5703	83.5671	68.0098	62.1634
		Quasi-3D[2]	160.2780	120.8630	101.6130	83.6159	68.0510	62.1959
	CF	Present	13.1178	9.2495	7.5009	5.9643	4.7067	4.2529
		HSDT[1]	13.0595	9.1913	7.4638	5.9347	4.6806	4.2268
		Quasi-3D[1]	13.1138	9.2289	7.4948	5.9601	4.7028	4.2480
		Quasi-3D[2]	13.1224	9.2404	7.5028	5.9674	4.7088	4.2533
20	SS	Present	53.3145	37.3725	30.2774	24.0276	18.9172	17.0712
		HSDT[1]	53.2364	37.3054	30.2306	23.9899	18.8874	17.0445
		Quasi-3D[1]	53.3175	37.3626	30.2785	24.0284	18.9180	17.0723
		Quasi-3D[2]	53.3145	41.8227	30.2774	24.0276	18.9172	17.0712
	CC	Present	210.9101	148.9308	120.5266	95.5647	75.8993	68.3893
		HSDT[1]	208.9515	147.0614	119.4215	94.9558	74.8903	67.6281
		Quasi-3D[1]	210.7774	148.4165	120.5619	95.8941	75.6538	68.3252
		Quasi-3D[2]	210.7420	148.4130	120.5090	95.8403	75.6019	68.2737
	CF	Present	13.3994	9.3805	7.5979	6.0267	4.7436	4.2801
		HSDT[1]	13.3730	9.3607	7.5815	6.0134	4.7323	4.2698
		Quasi-3D[1]	13.3993	9.3806	7.5986	6.0278	4.7443	4.2809
		Quasi-3D[2]	13.3981	9.3815	7.5965	6.0257	4.7423	4.2789

HSDT[1] (Vo et al., 2014); Quasi-3D[1] (Vo et al., 2015a); Quasi-3D[2] (Nguyen et al., 2016)

Table 12. Critical buckling loads of Type C beams

L/h	BC	Theory	p					
			0	0	0	0	0	0
5	SS	Present	28.7881	23.8572	21.6294	19.7893	18.5216	18.1383
		HSDT[1]	27.9314	22.9869	20.7762	18.9588	17.7320	17.3775
		Quasi-3D[1]	28.7884	23.8554	21.6374	19.7957	18.5212	18.1329
	CC	Present	100.5629	82.4770	73.9112	66.1354	59.3243	56.4987
		HSDT[1]	94.6117	77.5129	69.4877	62.2249	55.9446	53.3734
		Quasi-3D[1]	100.5883	82.4783	73.9348	66.1308	59.2628	56.4049
	CF	Present	7.4419	6.1872	5.6280	5.1823	4.9148	4.8580
		HSDT[1]	7.3149	6.0286	5.4629	5.0154	4.7534	4.7024
		Quasi-3D[1]	7.4344	6.1836	5.6304	5.1884	4.9228	4.8658
20	SS	Present	30.0195	24.9952	22.7720	21.0254	20.0317	19.8573
		HSDT[1]	29.6120	24.4140	22.1386	20.3581	19.3639	19.2058
		Quasi-3D[1]	30.0168	24.9914	22.7796	21.0343	20.0386	19.8622
	CC	Present	119.7827	99.5671	90.5848	83.4516	79.1967	78.3045
		HSDT[1]	117.0384	96.4573	87.4069	80.2465	76.0539	75.2379
		Quasi-3D[1]	119.4172	99.2742	90.3696	83.2627	79.0045	78.0989
	CF	Present	7.5310	6.2704	5.7129	5.2760	5.0305	4.9898
		HSDT[1]	7.4254	6.1225	5.5529	5.1084	4.8634	4.8269
		Quasi-3D[1]	7.5312	6.2702	5.7160	5.2800	5.0345	4.9934

HSDT[1] (Vo et al., 2014); Quasi-3D[1] (Nguyen et al., 2016)

Table 13. Comparison of first three natural frequencies in Type A beams

Mode	BCs	Theory	p					
			0	0.5	1	2	5	10
1	SS	Present	5.1616	4.4879	4.1183	3.7408	3.3839	3.2421
		HSDT[1]	5.1528	4.4798	4.1105	3.7334	3.3771	3.2356
	CC	Present	10.1889	9.1035	8.4730	7.8074	7.1602	6.8978
		HSDT[1]	10.0678	8.9942	8.3705	7.7114	7.0691	6.8087
	CF	Present	1.9053	1.6491	1.5076	1.3644	1.2298	1.1765
		HSDT[1]	1.8953	1.6383	1.4993	1.3582	1.2258	1.1734
2	SS	Present	17.9716	15.9653	14.8131	13.6019	12.4251	11.9483
		HSDT[1]	17.8812	15.8764	14.7246	13.6410	13.1852	12.9630
	CC	Present	24.3794	22.1509	20.8095	19.3609	17.9208	17.3265
		HSDT[1]	24.1007	21.8773	20.5397	19.0954	17.6608	17.0706
	CF	Present	10.3443	9.1033	8.4282	7.7036	7.0146	6.7334
		HSDT[1]	10.2454	9.0656	8.3933	7.6906	7.0127	6.7397
3	SS	Present	34.4899	31.2242	29.2701	27.1617	25.0616	24.1937
		HSDT[1]	34.2097	30.9311	28.9684	26.8553	24.7627	23.9043
	CC	Present	39.3867	36.3538	34.4902	32.4493	30.3894	29.5258
		HSDT[1]	39.0057	35.9260	34.0378	31.9753	29.9060	29.0452
	CF	Present	15.2148	14.8493	14.1430	13.7221	13.2608	13.0360
		HSDT[1]	15.1167	14.7909	14.0571	13.6410	13.1852	12.9631

HSDT[1] (Vo et al., 2014)

Table 14. Comparison of first three natural frequencies in Type C beams

Mode	BCs	Theory	p					
			0	0.5	1	2	5	10
1	SS	Present	4.0996	3.8439	3.7165	3.6112	3.5512	3.5417
		HSDT[2]	4.0691	3.7976	3.6636	3.5530	3.4914	3.4830
	CC	Present	8.4525	7.8932	7.5894	7.2903	7.0071	6.8818
		HSDT[2]	8.3282	7.7553	7.4487	7.1485	6.8702	6.7543
	CF	Present	1.4977	1.4054	1.3579	1.3247	1.3085	1.3087
		HSDT[2]	1.4840	1.3865	1.3393	1.3022	1.2857	1.2867
2	SS	Present	14.7402	13.7534	13.2273	12.7289	12.2980	12.1255
		HSDT[2]	14.5921	13.5629	13.0215	12.5117	12.0822	11.9168
	CC	Present	20.7864	19.3438	18.5249	17.6623	16.7505	16.3147
		HSDT[2]	19.8886	18.4463	17.6290	16.7552	15.8266	15.3878
	CF	Present	8.3244	7.7465	7.4544	7.2071	7.0590	7.0332
		HSDT[2]	8.3149	7.7255	7.4173	7.1308	6.8984	6.8139
3	SS	Present	29.1374	27.0784	25.9265	24.7440	23.4231	22.7558
		HSDT[2]	28.7653	26.6542	25.4901	24.3022	23.1254	22.5934
	CC	Present	34.5185	32.0116	30.5248	28.8733	27.0258	26.1303
		HSDT[2]	34.0624	31.5260	30.0458	28.4068	26.5927	25.7241
	CF	Present	14.1911	13.3194	12.8188	12.2643	11.6436	11.3344
		HSDT[2]	14.0712	13.2130	12.7196	12.1683	11.5477	11.2377

HSDT[2](Nguyen et al., 2015)

3.3.2. Porosity Effect

The fundamental natural frequencies for the 1-2-1 configured FGSBs are computed here in Tables 15 and 16, considering three core porosity patterns with varying porosity coefficient values (e_0= 0.4, 0.6, 0.8) To investigate the influence of the elastic foundation, three distinct foundation models are considered: no foundation, Winkler, and Pasternak. Regardless of boundary conditions, beam type, porosity pattern, or length-to-thickness ratio, a consistent increase in fundamental natural frequency is observed with increasing porosity coefficient. This trend is attributed to the simultaneous reduction in both bending stiffness and mass density of the beam due to increased porosity. An exception to the general trend is observed for CC beams with (L/h = 5), where increasing the porosity coefficient of UD leads to a decrease in nondimensional fundamental natural frequencies. This anomaly is attributed to the fact that CC beams experience a more pronounced reduction in bending stiffness relative to mass density at lower length-to-thickness ratios. A

descending order of fundamental natural frequencies is observed for FGSBs with porosity patterns ranging from symmetrical to asymmetrical to uniform. Additionally, it also highlighted that Type A beams (FG face layers, porous core) exhibit higher fundamental natural frequencies than Type C (isotropic face layers, FG porous core). This difference can be attributed to the superior bending stiffness offered by the FG face layers in Type A beams.

Similarly, the variation of critical buckling loads of the beams as a function of the porosity coefficient is tabulated in Tables 17 and 18 The critical buckling loads decrease as the porosity coefficient increases, regardless of porosity pattern or L/h ratio. This is due to the resulting decrease in bending stiffness caused by the increased porosity. Additionally, the incorporation of an elastic foundation leads to an increase in both fundamental natural frequencies and critical buckling loads. This positive impact is further magnified by the inclusion of a shear layer, which significantly improves the beam's shear stiffness, resulting in enhanced dynamic properties and buckling resistance.

The influence of the porosity coefficient on fundamental natural frequencies and critical buckling loads of SS beams is depicted in Figures 12 and 13 for three different cases: Case 1 (K_w = 0 and K_p = 0), Case 2 (K_w = 10 and K_p = 0), and Case 3 (K_w = 10 and K_p = 10). As expected, across all cases and porosity distribution types, fundamental natural frequencies increase as the porosity coefficient increases. Regarding the critical buckling loads, a notable decrease is observed across all scenarios in conjunction with an increase in the porosity coefficient. The incorporation of the Winkler parameter enhances the stiffness of the foundation, leading to increased support and stability, which in turn results in slightly higher fundamental natural frequencies and critical buckling loads. The Pasternak foundation in Case 3 significantly enhances both fundamental natural frequencies and critical buckling loads by increasing shear stiffness, leading to improved overall structural performance.

Table 15. Fundamental natural frequencies variation in the Type A beam with different BCs, porosity distributions, and elastic foundation (1-2-1, $p = 2$)

L/h	K_w	K_p	BCs	e_0								
				UD			SD			ASD		
				0.4	0.6	0.8	0.4	0.6	0.8	0.4	0.6	0.8
5	0	0	SS	3.7340	3.7395	3.7596	3.7955	3.8435	3.9265	3.7469	3.7634	3.8073
			CC	7.6835	7.6105	7.5130	7.7741	7.7695	7.7964	7.7100	7.6723	7.6691
			CF	1.3666	1.3720	1.3855	1.3908	1.4130	1.4504	1.3712	1.3798	1.3993
	100	0	SS	4.5463	4.5934	4.6724	4.5969	4.6784	4.8075	4.5568	4.6127	4.7105
			CC	8.1112	8.0670	8.0129	8.1970	8.2175	8.2788	8.1364	8.1251	8.1585
			CF	2.9499	3.0184	3.1201	2.9611	3.0370	3.1490	2.9520	3.0218	3.1261
	100	10	SS	5.2256	5.3030	5.4246	5.2697	5.3767	5.5412	5.2348	5.3196	5.4571
			CC	8.5746	8.5561	8.5428	8.6545	8.6970	8.7893	8.5977	8.6113	8.6783
			CF	3.3922	3.4724	3.5907	3.4027	3.4901	3.6189	3.3942	3.4761	3.5977
20	0	0	SS	3.8889	3.9102	3.9575	3.9590	4.0282	4.1430	3.9024	3.9329	3.9970
			CC	8.8032	8.8421	8.9332	8.9642	9.1095	9.3522	8.8334	8.8947	9.0285
			CF	1.3900	1.3978	1.4151	1.4152	1.4402	1.4817	1.3946	1.4053	1.4278
	100	0	SS	4.6931	4.7531	4.8541	4.7512	4.8506	5.0065	4.7042	4.7718	4.8864
			CC	9.1866	9.2457	9.3648	9.3410	9.5017	9.7653	9.2156	9.2959	9.4558
			CF	2.9755	3.0459	3.1507	2.9873	3.0656	3.1811	2.9777	3.0494	3.1564
	100	10	SS	5.3699	5.4588	5.6001	5.4208	5.5439	5.7327	5.3796	5.4751	5.6281
			CC	9.6358	9.7170	9.8669	9.7830	9.9608	10.2477	9.6634	9.7649	9.9536
			CF	3.4309	3.5147	3.6385	3.4423	3.5338	3.6683	3.4330	3.5181	3.6442

Table 16. Fundamental natural frequencies variation in tType C beam with different BCs, porosity distributions, and elastic foundations (1-2-1, $p = 2$)

L/h	K_w	K_p	BCs	e_0								
				UD			SD			ASD		
				0.4	0.6	0.8	0.4	0.6	0.8	0.4	0.6	0.8
5	0	0	SS	3.6131	3.6166	3.6252	3.6202	3.6343	3.6699	3.5868	3.5827	3.5982
			CC	7.1821	7.1078	7.0064	7.1954	7.1519	7.1350	7.1899	7.1532	7.1537
			CF	1.3293	1.3341	1.3423	1.3319	1.3403	1.3572	1.3175	1.3174	1.3246
	100	0	SS	4.5056	4.5472	4.6100	4.5102	4.5594	4.6422	4.4810	4.5140	4.5784
			CC	7.6747	7.6293	7.5704	7.6866	7.6692	7.6875	7.6795	7.6670	7.6990
			CF	3.0202	3.0823	3.1709	3.0198	3.0824	3.1728	3.0099	3.0662	3.1486
	100	10	SS	5.2393	5.3077	5.4086	5.2423	5.3167	5.4334	5.2151	5.2740	5.3729
			CC	8.1957	8.1757	8.1538	8.2063	8.2123	8.2622	8.1996	8.2100	8.2721
			CF	3.4738	3.5479	3.6521	3.4732	3.5477	3.6541	3.4640	3.5327	3.6317
20	0	0	SS	3.8258	3.8479	3.8853	3.8341	3.8659	3.9254	3.7865	3.7894	3.8139
			CC	8.6112	8.6496	8.7160	8.6324	8.6938	8.8141	8.5324	8.5337	8.5834
			CF	1.3666	1.3747	1.3885	1.3695	1.3811	1.4026	1.3524	1.3535	1.3623
	100	0	SS	4.7030	4.7598	4.8459	4.7088	4.7729	4.8756	4.6676	4.7065	4.7787
			CC	9.0349	9.0918	9.1843	9.0548	9.1330	9.2761	8.9578	8.9784	9.0532
			CF	3.0591	3.1225	3.2137	3.0591	3.1230	3.2159	3.0475	3.1039	3.1871
	100	10	SS	5.4315	5.5139	5.6357	5.4358	5.5238	5.6591	5.3980	5.4628	5.5694
			CC	9.5264	9.6032	9.7237	9.5447	9.6413	9.8091	9.4515	9.4927	9.5949
			CF	3.5335	3.6084	3.7158	3.5332	3.6084	3.7174	3.5210	3.5883	3.6867

Table 17. Variation of critical buckling loads in Type A beam with different BCs, porosity distributions, and elastic foundation (1-2-1, p = 2)

L/h	K_w	K_p	BCs	e_0								
				UD			SD			ASD		
				0.4	0.6	0.8	0.4	0.6	0.4	0.4	0.6	0.8
5	0	0	SS	21.3657	20.2548	18.9225	22.0740	21.3962	20.6426	21.5128	20.5144	19.4103
			CC	74.7905	69.4866	62.7953	76.6269	72.5125	67.7025	75.3003	70.5921	65.3321
			CF	5.5147	5.2602	4.9660	5.7115	5.5772	5.4374	5.5528	5.3228	5.0715
	100	0	SS	31.6589	30.5466	29.2119	32.3667	31.6873	30.9314	31.8055	30.8050	29.6979
			CC	82.5193	77.1994	70.4687	84.3587	80.2213	75.3787	83.0122	78.2915	72.9650
			CF	18.2614	17.8000	17.0161	18.5799	18.3254	17.8535	18.3301	17.9280	17.2812
	100	10	SS	41.8086	40.6944	39.3568	42.5163	41.8350	41.0766	41.9547	40.9519	39.8413
			CC	92.5929	87.0757	80.5032	94.5790	90.4331	85.5785	93.2328	88.5127	83.2193
			CF	28.3124	27.9254	27.0208	28.6276	28.4458	27.8657	28.3801	28.0510	27.2890
20	0	0	SS	22.2327	21.2404	20.1082	23.0406	22.5426	22.0389	22.3863	21.4886	20.5116
			CC	88.7475	84.6495	79.9134	92.0751	89.9084	87.6527	89.3584	85.6542	81.6041
			CF	5.5757	5.3289	5.0483	5.7794	5.6572	5.5346	5.6143	5.3909	5.1480
	100	0	SS	32.3772	31.3849	30.2526	33.1851	32.6870	32.1833	32.5307	31.6330	30.6558
			CC	96.3111	92.2107	87.4713	99.6286	97.4592	95.2023	96.9223	93.2161	89.1634
			CF	18.8488	18.4127	17.8847	19.1980	18.9880	18.7600	18.9159	18.5245	18.0737
	100	10	SS	42.3893	41.3970	40.2648	43.1972	42.6992	42.1954	42.5429	41.6450	40.6678
			CC	106.3553	102.2549	97.5153	109.6710	107.5032	105.2453	106.9664	103.2599	99.2067
			CF	28.8525	28.4196	27.8896	29.2016	28.9947	28.7646	28.9196	28.5313	28.0784

Table 18. Critical buckling loads variation in Type C beam with different BCs, porosity distributions, and elastic foundation (1-2-1, p = 2)

L/h	K_w	K_p	BCs	e_0								
				UD			SD			ASD		
				0.4	0.6	0.8	0.4	0.6	0.4	0.4	0.6	0.8
5	0	0	SS	18.4505	17.6256	16.5807	18.5452	17.8364	17.0510	18.2592	17.4207	16.5241
			CC	59.9082	56.0255	51.0725	60.1818	56.7935	53.0494	60.1593	56.9407	53.5454
			CF	4.8774	4.6928	4.4632	4.9031	4.7457	4.5730	4.8051	4.5971	4.3737
	100	0	SS	28.6857	27.8577	26.8086	28.7793	28.0673	27.2781	28.4918	27.6493	26.7482
			CC	67.4852	63.5730	58.5729	67.7577	64.3429	60.5648	67.7383	64.5013	61.0850
			CF	16.5588	16.1779	15.5399	16.6078	16.2922	15.8114	16.4870	16.1234	15.5965
	100	10	SS	38.7805	37.9493	36.8958	38.8732	38.1579	37.3649	38.5840	37.7376	36.8321
			CC	77.6273	73.7068	68.6953	77.8981	74.4753	70.6880	77.8805	74.6363	71.2125
			CF	26.4773	26.0803	25.4916	26.5272	26.1962	25.7636	26.4062	26.0285	25.5489
20	0	0	SS	19.8404	19.1279	18.2491	19.9476	19.3433	18.6835	19.5177	18.6858	17.7912
			CC	78.4902	75.5173	71.8214	78.9533	76.4193	73.6396	77.3022	73.9432	70.3357
			CF	4.9816	4.8049	4.5875	5.0085	4.8587	4.6953	4.8991	4.6910	4.4672
	100	0	SS	29.9807	29.2680	28.3890	30.0878	29.4833	28.8232	29.6577	28.8255	27.9306
			CC	86.0464	83.0712	79.3719	86.4631	83.9298	81.1505	84.8582	81.4971	77.8871
			CF	17.7401	17.4016	16.9640	17.7904	17.5053	17.1800	17.5894	17.1908	16.7422
	100	10	SS	39.9887	39.2759	38.3966	40.0957	39.4910	38.8308	39.6654	38.8330	37.9378
			CC	96.0753	93.0995	89.3994	96.4917	93.9578	91.1776	94.8863	91.5241	87.9131
			CF	27.7350	27.3972	26.9598	27.7854	27.5010	27.1759	27.5845	27.1865	26.7382

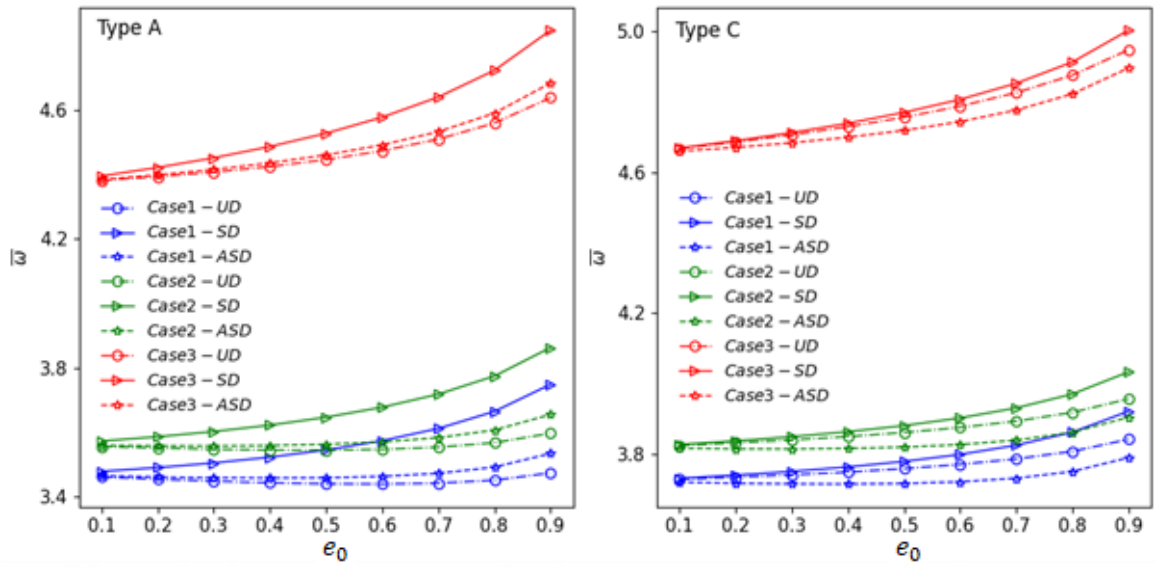

Figure 12. Porosity coefficient effect on fundamental frequencies of SS beams under various porosity distributions and elastic foundations (1-2-1, $L/h = 10$, $p = 5$)

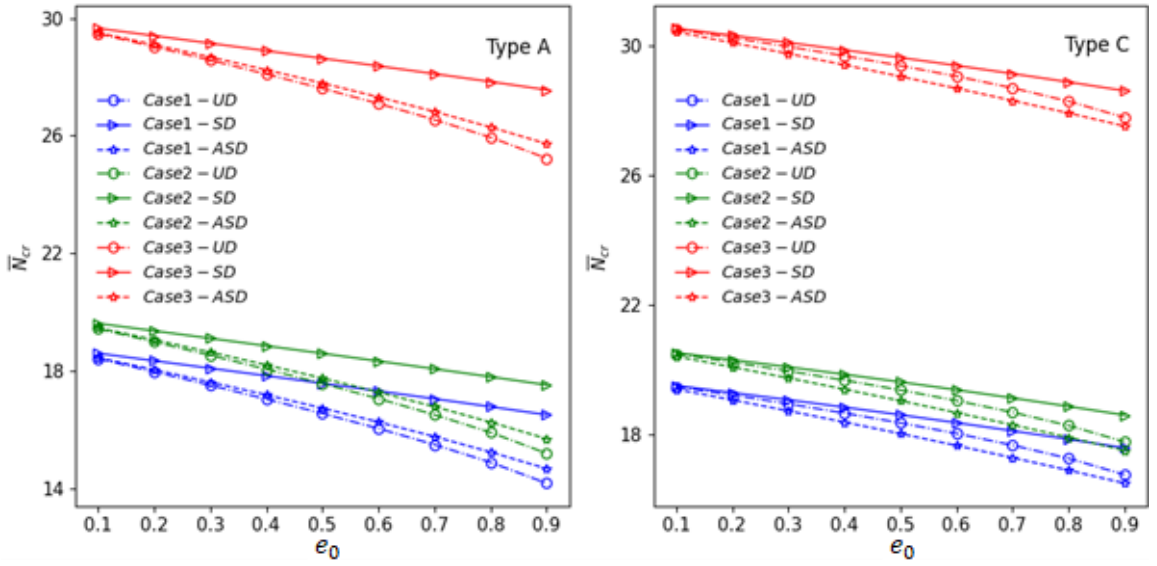

Figure 13. Porosity coefficient effect on critical buckling loads of SS beams under various porosity distributions and elastic foundations (1-2-1, $L/h = 10$, $p = 5$)

3.3.3. The Effect of Skin-Core-Skin Thickness Ratio

Tables 19 and 20 present the influence of the skin-core-skin thickness ratio on fundamental natural frequencies and critical buckling loads for various porosity patterns and porosity coefficients. Both types show increased fundamental natural frequencies with decreasing skin-core-skin thickness ratios. The observed phenomenon is a result of the

reinforcement of the beam's bending stiffness due to the increase in the thickness of the porous core. The critical buckling loads increase as the skin-core-skin thickness ratio decreases for Type A beams, but decrease for Type C beams. The observed behavior can be attributed to the FG nature of the core, which rapidly diminishes bending stiffness as the thickness of the FG porous core grows. Among the ratios considered, the 2-1-2 ratio results in the minimum value, whereas the 1-2-1 ratio corresponds to the maximum value.

3.3.4. The Effect of Power Index and Length-Thickness Ratio

Figures 14 and 15 illustrate the effect of the power index on the critical buckling loads and fundamental frequencies of CC beams with varying porosity distributions. Both fundamental frequencies and critical buckling loads decrease with increasing power index for all porosity patterns. This trend is attributed to the reduction in bending stiffness as the power index increases. The impact of porosity distributions on fundamental natural frequencies and critical buckling loads is less significant in Type A beams compared to Type C beams. This is because the FG face layers in Type A beams contribute more to overall stiffness and dynamic characteristics, minimizing the effect of core porosity. Conversely, in Type C beams, the FG beam with a porous core has a greater influence on overall stiffness than the isotropic face layers.

Figures 16 and 17 illustrate the impact of the length-to-thickness ratio on the fundamental natural frequencies and critical buckling loads of FGSBs with different porosity patterns. Across all porosity distributions, both the fundamental frequencies and critical buckling loads consistently increase as the length-to-thickness ratio increases This trend can be attributed to the enhanced stiffness of the beam as it becomes more slender. Furthermore, the impact of porosity distributions on fundamental frequencies and critical buckling loads becomes more pronounced at higher length-to-thickness ratios. This is attributed to the amplified influence of porosity on beam stiffness and mechanical behavior at larger length-to-thickness ratios.

Table 19. Fundamental natural frequencies variation of the beams with different skin-core-skin thickness ratio, BCs, and porosity distributions (L/h= 5, p = 5, K_w = 25, K_p= 10)

Beam	Scheme	BCs	UD			SD			ASD		
			0.4	0.6	0.8	0.4	0.6	0.8	0.4	0.6	0.8
Type A	2-1-2	SS	4.1583	4.1986	4.2541	4.1626	4.2061	4.2665	4.1595	4.2012	4.2597
		CC	6.9036	6.9241	6.9517	6.9154	6.9483	7.0018	6.9093	6.9388	6.9891
		CF	2.4121	2.4376	2.4725	2.4135	2.4400	2.4766	2.4126	2.4385	2.4745
	1-1-1	SS	4.2530	4.3074	4.3869	4.2712	4.3378	4.4351	4.2571	4.3151	4.4021
		CC	7.1829	7.1939	7.2130	7.2234	7.2669	7.3446	7.1955	7.2247	7.2868
		CF	2.4306	2.4691	2.5241	2.4361	2.4785	2.5393	2.4318	2.4715	2.5290
	1-2-1	SS	4.4506	4.4987	4.5814	4.5056	4.5910	4.7268	4.4611	4.5165	4.6138
		CC	7.6750	7.6272	7.5787	7.7775	7.8076	7.8837	7.6978	7.6819	7.7083
		CF	2.4678	2.5163	2.5900	2.4836	2.5432	2.6332	2.4707	2.5212	2.5991
Type C	2-1-2	SS	4.6028	4.6256	4.6583	4.6047	4.6299	4.6670	4.6015	4.6250	4.6602
		CC	7.8468	7.8574	7.8790	7.8593	7.8819	7.9242	7.8595	7.8824	7.9247
		CF	2.5012	2.5194	2.5434	2.5013	2.5200	2.5449	2.5002	2.5183	2.5424
	1-1-1	SS	4.6360	4.6732	4.7275	4.6395	4.6813	4.7452	4.6278	4.6634	4.7202
		CC	7.7571	7.7616	7.7790	7.7793	7.8075	7.8686	7.7727	7.7982	7.8570
		CF	2.5310	2.5609	2.6015	2.5313	2.5621	2.6049	2.5278	2.5565	2.5970
	1-2-1	SS	4.6783	4.7297	4.8074	4.6876	4.7491	4.8472	4.6573	4.7017	4.7806
		CC	7.6247	7.6014	7.5806	7.6597	7.6776	7.7421	7.6400	7.6514	7.7122
		CF	2.5695	2.6140	2.6767	2.5711	2.6178	2.6856	2.5623	2.6040	2.6659

Table 20. Critical buckling loads variation of the beams with different skin-core-skin thickness ratio, BCs, and porosity distributions (L/h= 5, p = 5, K_w = 25, K_p= 10)

Beam	Scheme	BCs	UD			SD			USD		
			0.4	0.6	0.8	0.4	0.6	0.8	0.4	0.6	0.8
Type A	2-1-2	SS	24.4748	24.3609	24.2174	24.5259	24.4488	24.3627	24.4894	24.3923	24.2850
		CC	55.2446	54.4910	53.3925	55.7971	55.0518	54.1803	55.6979	54.9148	54.0231
		CF	16.9807	16.9454	16.9021	16.9965	16.9720	16.9203	16.9849	16.9541	16.8989
	1-1-1	SS	26.1447	25.7811	25.3378	26.3688	26.1483	25.9048	26.1946	25.8744	25.5206
		CC	60.2137	58.8745	57.6623	62.1894	60.5418	58.7771	61.6997	59.9078	57.8632
		CF	17.4511	17.3936	17.2243	17.5454	17.5042	17.3966	17.4657	17.4196	17.2745
	1-2-1	SS	29.3689	28.3107	27.0639	30.0993	29.4841	28.8135	29.5061	28.5344	27.4517
		CC	73.6865	67.3561	61.5465	74.1833	70.6909	66.7046	72.6439	68.3563	63.5740
		CF	18.4041	18.1501	17.7681	18.6203	18.4995	18.2965	18.4436	18.2122	17.8708
Type C	2-1-2	SS	31.5344	31.3267	31.0817	31.5833	31.4221	31.2567	31.5546	31.3797	31.2012
		CC	75.3690	74.3602	73.1719	75.6514	74.8910	74.1118	75.6765	74.9338	74.1785
		CF	18.9969	18.9556	18.9040	19.0086	18.9787	18.9468	18.9985	18.9637	18.9268
	1-1-1	SS	30.8751	30.4832	30.0093	30.9621	30.6570	30.3378	30.8310	30.4614	30.0787
		CC	71.3038	69.4120	67.1286	71.7751	70.3364	68.8354	71.6676	70.1978	68.6869
		CF	18.8449	18.7556	18.6466	18.8663	18.7988	18.7283	18.8231	18.7336	18.6405
	1-2-1	SS	30.0065	29.2949	28.4109	30.1895	29.6437	29.0563	29.8377	29.1160	28.3558
		CC	66.0796	62.8341	58.7904	66.7852	64.2527	61.5345	66.4272	63.7972	61.0618
		CF	18.6410	18.4638	18.2223	18.6929	18.5614	18.4284	18.5751	18.3812	18.1819

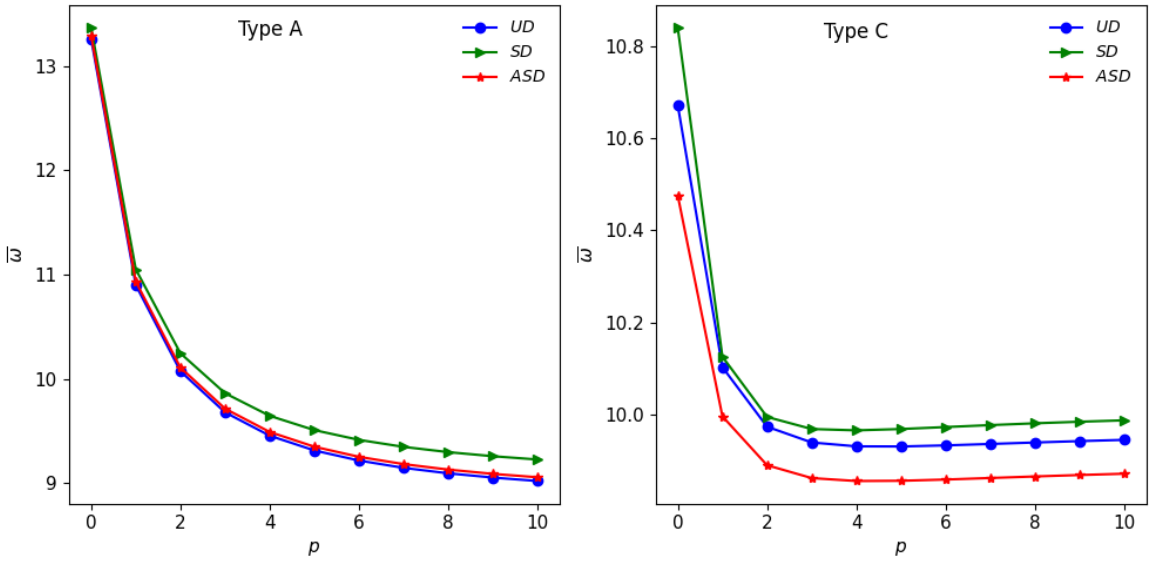

Figure 14. Effect of power index on fundamental natural frequencies in CC beams across different porosity distributions (1-2-1, $L/h = 15$, $e_0 = 0.5$, $K_w = 50$, $K_p = 10$)

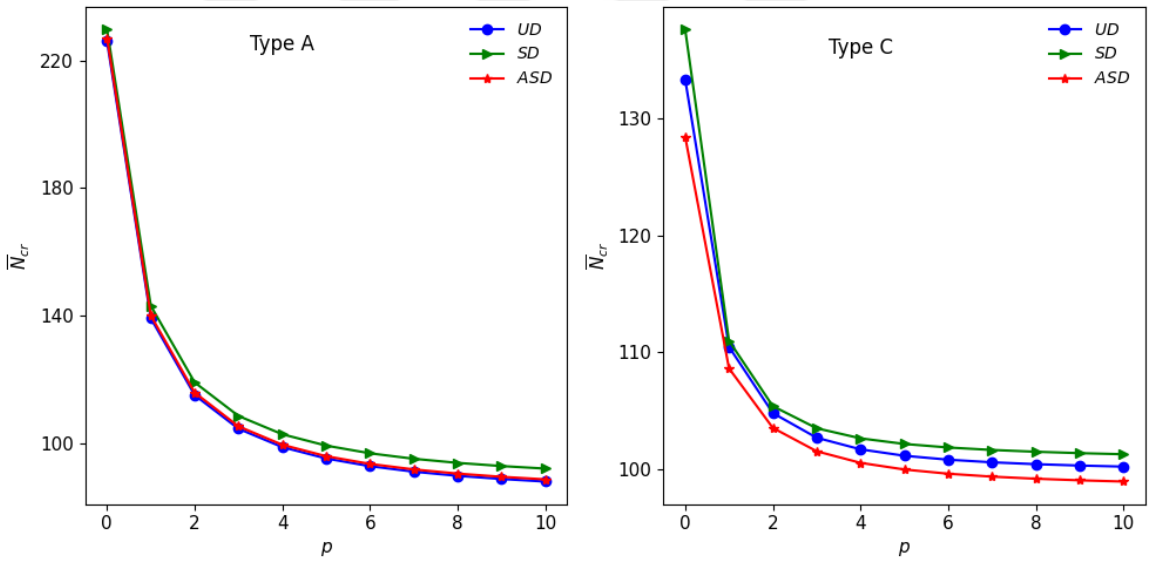

Figure 15. Effect of power index on critical buckling loads in CC beams across different porosity distributions (1-2-1, $L/h = 15$, $e_0 = 0.5$, $K_w = 50$, $K_p = 10$)

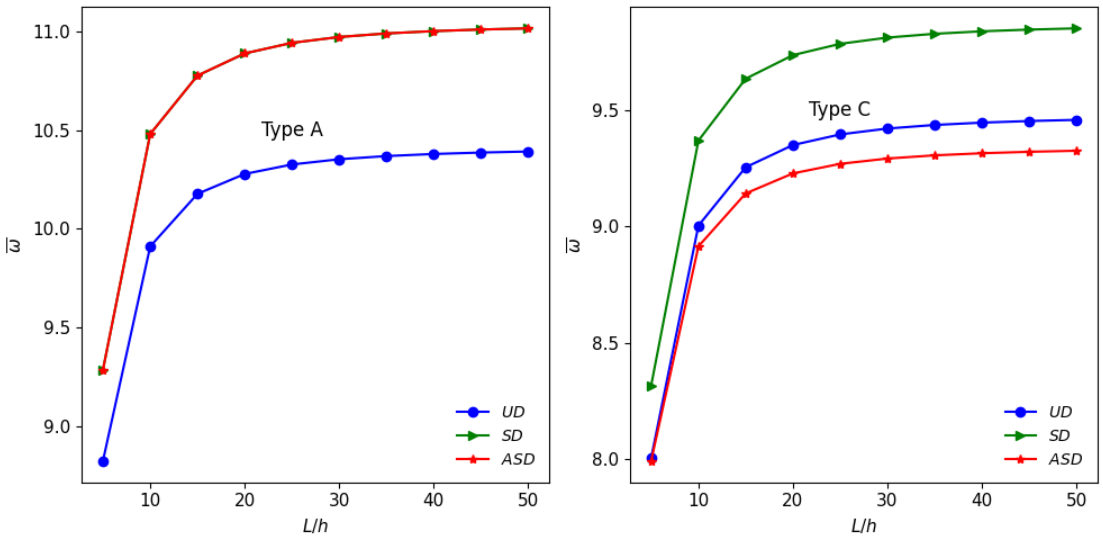

Figure 16. Effect of length-to-thickness ratio on fundamental natural frequencies in CC beams across various porosity distributions (1-2-1, $e_0 = 0.5$, $K_w = K_p = 10$,$p = 1$)

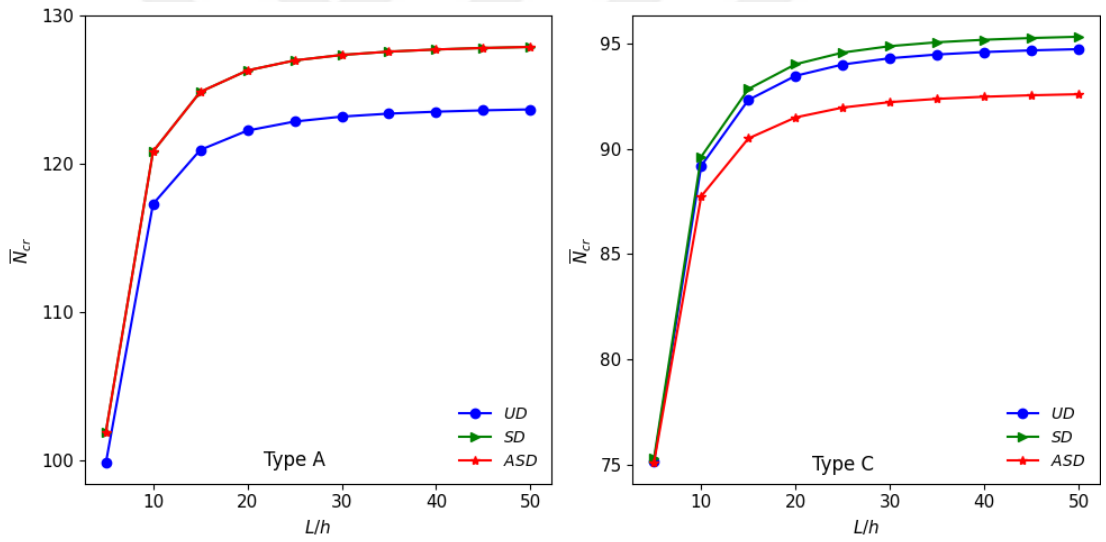

Figure 17. Effect of length-to-thickness ratio on critical buckling loads in CC beams across various porosity distributions (1-2-1, $e_0 = 0.5$, $K_w = K_p = 10$, $p = 1$)

3.3.5. Elastic Foundation Effect

The effects of different foundation parameters on fundamental natural frequencies and critical buckling loads are summarized in Tables 21 and 22. As expected, fundamental frequencies and critical buckling loads increase with increasing foundation constants, regardless of porosity distributions or boundary conditions. In addition, the variations of critical buckling loads and nondimensional fundamental frequencies as functions of elastic foundation parameters are given in Figures 18 and 19. Remarkably, a substantial

improvement in both fundamental frequencies and critical buckling loads is achieved by increasing the Pasternak parameter. This implies that variations in K_p affect the mechanical behavior of the beam more significantly than variations in the Winkler parameter (K_w). Besides, porosity distributions have a negligible effect, especially for the CF beam. This is mainly because the elastic foundation effect on bending stiffness has a more significant influence than that of the porosity. Among the considered porosity distributions, symmetric distribution yields slightly higher values than the others.

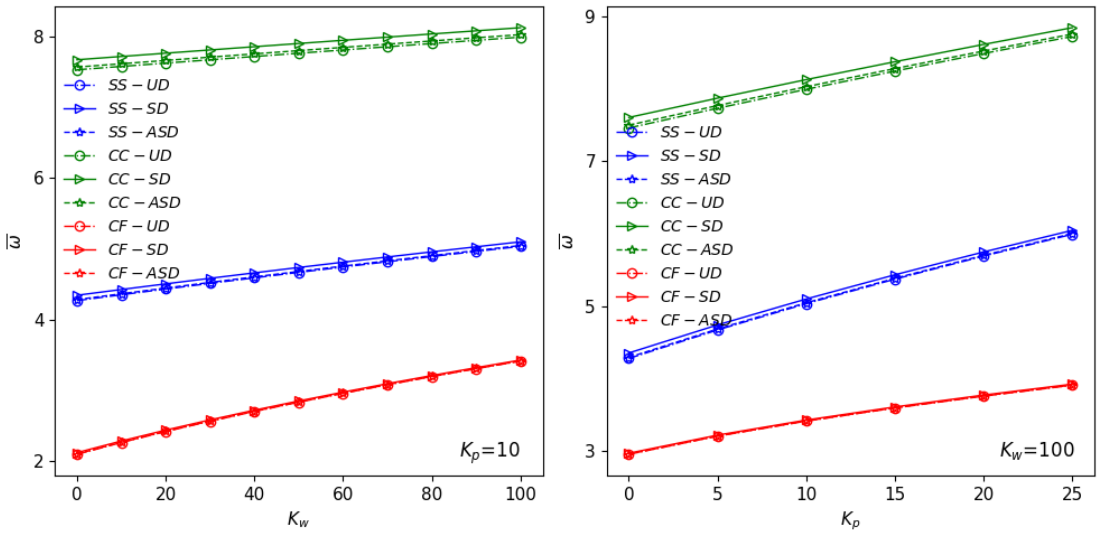

Figure 18. Effect of Winkler and Pasternak foundation on fundamental frequencies of Type A beam with different BCs and porosity distributions (1-2-1, e_0 = 0.5, L/h = 5, p =5)

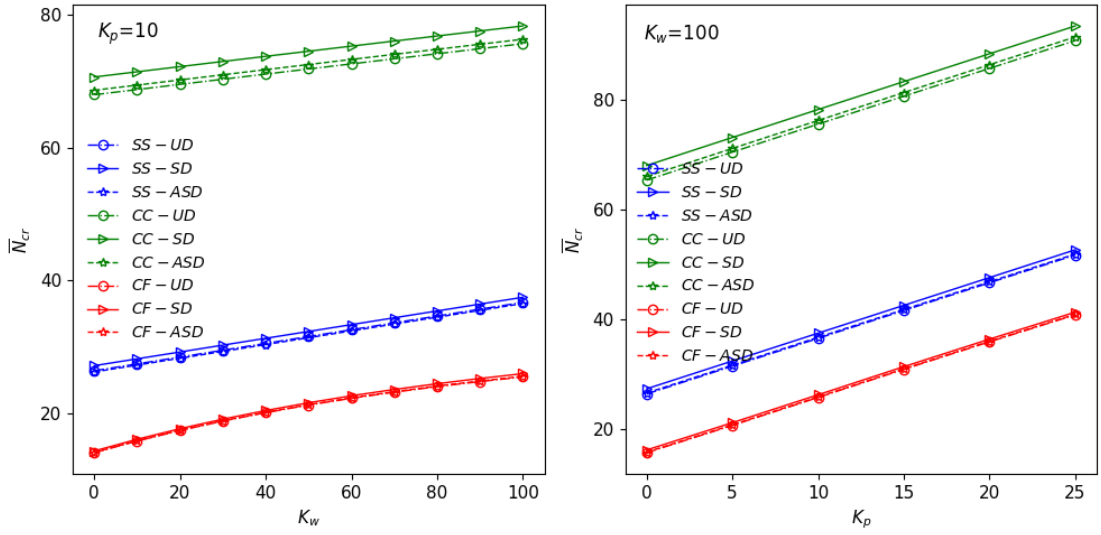

Figure 19. Effect of Winkler and Pasternak foundation on critical buckling loads of Type A beam with different BCs and porosity distributions (1-2-1, e_0 = 0.5, L/h = 5, p =5)

Table 21. Effect of foundation parameters on fundamental frequencies of FGSBs (1-2-1, L/h = 5, p = 5, e_0 = 0.5)

Beam	K_p	BCs	UD			SD			USD		
			K_w								
			0	50	100	0	50	100	0	50	100
Type A	0	SS	3.3417	3.8388	4.2786	3.4381	3.9230	4.3542	3.3602	3.8549	4.2930
		CC	6.9635	7.2168	7.4602	7.1183	7.3658	7.6052	7.0047	7.2559	7.4986
		CF	1.1867	2.2035	2.8814	1.2546	2.2806	2.9711	1.2236	2.2638	2.9583
	10	SS	4.2677	4.6672	5.0351	4.3435	4.7366	5.0995	4.2821	4.6803	5.0472
		CC	7.5317	7.7660	7.9934	7.6735	7.9042	8.1271	7.5699	7.8030	8.0293
		CF	2.0384	2.7591	3.3271	2.1160	2.8488	3.4283	2.0957	2.8338	3.4160
	25	SS	5.3649	5.6878	5.9933	5.4253	5.7448	6.0475	5.3762	5.6985	6.0035
		CC	8.3012	8.5145	8.7225	8.4283	8.6379	8.8437	8.3361	8.5484	8.7556
		CF	2.7527	3.3227	3.8083	2.8474	3.4281	3.9238	2.8287	3.4126	3.9103
Type C	0	SS	3.5605	4.0608	4.5058	3.5821	4.0784	4.5205	3.5336	4.0350	4.4805
		CC	6.8851	7.1602	7.4250	6.9443	7.2163	7.4784	6.9183	7.1905	7.4528
		CF	1.3179	2.3686	3.0782	1.3253	2.3705	3.0780	1.3042	2.3572	3.0674
	10	SS	4.4947	4.9004	5.2748	4.5095	4.9128	5.2854	4.4695	4.8754	5.2500
		CC	7.4851	7.7390	7.9847	7.5387	7.7900	8.0335	7.5154	7.7668	8.0103
		CF	2.1848	2.9433	3.5422	2.1889	2.9445	3.5417	2.1751	2.9334	3.5302
	25	SS	5.6111	5.9408	6.2531	5.6201	5.9484	6.2595	5.5862	5.9158	6.2279
		CC	8.2932	8.5230	8.7469	8.3404	8.5683	8.7904	8.3200	8.5479	8.7698
		CF	2.9209	3.5325	4.0448	2.9243	3.5337	4.0446	2.9200	3.5181	4.0358

Table 22. Effect of foundation parameters on critical buckling loads of FGSBs (1-2-1, $L/h = 5$, $p = 5$, $e_0 = 0.5$)

Beam	K_p	BCs	UD			SD			USD		
			K_w								
			0	50	100	0	50	100	0	50	100
Type A	0	SS	16.1248	21.2729	26.4178	17.0672	22.2150	27.3597	16.3028	21.4503	26.5946
		CC	57.6874	61.5642	65.3416	60.3610	63.8891	68.0065	58.3579	62.2370	66.0558
		CF	4.1354	11.3918	15.7797	4.3916	11.7321	16.2699	4.1805	11.4563	15.8779
	10	SS	26.2837	31.4255	36.5642	27.2256	32.3674	37.5063	26.4605	31.6018	36.7400
		CC	67.9403	71.4621	75.4959	70.6091	73.9677	35.8064	68.6048	72.4783	76.2761
		CF	14.1812	21.4509	25.9195	14.4374	21.7884	26.4032	14.2259	21.5142	26.0155
	25	SS	41.4988	46.6313	51.7606	42.4413	47.5744	52.7044	41.6742	46.8063	51.9353
		CC	83.2007	86.7895	90.6369	85.8922	89.6961	92.7720	83.9102	87.7467	91.5154
		CF	29.2443	36.3793	40.7582	29.5009	36.7289	41.2519	29.2886	36.4465	40.8562
Type C	0	SS	17.0137	22.1291	27.2427	17.2698	22.3851	27.4986	16.8328	21.9469	27.0592
		CC	52.4693	56.2758	59.9712	53.4837	57.2917	60.9925	53.0677	56.8758	60.5862
		CF	4.5749	11.6358	15.7785	4.6369	11.7290	15.9229	4.4931	11.5703	15.7247
	10	SS	27.1094	32.2212	37.3312	27.3653	32.4770	37.5870	26.9259	32.0365	37.1453
		CC	62.6126	66.4114	70.0998	63.6272	67.4281	71.1202	63.2108	67.0138	70.7123
		CF	14.5430	21.6138	25.7249	14.6050	21.7118	25.8696	14.4622	21.5311	25.6850
	25	SS	42.2396	47.3460	52.4506	42.4954	47.6018	52.7065	42.0525	47.1578	52.2613
		CC	77.7781	81.5636	85.2327	78.7934	82.5805	86.2578	78.3771	82.1661	85.8501
		CF	29.4919	36.5531	40.6100	29.5542	36.6484	40.7560	29.4127	36.4314	40.5452

3.4. Free Vibration and Buckling Analysis of FGSBs with Porous Core Resting on Elastic Foundation by Finite Element Method

3.4.1. Convergence and Validation Study

To validate the proposed FE model, free vibration and buckling analysis are conducted on non-porous FGSBs with 1-2-1 configuration. Type B and Type C beams are examined. The convergence behavior of the developed FE model is summarized in Tables 23 and 24. The FE model demonstrated a high level of accuracy in its results, exhibiting strong agreement with findings from prior research and the Ritz solution. The convergence study indicated that four elements are sufficient to achieve convergence for SS beams across both beam types. Conversely, 20 elements are required to obtain consistent results for CC and CF beam configurations. A discretization of 24 beam elements is then adopted for all subsequent analyses to preserve computational accuracy. Furthermore, Tables 25-28 compare fundamental natural frequencies and critical buckling loads for FGSBs. The proposed FE model exhibited an exceptional level of concordance with the results obtained using two different HSDTs (Nguyen et al., 2015; Vo et al., 2014), quasi-3D theory (Nguyen et al., 2016), and the Ritz method. For the sake of thoroughness, the first three natural frequencies of the beams are presented in Tables 29 and 30.

Table 23. Convergence study of fundamental natural frequencies of the beams (p = 5)

Beam	Number of elements	$L/h = 5$			$L/h = 20$		
		SS	CC	CF	SS	CC	CF
Type B	4	2.6819	5.3848	0.9942	2.8375	6.4359	2.4778
	8	2.6819	5.3232	0.9915	2.8375	6.3986	2.4716
	12	2.6819	5.3038	0.9907	2.8375	6.3870	2.4697
	16	2.6819	5.2954	0.9903	2.8375	6.3814	2.4688
	20	2.6819	5.2914	0.9901	2.8375	6.3781	2.4683
	24	2.6819	5.2894	0.9900	2.8375	6.3759	2.4680
	28	2.6819	5.2883	0.9900	2.8375	6.3744	2.4677
	32	2.6819	5.2877	0.9899	2.8375	6.3733	2.4676
	Ritz solution	2.6819	5.2929	0.9901	2.8375	6.3901	1.0147
	HSDT[1]	2.6773	5.2311	0.9847	2.8371	6.3509	1.0130
Type C	4	4.0997	8.5814	1.5059	4.2714	9.7152	1.5316
	8	4.0996	8.5015	1.5025	4.2713	9.6665	1.5283
	12	4.0996	8.4749	1.5013	4.2713	9.6519	1.5272
	16	4.0996	8.4626	1.5007	4.2713	9.6447	1.5267
	20	4.0996	8.4566	1.5004	4.2713	9.6404	1.5265
	24	4.0996	8.4535	1.5002	4.2713	9.6376	1.5263
	28	4.0996	8.4519	1.5002	4.2713	9.6356	1.5262
	32	4.0996	8.4510	1.5001	4.2713	9.6341	1.5261
	Ritz solution	4.0996	8.4521	1.4967	4.2713	9.6537	1.5247
	HSDT[2]	4.0691	8.3282	1.4840	4.2445	9.5451	1.5145
	Quasi-3D[1]	4.0996	8.4529	1.5001	4.2711	9.6404	1.5264

HSDT[2] (Nguyen et al., 2015); Quasi-3D[1] (Nguyen et al., 2016)

Table 24. Convergence study of critical buckling loads of the beams (p = 5)

Beam	Number of elements	$L/h = 5$			$L/h = 20$		
		SS	CC	CF	SS	CC	CF
Type B	4	9.1351	29.5573	2.4298	9.8211	39.1240	2.4778
	8	9.1351	29.5358	2.4211	9.8211	38.9236	2.4716
	12	9.1351	29.5296	2.4177	9.8211	38.8679	2.4697
	16	9.1351	29.5264	2.4164	9.8211	38.8422	2.4688
	20	9.1351	29.5246	2.4158	9.8211	38.8277	2.4683
	24	9.1351	29.5237	2.4156	9.8211	38.8186	2.4680
	28	9.1351	29.5233	2.4154	9.8211	38.8124	2.4677
	32	9.1351	29.5230	2.4153	9.8211	38.8081	2.4676
	Ritz solution	9.1351	29.5271	2.4157	9.8211	38.9343	2.4681
	HSDT[1]	8.9519	28.0272	2.4057	9.8067	38.4910	2.4635
Type C	4	28.7899	100.7534	7.4741	30.0196	120.3349	7.5569
	8	28.7882	100.6137	7.4503	30.0195	119.6885	7.5406
	12	28.7881	100.5869	7.4410	30.0195	119.5359	7.5356
	16	28.7881	100.5730	7.4375	30.0195	119.4671	7.5333
	20	28.7881	100.5653	7.4359	30.0195	119.4281	7.5319
	24	28.7881	100.5614	7.4351	30.0195	119.4032	7.5311
	28	28.7881	100.5594	7.4346	30.0195	119.3860	7.5304
	32	28.7881	100.5583	7.4343	30.0195	119.3736	7.5300
	Ritz solution	28.7881	100.5588	7.4236	30.0195	119.6879	7.5279
	HSDT[2]	27.9314	94.6117	7.3149	29.6120	117.0384	7.4254
	Quasi-3D[1]	28.7884	100.5883	7.4344	30.0168	119.4172	7.5312

Table 25. Fundamental natural frequencies of Type B beams

L/h	BC	Theory	p					
			0	0.5	1	2	5	10
5	SS	FEM	2.6819	3.9979	4.3730	4.6536	4.8650	4.9416
		Ritz method	2.6819	3.9979	4.3730	4.6536	4.8650	4.9416
		HSDT[1]	2.6773	4.0504	4.4270	4.7047	4.9038	4.9700
	CC	FEM	5.2894	7.1181	7.5838	7.9629	8.3204	8.4894
		Ritz method	5.2929	7.1243	7.5909	7.9706	8.3285	8.4976
		HSDT[1]	5.2311	7.2456	7.8056	8.2835	8.7255	8.9195
	CF	FEM	0.9900	1.5095	1.6620	1.7747	1.8556	1.8825
		Ritz method	0.9901	1.5095	1.6620	1.7748	1.8556	1.8826
		HSDT[1]	0.9847	1.5211	1.6691	1.7745	1.8444	1.8652
20	SS	FEM	2.8375	4.4165	4.8944	5.2452	5.4851	5.5583
		Ritz method	2.8375	4.4165	4.8944	5.2452	5.4851	5.5583
		HSDT[1]	2.8371	4.4160	4.8938	5.2445	5.4843	5.5575
	CC	FEM	6.3759	9.7936	10.8088	11.5576	12.0853	12.2560
		Ritz method	6.3901	9.8189	10.8371	11.5881	12.1170	12.2880
		HSDT[1]	6.3509	9.7587	10.7706	11.5168	12.0423	12.2122
	CF	FEM	1.0146	1.5818	1.7540	1.8803	1.9663	1.9924
		Ritz method	1.0147	1.5819	1.7541	1.8804	1.9664	1.9925
		HSDT[1]	1.0130	1.5796	1.7516	1.8778	1.9636	1.9896

HSDT[1] (Vo et al., 2014); HSDT[2] (Nguyen et al., 2015); Quasi-3D[1] (Nguyen et al., 2016)

Table 26. Fundamental natural frequencies of Type C beams

L/h	BC	Theory	p					
			0	0.5	1	2	5	10
5	SS	FEM	4.0996	3.8439	3.7165	3.6112	3.5512	3.5417
		Ritz method	4.0996	3.8439	3.7165	3.6112	3.5512	3.5417
		HSDT[2]	4.0691	3.7976	3.6636	3.553	3.4914	3.483
		Quasi-3D[1]	4.0996	3.8438	3.7172	3.6119	3.5513	3.5413
	CC	FEM	8.4535	7.8938	7.5898	7.2904	7.0069	6.8815
		Ritz method	8.4525	7.8932	7.5894	7.2903	7.0071	6.8818
		HSDT[2]	8.3282	7.7553	7.4487	7.1485	6.8702	6.7543
		Quasi-3D[1]	8.4529	7.8924	7.5904	7.2898	7.0032	6.8757
	CF	FEM	1.5002	1.4078	1.3626	1.3271	1.3112	1.3119
		Ritz method	1.5003	1.4078	1.3626	1.3271	1.3112	1.3119
		HSDT[2]	1.4840	1.3865	1.3393	1.3022	1.2857	1.2867
		Quasi-3D[1]	1.5001	1.4076	1.3627	1.3273	1.3113	1.3118
20	SS	FEM	4.2713	4.0146	3.8916	3.7995	3.7702	3.7826
		Ritz method	4.2713	4.0146	3.8916	3.7995	3.7702	3.7826
		HSDT[2]	4.2445	3.9695	3.8387	3.7402	3.7081	3.7214
		Quasi-3D[1]	4.2711	4.0143	3.8923	3.8003	3.7708	3.7831
	CC	FEM	9.6376	9.0508	8.7668	8.5477	8.4604	8.4738
		Ritz method	9.6546	9.0658	8.7809	8.5613	8.4741	8.488
		HSDT[2]	9.5451	8.9243	8.6264	8.3959	8.3047	8.3205
		Quasi-3D[1]	9.6404	9.0524	8.7701	8.5509	8.4627	8.4755
	CF	FEM	1.5263	1.4344	1.3904	1.3576	1.3475	1.3523
		Ritz method	1.5264	1.4344	1.3905	1.3577	1.3476	1.3523
		HSDT[2]	1.5145	1.4165	1.37	1.335	1.3241	1.3292
		Quasi-3D[1]	1.5264	1.4344	1.3907	1.358	1.3478	1.3525

HSDT[2] (Nguyen et al., 2015); Quasi-3D[1] (Nguyen et al., 2016)

Table 27. Critical buckling loads of Type B beams

L/h	BC	Theory	p					
			0	0.5	1	2	5	10
5	SS	FEM	9.1351	21.7614	26.9366	31.5445	35.6386	37.3250
		Ritz method	9.1351	21.7614	26.9366	31.5445	35.6386	37.3250
		HSDT[1]	9.8067	25.6086	32.5803	38.7192	43.7637	45.6040
	CC	FEM	29.5237	58.3337	68.8601	78.7220	88.8611	93.8148
		Ritz method	29.5271	58.3461	68.8748	78.7385	88.8791	93.8336
		HSDT[1]	28.0272	56.1398	66.4523	76.0626	85.8462	90.5815
	CF	FEM	2.4156	6.1749	7.8042	9.2408	10.4430	10.8956
		Ritz method	2.4157	6.1752	7.8047	9.2413	10.4436	10.8962
		HSDT[1]	2.4057	6.1578	7.7858	9.2209	10.4208	10.8716
20	SS	FEM	9.8211	25.6411	32.6255	38.7731	43.8252	45.6685
		Ritz method	9.8211	25.6411	32.6255	38.7731	43.8252	45.6685
		HSDT[1]	9.8067	25.6086	32.5803	38.7192	43.7637	45.6040
	CC	FEM	38.8186	99.2672	125.4954	148.6238	167.9729	175.2486
		Ritz method	38.9343	99.6031	125.9248	149.1336	168.5475	175.8463
		HSDT[1]	38.4910	98.5240	24.5720	47.5350	66.7330	73.9460
	CF	FEM	2.4680	6.4753	8.2526	9.8164	11.0958	11.5589
		Ritz method	2.4681	6.4757	8.2531	9.8170	11.0965	11.5596
		HSDT[1]	2.4635	6.4654	8.2402	9.8018	11.0792	6.4654

HSDT[1] (Vo et al., 2014)

Table 28. Critical buckling loads of Type C beams

L/h	BC	Theory	p					
			0	0.5	1	2	5	10
5	SS	FEM	28.7881	23.8572	21.6294	19.7893	18.5216	18.1383
		Ritz method	28.7881	23.8572	21.6294	19.7893	18.5216	18.1383
		HSDT[2]	27.9314	22.9869	20.7762	18.9588	17.732	17.3775
		Quasi-3D[1]	28.7884	23.8554	21.6374	19.7957	18.5212	18.1329
	CC	FEM	100.5614	82.4740	73.9071	66.1303	59.3190	56.4930
		Ritz method	100.5629	82.477	73.9112	66.1354	59.3243	56.4987
		HSDT[2]	94.6117	77.5129	69.4877	62.2249	55.9446	53.3734
		Quasi-3D[1]	100.5883	82.4783	73.9348	66.1308	59.2628	56.4049
	CF	FEM	7.4351	6.1847	5.6286	5.1864	4.9216	4.8653
		Ritz method	7.4354	6.1849	5.6288	5.1866	4.9218	4.8655
		HSDT[2]	7.3149	6.0286	5.4629	5.0154	4.7534	4.7024
		Quasi-3D[1]	7.4344	6.1836	5.6304	5.1884	4.9228	4.8658
20	SS	FEM	30.0195	24.9952	22.772	21.0254	20.0317	19.8573
		Ritz method	30.0195	24.9952	22.772	21.0254	20.0317	19.8573
		HSDT[2]	29.612	24.414	22.1386	20.3581	19.3639	19.2058
		Quasi-3D[1]	30.0168	24.9914	22.7796	21.0343	20.0386	19.8622
	CC	FEM	119.4032	99.2755	90.3305	83.2242	78.9796	78.0853
		Ritz method	119.7827	99.5671	90.5848	83.4516	79.1967	78.3045
		HSDT[2]	117.0384	96.4573	87.4069	80.2465	76.0539	75.2379
		Quasi-3D[1]	119.4172	99.2742	90.3696	83.2627	79.0045	78.0989
	CF	FEM	7.5311	6.2708	5.7138	5.2775	5.0325	4.9920
		Ritz method	7.5315	6.2711	5.7140	5.2778	5.0327	4.9922
		HSDT[2]	7.4254	6.1225	5.5529	5.1084	4.8634	4.8269
		Quasi-3D[1]	7.5312	6.2702	5.716	5.28	5.0345	4.9934

HSDT[2] (Nguyen et al., 2015); Quasi-3D[1] (Nguyen et al., 2016)

Table 29. Comparison of first three natural frequencies in Type B beams (L/h = 5)

Mode	BC	Theory	p					
			0	0.5	1	2	5	10
1	SS	FEM	2.6819	3.9979	4.3730	4.6536	4.8650	4.9416
		Ritz method	2.6819	3.9979	4.3730	4.6536	4.8650	4.9416
		HSDT[1]	2.6773	4.0504	4.4270	4.7047	4.9038	4.9700
	CC	FEM	5.2894	7.1181	7.5838	7.9629	8.3204	8.4894
		Ritz method	5.2929	7.1243	7.5909	7.9706	8.3285	8.4976
		HSDT[1]	5.2311	7.2456	7.8056	8.2835	8.7255	8.9195
	CF	FEM	0.9900	1.5095	1.6620	1.7747	1.8556	1.8825
		Ritz method	0.9901	1.5095	1.6620	1.7748	1.8556	1.8826
		HSDT[1]	0.9847	1.5211	1.6691	1.7745	1.8444	1.8652
2	SS	FEM	9.3379	12.8786	13.7986	14.5280	15.1801	15.4727
		Ritz method	9.3379	12.8786	13.7986	14.5280	15.1801	15.4727
		HSDT[1]	9.2909	12.8310	13.7464	14.4701	15.1156	15.4047
	CC	FEM	12.1812	15.4688	16.2925	17.0136	17.7724	18.1649
		Ritz method	12.5970	16.5814	17.6667	18.6710	19.0927	19.5200
		HSDT[1]	12.5225	16.0881	16.9638	17.7202	18.5077	18.9119
	CF	FEM	5.3586	7.4934	8.0584	8.5002	8.8818	9.0470
		Ritz method	5.3591	7.4940	8.0590	8.5009	8.8826	9.0477
		HSDT[1]	5.3234	7.4544	8.0182	8.4585	8.8373	9.0006
3	SS	FEM	17.9179	23.2515	24.5620	25.6794	26.8221	27.4001
		Ritz method	17.9178	23.2514	24.5619	25.6792	26.8219	27.3999
		HSDT[1]	17.7751	23.1294	24.4327	25.5391	26.6663	27.2351
	CC	FEM	16.4664	20.9126	22.6223	24.1082	25.4190	25.9665
		Ritz method	16.4673	20.9137	22.6235	24.1094	25.4203	25.9678
		HSDT[1]	15.7120	19.9545	21.5859	23.0036	24.2544	24.7768
	CF	FEM	8.2332	10.4563	11.3112	12.0541	12.7095	12.9832
		Ritz method	8.2332	10.4563	11.3112	12.0541	12.7095	12.9832
		HSDT[1]	7.8545	9.9753	10.7909	11.4996	12.1248	12.3860

HSDT[1] (Vo et al., 2014)

Table 30. Comparison of first three natural frequencies in Type C beams (L/h = 5)

Mode	BC	Theory	p					
			0	0.5	1	2	5	10
1	SS	FEM	4.0996	3.8439	3.7165	3.6112	3.5512	3.5417
		Ritz method	4.0996	3.8439	3.7165	3.6112	3.5512	3.5417
		HSDT[2]	4.0691	3.7976	3.6636	3.5530	3.4914	3.4830
	CC	FEM	8.4535	7.8938	7.5898	7.2904	7.0069	6.8815
		Ritz method	8.4525	7.8932	7.5894	7.2903	7.0071	6.8818
		HSDT[2]	8.3282	7.7553	7.4487	7.1485	6.8702	6.7543
	CF	FEM	1.5002	1.4078	1.3626	1.3271	1.3112	1.3119
		Ritz method	1.5003	1.4078	1.3626	1.3271	1.3112	1.3119
		HSDT[2]	1.4840	1.3865	1.3393	1.3022	1.2857	1.2867
2	SS	FEM	14.7402	13.7534	13.2273	12.7289	12.2980	12.1255
		Ritz method	14.7403	13.7536	13.2275	12.7291	12.2982	12.1257
		HSDT[2]	14.5921	13.5629	13.0215	12.5117	12.0822	11.9168
	CC	FEM	20.1544	18.7387	17.9222	17.0450	16.0975	15.6427
		Ritz method	20.7864	19.3438	18.5249	17.6623	16.7505	16.3147
		HSDT[2]	19.8886	18.4463	17.6290	16.7552	15.8266	15.3878
	CF	FEM	8.4115	7.8472	7.5479	7.2682	7.0355	6.9473
		Ritz method	8.4122	7.8478	7.5484	7.2686	7.0359	6.9477
		HSDT[2]	8.3149	7.7255	7.4173	7.1308	6.8984	6.8139
3	SS	FEM	29.1374	27.0784	25.9265	24.7440	23.4231	22.7558
		Ritz method	29.1329	27.0748	25.9235	24.7414	23.4232	22.7559
		HSDT[2]	28.7653	26.6542	25.4901	24.3022	23.1254	22.5934
	CC	FEM	34.4183	31.9232	30.4419	28.7950	26.9517	26.0580
		Ritz method	34.5185	32.0116	30.5248	28.8733	27.0258	26.1303
		HSDT[2]	34.0624	31.5260	30.0458	28.4068	26.5927	25.7241
	CF	FEM	14.6578	13.6956	13.1485	12.5521	11.8995	11.5818
		Ritz method	14.6579	13.6956	13.1486	12.5521	11.8995	11.5818
		HSDT[2]	14.0712	13.2130	12.7196	12.1683	11.5477	11.2377

HSDT[2] (Nguyen et al., 2015)

3.4.2. Porosity Effect

The fundamental natural frequencies and critical buckling loads of 1-2-1 configuration FGSBs are provided in Tables 31-34, considering various porosity patterns with different coefficients (e_0= 0.4, 0.6, 0.8) the context of three distinct foundation models: without foundation, Winkler, and Pasternak. FEM results exhibit a trend that correlates strongly with the Ritz solution results. This alignment implies that the porosity coefficient and elastic foundation modulus have comparable impacts on the response of

FGSBs with porous cores, regardless of core material constituents. Figures 20 and 21 graphically illustrate the influence of the porosity coefficient on natural frequencies and critical buckling loads of simply supported FGSBs for three different foundation conditions: Case 1 (K_w = 0 and K_p = 0), Case 2 (K_w = 10 and K_p = 0), and Case 3 (K_w = 10 and K_p = 10), considering SD pattern.

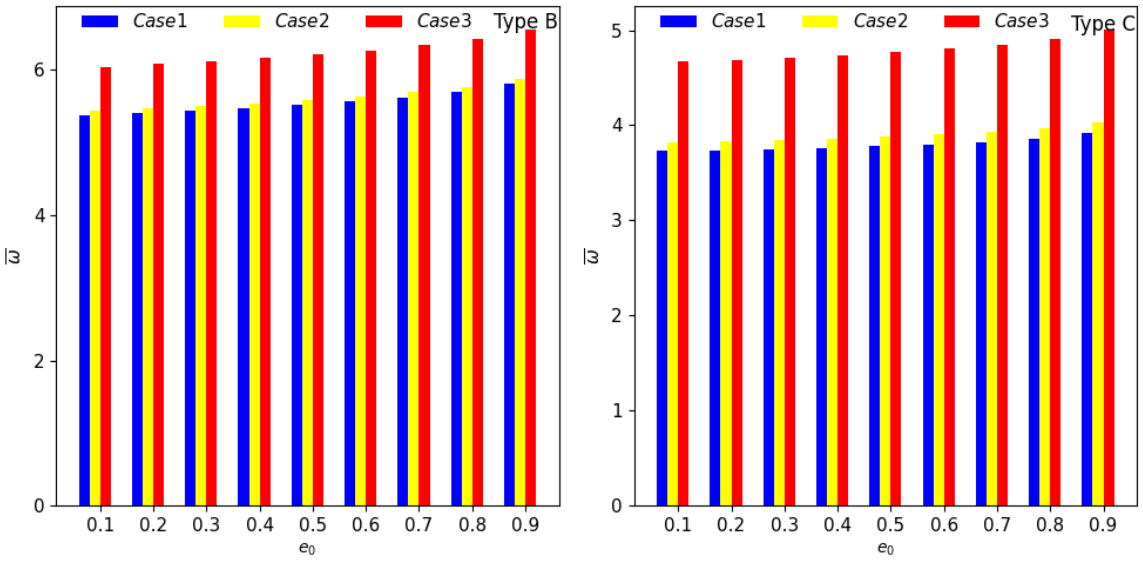

Figure 20. Porosity coefficient influence on fundamental frequencies of SS beams under various porosity distributions and elastic foundations (1-2-1, L/h = 10, p = 5)

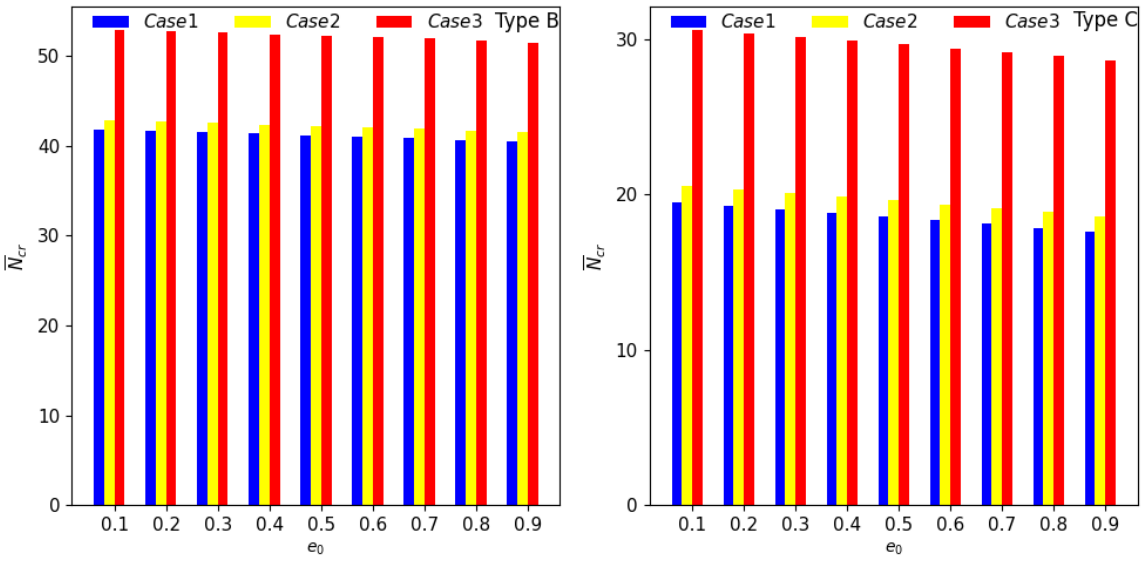

Figure 21. Porosity coefficient influence on critical buckling loads of SS beams under various porosity distributions and elastic foundations (1-2-1, L/h = 10, p = 5)

Table 31. Fundamental natural frequencies variation in the Type B beam with different BCs, porosity distributions, and elastic foundation (1-2-1, p = 2)

L/h	K_w	K_p	BCs	e_0								
				UD			SD			ASD		
				0.4	0.6	0.8	0.4	0.6	0.8	0.4	0.6	0.8
5	0	0	SS	4.7059	4.7404	4.7894	4.7090	4.7507	4.8199	4.7102	4.7541	4.8272
			CC	7.8424	7.7661	7.6740	7.8350	7.7761	7.7466	7.8554	7.8114	7.8015
			CF	1.8082	1.8310	1.8632	1.8105	1.8358	1.8736	1.8095	1.8347	1.8727
	100	0	SS	5.4475	5.5077	5.5929	5.4503	5.5165	5.6188	5.4512	5.5193	5.6249
			CC	8.3153	8.2639	8.2071	8.3083	8.2733	8.2750	8.3275	8.3064	8.3263
			CF	3.2941	3.3561	3.4434	3.2953	3.3586	3.4487	3.2948	3.3580	3.4482
	100	10	SS	6.0915	6.1720	6.2860	6.0940	6.1799	6.3088	6.0948	6.1823	6.3141
			CC	8.7913	8.7618	8.7362	8.7847	8.7709	8.8006	8.8029	8.8021	8.8488
			CF	3.7149	3.7825	3.8776	3.7156	3.7846	3.8833	3.7157	3.7849	3.8843
20	0	0	SS	5.3859	5.4838	5.6234	5.3957	5.5004	5.6503	5.3888	5.4897	5.6358
			CC	11.8095	11.9823	12.2269	11.8267	12.0153	12.2924	11.8174	12.0025	12.2775
			CF	1.9321	1.9682	2.0198	1.9357	1.9742	2.0292	1.9331	1.9701	2.0236
	100	0	SS	6.0566	6.1709	6.3335	6.0653	6.1856	6.3573	6.0591	6.1762	6.3444
			CC	12.1301	12.3119	12.5693	12.1468	12.3441	12.6329	12.1377	12.3315	12.6185
			CF	3.3787	3.4483	3.5467	3.3808	3.4517	3.5521	3.3793	3.4494	3.5489
	100	10	SS	6.6526	6.7812	6.9636	6.6605	6.7946	6.9853	6.6549	6.7860	6.9736
			CC	12.5032	12.6945	12.9651	12.5194	12.7257	13.0270	12.5107	12.7138	13.0134
			CF	3.8409	3.9203	4.0323	3.8428	3.9234	4.0374	3.8415	3.9214	4.0346

Table 32. Fundamental natural frequencies variation in the Type C beam with different BCs, porosity distributions, and elastic foundation (1-2-1, p = 2)

L/h	K_w	K_p	BCs	e_0								
				UD			SD			ASD		
				0.4	0.6	0.8	0.4	0.6	0.8	0.4	0.6	0.8
5	0	0	SS	3.6131	3.6166	3.6252	3.6202	3.6343	3.6699	3.5868	3.5827	3.5982
			CC	7.1820	7.1076	7.0061	7.1953	7.1516	7.1346	7.1899	7.1531	7.1535
			CF	1.3321	1.3366	1.3447	1.3348	1.3429	1.3598	1.3201	1.3197	1.3267
	100	0	SS	4.5056	4.5472	4.6100	4.5102	4.5594	4.6422	4.4810	4.5140	4.5784
			CC	7.6746	7.6291	7.5701	7.6865	7.6690	7.6872	7.6795	7.6670	7.6990
			CF	3.0227	3.0831	3.1700	3.0224	3.0833	3.1722	3.0123	3.0669	3.1477
	100	10	SS	5.2393	5.3077	5.4086	5.2423	5.3167	5.4334	5.2151	5.2740	5.3729
			CC	8.1946	8.1745	8.1523	8.2052	8.2111	8.2608	8.1987	8.2090	8.2710
			CF	3.4809	3.5507	3.6504	3.4803	3.5507	3.6531	3.4709	3.5355	3.6303
20	0	0	SS	3.8259	3.8479	3.8853	3.8341	3.8659	3.9254	3.7865	3.7894	3.8139
			CC	8.5922	8.6305	8.6968	8.6102	8.6716	8.7920	8.5107	8.5127	8.5630
			CF	1.3673	1.3754	1.3891	1.3702	1.3818	1.4033	1.3530	1.3541	1.3629
	100	0	SS	4.7030	4.7598	4.8460	4.7088	4.7729	4.8756	4.6676	4.7065	4.7787
			CC	9.0168	9.0736	9.1661	9.0335	9.1119	9.2551	8.9374	8.9585	9.0339
			CF	3.0594	3.1228	3.2139	3.0594	3.1233	3.2162	3.0478	3.1042	3.1873
	100	10	SS	5.4315	5.5139	5.6357	5.4358	5.5238	5.6591	5.3980	5.4628	5.5694
			CC	9.5085	9.5852	9.7057	9.5238	9.6206	9.7885	9.4314	9.4733	9.5759
			CF	3.5342	3.6090	3.7164	3.5339	3.6090	3.7180	3.5217	3.5889	3.6872

Table 33. Critical buckling loads variation in the Type B beam with different BCs, porosity distributions, and elastic foundation (1-2-1, p = 2)

L/h	K_w	K_p	BCs	e_0								
				UD			SD			ASD		
				0.4	0.6	0.8	0.4	0.6	0.4	0.4	0.6	0.8
5	0	0	SS	30.2135	29.3521	28.2242	30.2522	29.4800	28.5960	30.2713	29.5285	28.6935
			CC	71.8155	67.5924	62.3648	71.6677	67.7367	63.4885	72.0437	68.3602	64.4079
			CF	9.0669	8.9569	8.8143	9.0947	9.0077	8.9074	9.0784	8.9851	8.8807
	100	0	SS	40.4787	39.6141	38.4818	40.5171	39.7417	38.8541	40.5367	39.7910	38.9527
			CC	79.2025	74.9231	69.6113	79.0513	75.0673	70.7524	79.4333	75.7014	71.6890
			CF	21.5344	21.1865	20.7169	21.5585	21.2521	20.8918	21.5590	21.2607	20.9172
	100	10	SS	50.6047	49.7369	48.6002	50.6428	49.8643	48.9730	50.6628	49.9143	49.0728
			CC	89.3498	85.0605	79.7355	89.1976	85.2041	80.8784	89.5810	85.8405	81.8182
			CF	30.9754	30.6127	30.1244	31.0047	30.6879	30.3162	31.0018	30.6912	30.3341
20	0	0	SS	38.3449	38.0925	37.7847	38.4845	38.3238	38.1473	38.3856	38.1756	37.9511
			CC	145.8516	144.0979	141.8237	146.2983	144.9112	143.3127	146.0365	144.5486	142.8840
			CF	9.7274	9.6773	9.6189	9.7643	9.7371	9.7090	9.7372	9.6960	9.6534
	100	0	SS	48.4892	48.2367	47.9289	48.6288	48.4680	48.2915	48.5299	48.3199	48.0953
			CC	153.4313	151.6762	149.4000	153.8780	152.4896	150.8894	153.6163	152.1272	150.4611
			CF	24.8321	24.7517	24.6538	24.8787	24.8289	24.7744	24.8454	24.7788	24.7076
	100	10	SS	58.5012	58.2487	57.9408	58.6408	58.4800	58.3035	58.5418	58.3319	58.1073
			CC	163.4751	161.7197	159.4431	163.9218	162.5330	160.9325	163.6601	162.1707	160.5044
			CF	34.8323	34.7519	34.6540	34.8789	34.8291	34.7745	34.8456	34.7790	34.7077

Table 34. Critical buckling loads variation in the Type C beam with different BCs, porosity distributions, and elastic foundation (12-1, p = 2)

L/h	K_w	K_p	BCs	e_0								
				UD			SD			ASD		
				0.4	0.6	0.8	0.4	0.6	0.4	0.4	0.6	0.8
5	0	0	SS	18.4506	17.6257	16.5807	18.5452	17.8365	17.0511	18.2592	17.4208	16.5241
			CC	59.8978	56.0151	51.0623	60.1714	56.7830	53.0390	60.1542	56.9359	53.5406
			CF	4.8809	4.6959	4.4660	4.9071	4.7497	4.5771	4.8081	4.5997	4.3758
	100	0	SS	28.6858	27.8578	26.8086	28.7794	28.0674	27.2782	28.4918	27.6494	26.7483
			CC	67.4569	63.5434	58.5418	67.7295	64.3137	60.5347	67.7211	64.4838	61.0665
			CF	16.3614	15.9043	15.2968	16.4155	16.0277	15.5820	16.2999	15.8621	15.3788
	100	10	SS	38.7805	37.9494	36.8958	38.8732	38.1579	37.3650	38.5841	37.7376	36.8321
			CC	77.6037	73.6822	68.6692	77.8747	74.4511	70.6629	77.8667	74.6224	71.1974
			CF	25.8352	25.3610	24.7316	25.9020	25.5068	25.0532	25.7920	25.3501	24.8626
20	0	0	SS	19.8405	19.1280	18.2492	19.9477	19.3434	18.6835	19.5178	18.6859	17.7913
			CC	78.3233	75.3566	71.6690	78.7403	76.2150	73.4450	77.1440	73.7950	70.1984
			CF	4.9830	4.8062	4.5887	5.0099	4.8601	4.6968	4.9003	4.6921	4.4681
	100	0	SS	29.9807	29.2681	28.3890	30.0878	29.4834	28.8233	29.6577	28.8256	27.9307
			CC	85.8880	82.9190	79.2280	86.3051	83.7778	81.0054	84.7082	81.3570	77.7577
			CF	17.7433	17.4009	16.9655	17.7937	17.5048	17.1817	17.5925	17.1898	16.7433
	100	10	SS	39.9887	39.2759	38.3966	40.0957	39.4911	38.8308	39.6655	38.8331	37.9378
			CC	95.9180	92.9484	89.2566	96.3349	93.8069	91.0336	94.7374	91.3851	87.7847
			CF	27.7428	27.4003	26.9649	27.7932	27.5042	27.1811	27.5919	27.1893	26.7428

3.4.3. The Effect of Skin-Core-Skin Thickness Ratio

Tables 35 and 36 present the effect of the skin-core-skin thickness ratio on fundamental natural frequencies and critical buckling loads for various porosity patterns and coefficients. It is revealed that the reduction in the skin-core-skin thickness ratio leads to a decrease in fundamental natural frequencies for Type B beams, attributable to a decrease in bending stiffness. Conversely, Type C beams exhibit an increase in frequencies as core thickness increases, resulting in improved bending stiffness. Similarly critical buckling loads decrease consistently with decreasing skin-core-skin thickness ratio.

3.4.4. The Effect of Power Index and Length-To-Thickness Ratio

The influence of the power index and length-to-thickness ratio on the fundamental natural frequencies and critical buckling loads of CC beams with different porosity distributions are visually represented in Figures 22-25. It is noted that increasing the power index enhances fundamental natural frequencies and critical buckling loads for Type B beams but decreases them for Type C beams across all porosity patterns. Similarly, across all porosity patterns, higher length-to-thickness ratios lead to increased natural frequencies and critical buckling loads.

3.4.5. Elastic Foundation Effect

The effect of foundation parameters on the fundamental natural frequencies and critical buckling loads of the beams is given in Tables 37 and 38 for different porosity patterns. Likewise, Figures 26 and 27 graphically demonstrate the influence of Winkler and Pasternak constants on fundamental natural frequencies and critical buckling loads of Type C beams. Linear trends are evident in both cases.

Table 35. Fundamental natural frequencies variation of the beams with different skin-core-skin thickness ratio, BCs, and porosity distributions ($L/h = 5$, $p = 5$, $K_w = 25$, $K_p = 10$)

Type	Scheme	BCs	UD			SD			ASD		
			0.4	0.6	0.8	0.4	0.6	0.8	0.4	0.6	0.8
Type B	2-1-2	SS	5.9176	5.9522	5.9994	5.9183	5.9540	6.0032	5.9182	5.9538	6.0030
		CC	9.9416	9.9719	10.0185	9.9443	9.9798	10.0376	9.9447	9.9804	10.0384
		CF	2.8424	2.8607	2.8853	2.8426	2.8611	2.8863	2.8425	2.8610	2.8862
	1-1-1	SS	5.8948	5.9497	6.0265	5.8966	5.9542	6.0369	5.8963	5.9538	6.0365
		CC	9.5034	9.5298	9.5780	9.5068	9.5438	9.6180	9.5098	9.5488	9.6251
		CF	2.8696	2.9006	2.9434	2.8702	2.9019	2.9463	2.8700	2.9017	2.9461
	1-2-1	SS	5.7687	5.8389	5.9394	5.7714	5.8470	5.9621	5.7721	5.8489	5.9663
		CC	8.8098	8.7901	8.7808	8.8039	8.7989	8.8397	8.8207	8.8273	8.8830
		CF	2.8759	2.9215	2.9859	2.8769	2.9242	2.9929	2.8769	2.9244	2.9936
Type C	2-1-2	SS	4.6028	4.6256	4.6583	4.6047	4.6299	4.6670	4.6015	4.6250	4.6602
		CC	7.8460	7.8566	7.8781	7.8586	7.8811	7.9233	7.8588	7.8816	7.9239
		CF	2.5083	2.5247	2.5473	2.5085	2.5253	2.5489	2.5073	2.5235	2.5463
	1-1-1	SS	4.6360	4.6732	4.7275	4.6395	4.6813	4.7452	4.6278	4.6634	4.7202
		CC	7.7560	7.7604	7.7776	7.7783	7.8063	7.8674	7.7716	7.7971	7.8559
		CF	2.5381	2.5660	2.6052	2.5385	2.5674	2.6089	2.5348	2.5616	2.6007
	1-2-1	SS	4.6783	4.7297	4.8074	4.6876	4.7491	4.8472	4.6573	4.7017	4.7806
		CC	7.6233	7.5999	7.5789	7.6582	7.6761	7.7404	7.8588	7.8816	7.9239
		CF	2.5765	2.6189	2.6798	2.5782	2.6228	2.6892	2.5692	2.6087	2.6692

Table 36. Critical buckling loads variation of the beams with different skin-core-skin thickness ratio, BCs, and porosity distributions ($L/h = 5$, $p = 5$, $K_w = 25$, $K_p = 10$)

Type	Scheme	BCs	UD			SD			USD		
			0.4	0.6	0.8	0.4	0.6	0.8	0.4	0.6	0.8
Type B	2-1-2	SS	56.8269	56.6839	56.5161	56.8413	56.7191	56.5936	56.8388	56.7155	56.5889
		CC	135.4088	134.3620	133.1466	135.4787	134.5662	133.6370	135.4890	134.5824	133.6594
		CF	26.4163	26.4006	26.3821	26.4193	26.4066	26.3935	26.4179	26.4045	26.3906
	1-1-1	SS	53.1604	52.7988	52.3617	53.1942	52.8839	52.5559	53.1893	52.8782	52.5506
		CC	117.4725	115.2651	112.6524	117.5501	115.5901	113.5595	117.6260	115.7107	113.7298
		CF	25.6836	25.6370	25.5808	25.6945	25.6578	25.6189	25.6886	25.6491	25.6074
	1-2-1	SS	47.0380	46.2146	45.1619	47.0797	46.3450	45.5223	47.0949	46.3838	45.5997
		CC	94.1891	90.1149	85.1373	94.0521	90.2651	86.2193	94.4120	90.8544	87.0772
		CF	24.2278	24.1003	23.9372	24.2568	24.1546	24.0390	24.2407	24.1324	24.0126
Type C	2-1-2	SS	31.5345	31.3267	31.0817	31.5833	31.4221	31.2567	31.5547	31.3798	31.2013
		CC	75.3644	74.3543	73.1665	75.6465	74.8854	74.1067	75.6709	74.9286	74.1734
		CF	18.8196	18.7665	18.7036	18.8317	18.7903	18.7476	18.8215	18.7751	18.7276
	1-1-1	SS	30.8751	30.4833	30.0093	30.9621	30.6571	30.3379	30.8311	30.4614	30.0787
		CC	71.2980	69.4067	67.1228	71.7706	70.3307	68.8293	71.6620	70.1924	68.6814
		CF	18.6597	18.5574	18.4330	18.6831	18.6037	18.5203	18.6400	18.5387	18.4331
	1-2-1	SS	30.0065	29.2949	28.4110	30.1896	29.6437	29.0563	29.8378	29.1160	28.3559
		CC	66.0736	62.8283	58.7845	66.7802	64.2465	61.5288	75.6709	74.9286	74.1734
		CF	18.4343	18.2392	17.9945	18.4915	18.3462	18.1887	18.3751	18.1682	17.9472

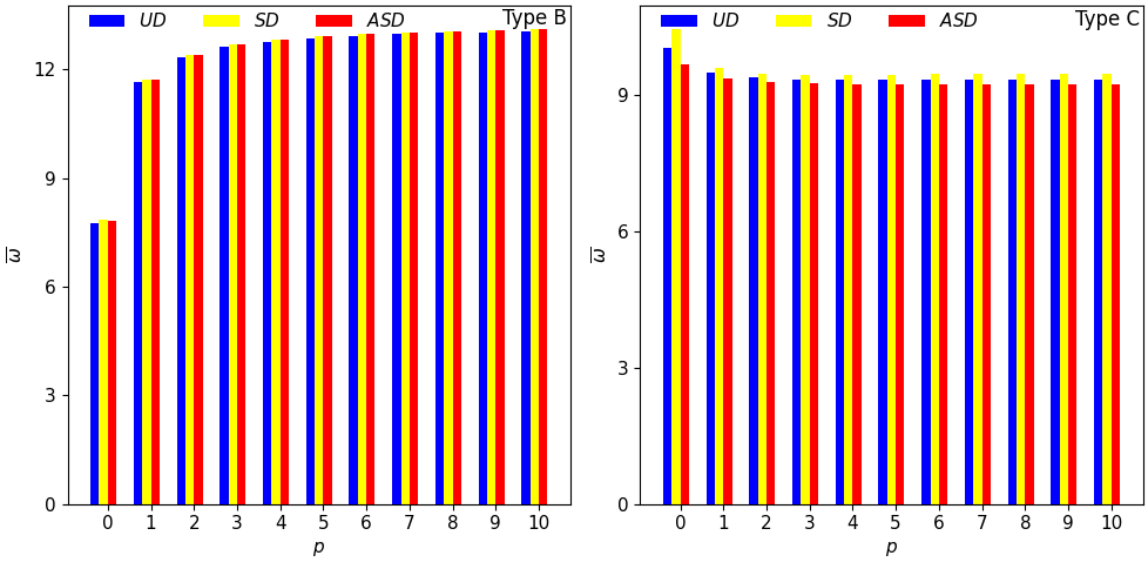

Figure 22. Effect of power index on fundamental natural frequencies in CC beams across different porosity distributions (1-2-1, $L/h = 15$, $e_0 = 0.8$, $K_w = 25$, $K_p = 10$)

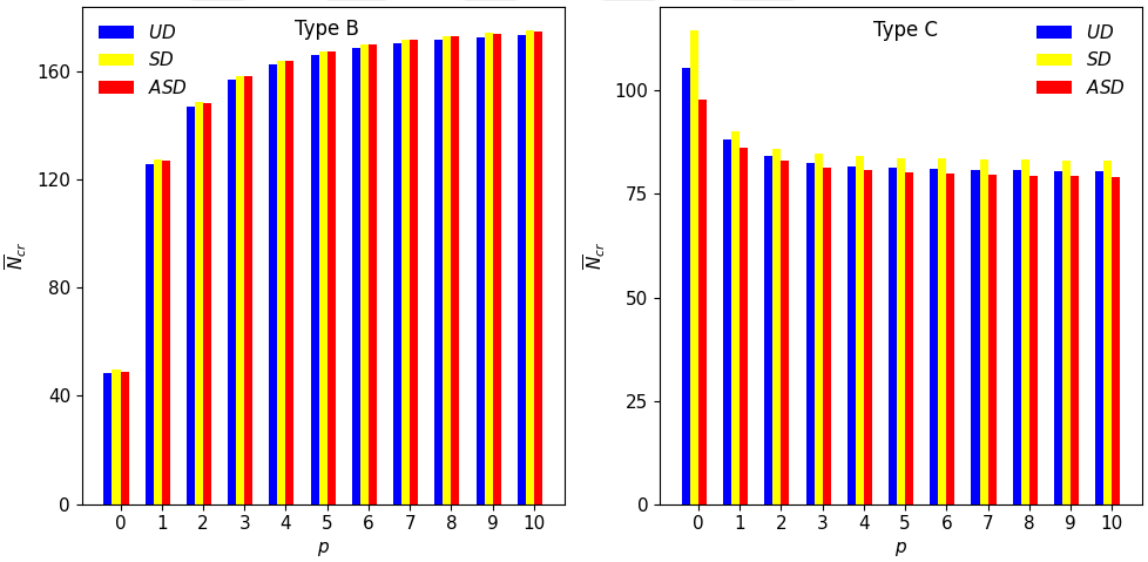

Figure 23. Effect of power index on critical buckling loads in CC beams across different porosity distributions (1-2-1, $L/h = 15$, $e_0 = 0.8$, $K_w = 25$, $K_p = 10$)

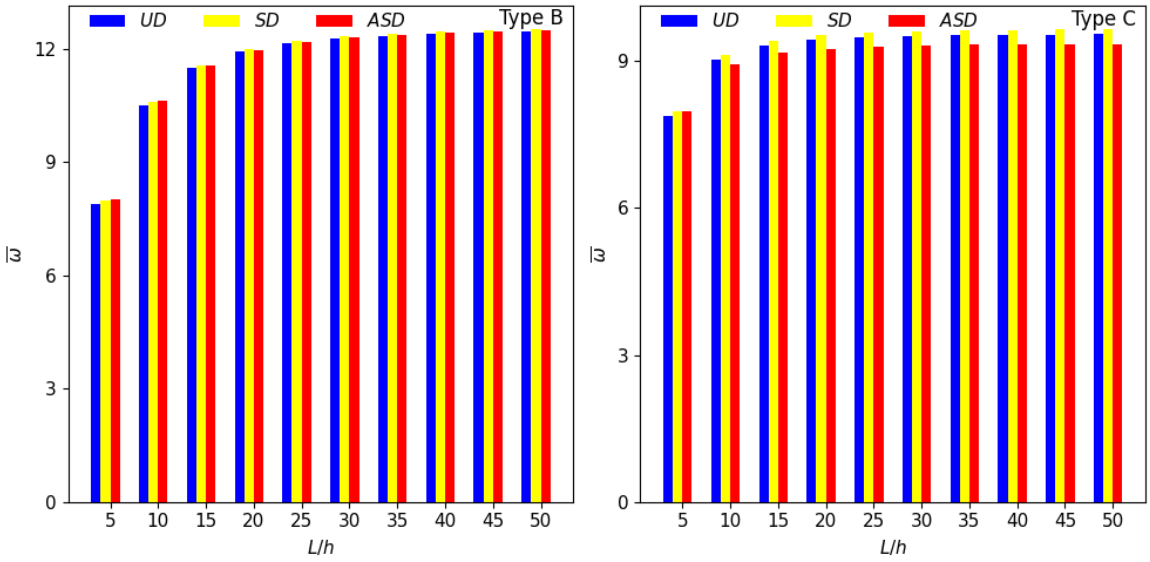

Figure 24. Effect of length-to-thickness ratio on fundamental natural frequencies in CC beams across different porosity distributions (1-2-1, $e_0 = 0.8$, $K_w = K_p = 10$, $p = 1$)

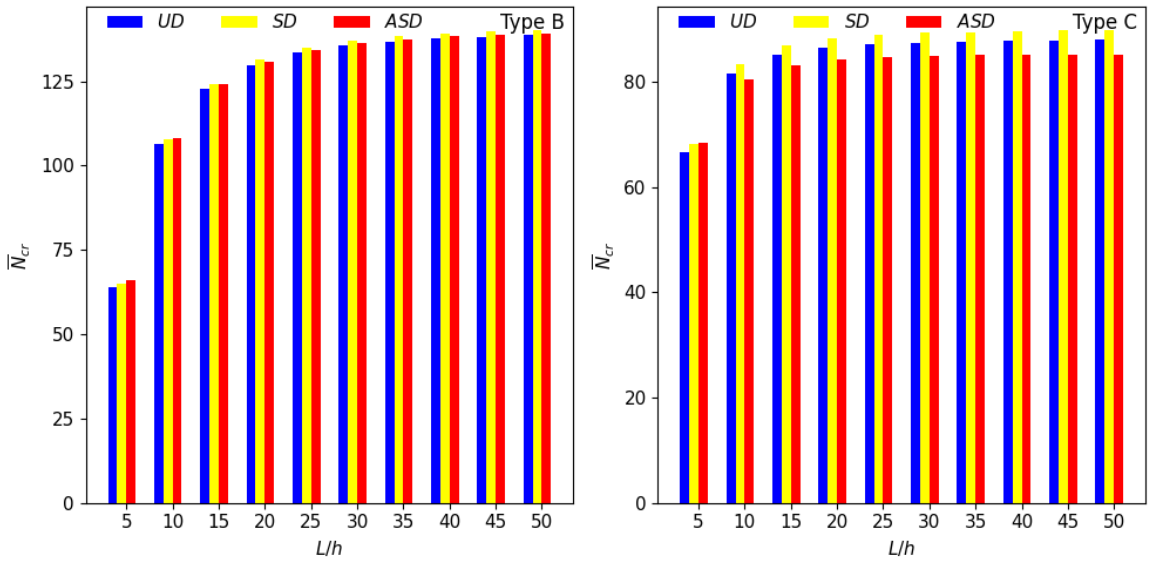

Figure 25. Effect of length-to-thickness ratio on critical buckling loads in CC beams across different porosity distributions (1-2-1, $e_0 = 0.8$, $K_w = K_p = 10$, $p = 1$)

Table 37. Effect foundation parameters on fundamental frequencies of FGSBs (1-2-1, L/h = 5, e_0 = 0.5, p = 5)

Type	K_p	BCs	UD			SD			USD		
			K_w								
			0	50	100	0	50	100	0	50	100
Type B	0	SS	5.3099	5.6480	4.9543	5.3152	5.6530	4.9558	5.3165	5.6542	5.3099
		CC	8.4438	8.6636	8.2168	8.4426	8.6624	8.2407	8.4657	8.6850	8.4438
		CF	2.7118	3.3293	1.9067	2.7139	3.3309	1.9056	2.7132	3.3304	2.7118
	10	SS	5.9589	6.2620	5.6444	5.9636	6.2665	5.6456	5.9647	6.2675	5.9589
		CC	8.9056	9.1143	8.6908	8.9045	9.1132	8.7133	8.9265	9.1347	8.9056
		CF	3.2036	3.7420	2.5561	3.2051	3.7432	2.5561	3.2052	3.7433	3.2036
	25	SS	6.8174	7.0839	6.5443	6.8215	7.0878	6.5453	6.8224	7.0887	6.8174
		CC	9.5513	9.7462	9.3513	9.5503	9.7452	9.3724	9.5709	9.7654	9.5513
		CF	3.7502	4.2203	3.2133	3.7513	4.2212	3.2142	3.7520	4.2219	3.7502
Type C	0	SS	4.0608	4.5058	3.5821	4.0784	4.5205	3.5336	4.0350	4.4805	4.0608
		CC	7.1598	7.4247	6.9439	7.2159	7.4780	6.9180	7.1903	7.4525	7.1598
		CF	2.3701	3.0805	1.3279	2.3720	3.0803	1.3070	2.3590	3.0692	2.3701
	10	SS	4.9004	5.2749	4.5095	4.9128	5.2854	4.4695	4.8754	5.2500	4.9004
		CC	7.7375	7.9833	7.5372	7.7886	8.0321	7.5140	7.7655	8.0090	7.7375
		CF	2.9471	3.5461	2.1940	2.9485	3.5458	2.1811	2.9378	3.5360	2.9471
	25	SS	5.9408	6.2531	5.6201	5.9484	6.2595	5.5862	5.9158	6.2279	5.9408
		CC	8.5195	8.7435	8.3368	8.5649	8.7870	8.3166	8.5446	8.7666	8.5195
		CF	3.5359	4.0500	2.9367	3.5375	4.0500	2.9259	3.5276	4.0406	3.5359

Table 38. Effect of foundation parameters on critical buckling loads of FGSBs (1-2-1, L/h = 5, e_0 = 0.5, p = 5)

Type	K_p	BCs	UD			SD			USD		
			K_w								
			0	50	100	0	50	100	0	50	100
Type B	0	SS	33.9500	39.0830	44.2148	34.0264	39.1592	44.2908	34.0511	39.1842	44.3160
		CC	80.1628	83.9512	87.5819	80.1216	83.9092	87.5385	80.5894	84.3789	88.0124
		CF	10.2220	17.8497	23.1496	10.2603	17.8886	23.1901	10.2401	17.8744	23.1881
	10	SS	44.0809	49.2115	54.3409	44.1570	49.2874	54.4166	44.1822	49.3129	54.4424
		CC	90.3208	94.1052	97.7289	90.2787	94.0623	97.6847	90.7481	94.5335	98.1601
		CF	20.0995	27.5432	32.6499	20.1387	27.5848	32.6952	20.1179	27.5692	32.6904
	25	SS	59.2684	64.3954	69.5212	59.3441	64.4709	69.5966	59.3700	64.4971	69.6230
		CC	105.5231	109.2997	112.9106	105.4798	109.2556	112.8654	105.9513	109.7290	113.3430
		CF	34.6672	41.6901	46.3677	34.7106	41.7415	46.4295	34.6873	41.7206	46.4152
Type C	0	SS	17.0137	22.1291	27.2427	17.2699	22.3852	27.4987	16.8328	21.9469	27.0592
		CC	52.4637	56.2649	59.9517	53.4780	57.2808	60.9735	53.0624	56.8674	60.5678
		CF	4.5804	11.5471	15.5345	4.6427	11.6435	15.6848	4.4981	11.4807	15.4884
	10	SS	27.1094	32.2212	37.3312	27.3653	32.4771	37.5870	26.9259	32.0365	37.1453
		CC	62.6092	66.4031	70.0810	63.6235	67.4192	71.1031	63.2076	67.0054	70.6973
		CF	14.4741	21.2031	24.9816	14.5391	21.3102	25.1488	14.3960	21.1506	24.9587
	25	SS	42.2396	47.3460	52.4507	42.4954	47.6019	52.7065	42.0525	47.1578	52.2613
		CC	77.7772	81.5581	85.2201	78.7923	82.5753	86.2439	78.3759	82.1611	85.8379
		CF	28.9777	35.0850	38.3594	29.0603	35.2385	38.5931	28.9202	35.0842	38.4153

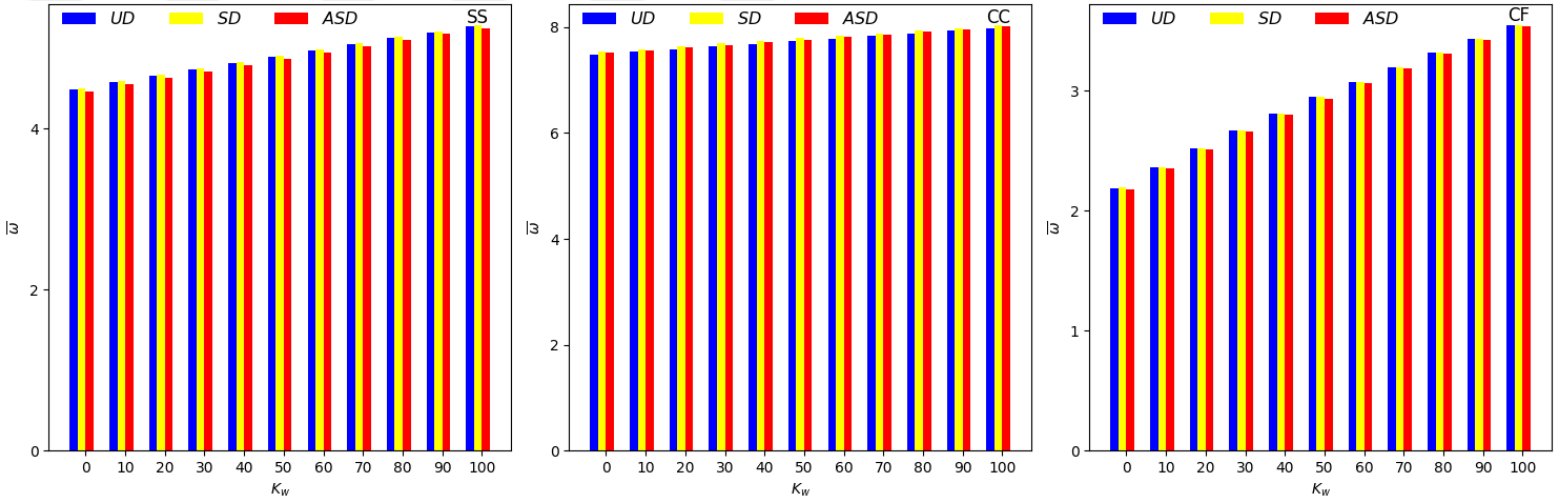

(a) with respect to K_w (K_p = 10)

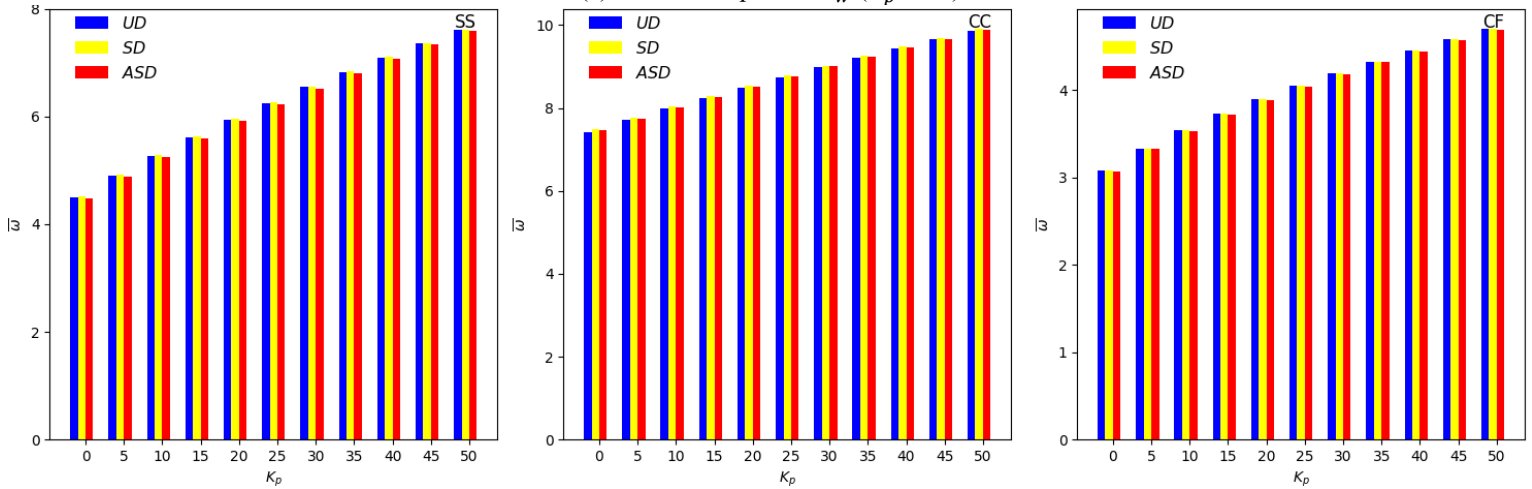

(b) with respect to K_p (K_w= 100)

Figure 26. Effect of Winkler and Pasternak foundation on fundamental frequencies of Type C beam with different BCs and porosity distributions (1-2-1, L/h = 5, e_0 = 0.8, p = 5) under K_w and K_p

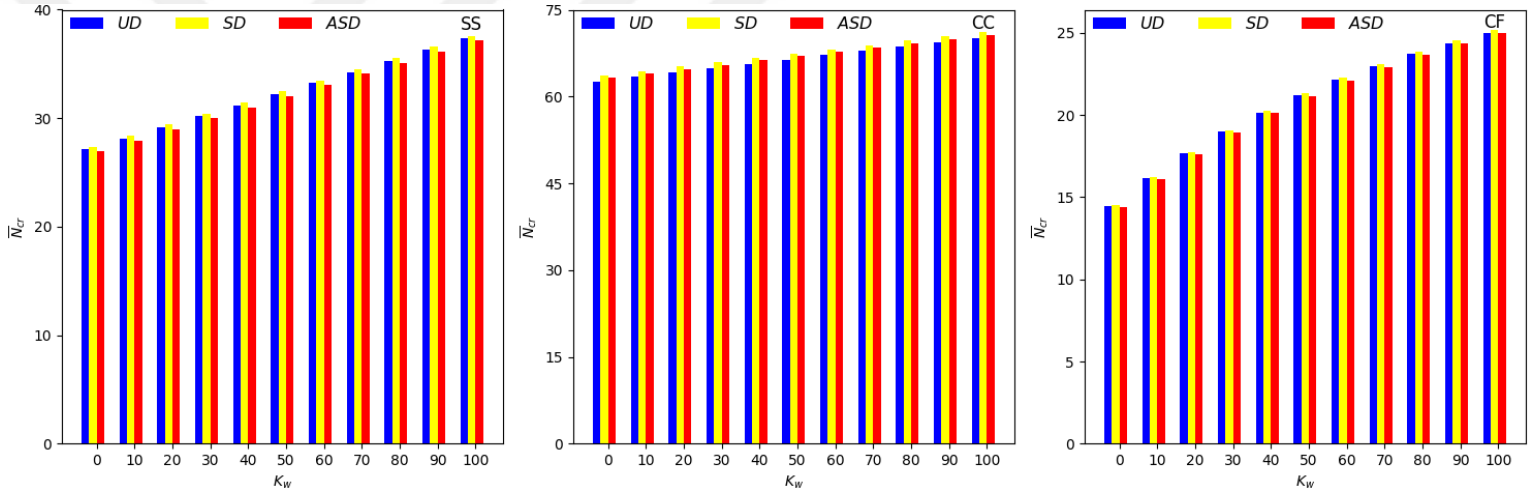

(a) with respect to K_w (K_p = 10)

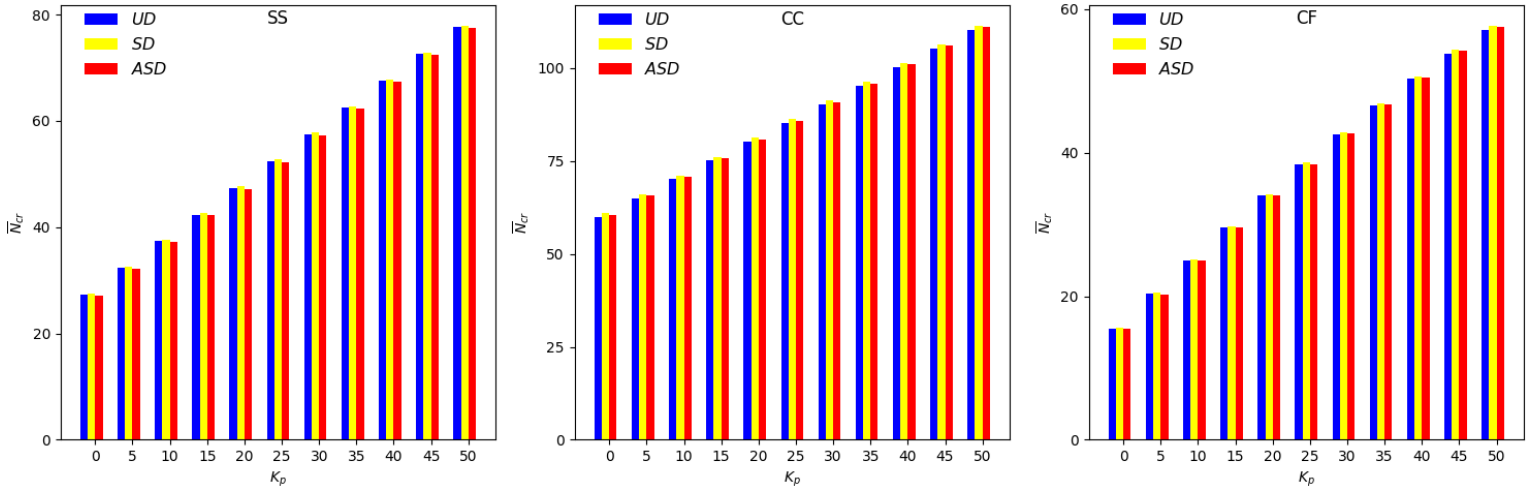

(b) with respect to K_p (K_w= 100)

Figure 27. Effect of Winkler and Pasternak foundation on the critical buckling loads of Type C beam with different BCs and porosity distributions (1-2-1, L/h = 5, e_0 = 0.8, p = 5) under K_w and K_p

3.5. Static Analysis of FGSBs with Porous Core Resting on Elastic Foundation Using FEM

3.5.1. Convergence and Validation Study

The accuracy of the proposed FE model is further validated through a static analysis for Type A and Type C beams. A comparison of normalized maximum vertical displacements for non-porous FG sandwich beams is presented in Tables 39 and 40. The results of the current study are compared with those obtained using different HSDTs (Sayyad & Avhad, 2019; Vo et al., 2015b) and a quasi-3D theory (Vo et al., 2015b). The proposed FE model demonstrates exceptional accuracy in predicting normalized maximum vertical displacements, as evidenced by the close agreement with reference studies, particularly those incorporating transverse normal deformation effects. Additionally, the tables indicate that as the power-law index increases, the maximum vertical displacements of the beams increase accordingly. This trend can be explained by the increased proportion of the metal phase at higher power-law indices, which leads to a reduction in bending stiffness, thereby increasing the flexibility of the beam. In addition, the maximum vertical displacements of the beams decrease in the following sequence: CF, SS, and CC. In addition to the power-law index, it becomes apparent that the slenderness ratio and boundary conditions affect maximum vertical displacement, with their effects being more pronounced in CC beams than in SS and CF beams.

For completeness, Tables 41 and 42 present a comparison of maximum axial normal stress $\bar{\sigma}_x$, vertical normal stress $\bar{\sigma}_z$ and shear stress $\bar{\sigma}_{xz}$ for SS beams (Type A: 1-2-1, Type C: 1-8-1). The proposed FE model accurately captures the stress distributions of the beams, as confirmed by comparisons with existing studies. Notably, maximum axial stress decreases for Type A and increases for Type C, while vertical stress shows a varied behavior. Shear stress increases for Type A and decreases for Type C. These trends are directly correlated to the metal phase content, which influences Young's modulus and bending stiffness.

Table 39. The nondimensional maximum vertical displacements of Type A beams (1-2-1)

L/h	BC	Theory	p				
			0	1	2	5	10
5	SS	Present	3.1397	5.3612	6.6914	8.4278	9.3101
		HSDT[3]	3.1241	5.0341	6.3359	8.0576	8.9290
		HSDT[4]	3.1654	5.4122	6.7579	8.5137	9.4050
		Quasi-3D[3]	3.1397	5.3612	6.6913	8.4276	9.3099
	CC	Present	0.8323	1.3072	1.5852	1.9417	2.1212
		HSDT[4]	0.8501	1.3372	1.6225	1.9896	2.1747
		Quasi-3D[3]	0.8327	1.3077	1.5853	1.9416	2.1211
	CF	Present	28.5532	49.7415	62.4630	79.0683	87.4969
		HSDT[4]	28.7555	50.0741	62.8813	79.6213	88.1270
		Quasi-3D[3]	28.5524	49.7281	62.4386	79.0288	87.4501
20	SS	Present	2.8947	5.0976	6.4236	8.1591	9.0414
		HSDT[3]	2.8585	5.3415	6.6697	8.4045	9.2824
		HSDT[4]	2.8963	5.1006	6.4276	8.1642	9.0471
		Quasi-3D[3]	2.8947	5.0975	6.4235	8.1589	9.0413
	CC	Present	0.5893	1.0294	1.2938	1.6394	1.8149
		HSDT[4]	0.5933	1.0365	1.3028	1.6512	1.8282
		Quasi-3D[3]	0.5894	1.0293	1.2936	1.6390	1.8145
	CF	Present	27.6219	48.6886	61.3682	77.9597	86.3942
		HSDT[4]	27.7029	48.8489	61.5809	78.2451	86.7178
		Quasi-3D[3]	27.6217	48.6985	61.3855	77.9869	86.4264

HSDT[3] (Sayyad and Avhad, 2019), HSDT[4] (Vo et al., 2015b), Quasi-3D[3] (Vo et al., 2015b)

Table 40. The nondimensional maximum vertical displacement of Type C beams (1-2-1)

L/h	BC	Theory	p				
			0	1	2	5	10
5	SS	Present	3.9374	6.5506	7.7722	8.8090	9.2428
		HSDT[4]	3.9788	6.7166	8.0083	9.0691	9.4817
		Quasi-3D[3]-FEM	3.9374	6.5499	7.7711	8.8078	9.2417
		Quasi-3D[3]-Navier	3.9374	6.5505	7.7721	8.8089	9.2426
	CC	Present	1.0049	1.6540	2.0119	2.4588	2.7081
		HSDT[4]	1.0273	1.7079	2.0825	2.5386	2.7866
		Quasi-3D[3]	1.0046	1.6539	2.0122	2.4595	2.7089
	CF	Present	36.1528	60.2074	71.0318	79.0851	81.9766
		HSDT[4]	36.4685	61.7373	73.2441	81.5334	84.2168
		Quasi-3D[3]	36.1509	60.2081	71.0316	79.0886	81.9813
20	SS	Present	3.6840	6.1381	7.2141	7.9433	8.1707
		HSDT[4]	3.6934	6.2638	7.4085	8.1587	8.3619
		Quasi-3D[3]-FEM	3.6840	6.1377	7.2133	7.9425	8.1700
		Quasi-3D[3]-Navier	3.6841	6.1383	7.2143	7.9435	8.1710
	CC	Present	0.7472	1.2447	1.4670	1.6284	1.6845
		HSDT[4]	0.7536	1.2759	1.5122	1.6784	1.7300
		Quasi-3D[3]	0.7472	1.2447	1.4669	1.6283	1.6843
	CF	Present	35.1768	58.6484	68.9200	75.8028	77.9023
		HSDT[4]	35.3495	59.9664	70.9018	77.9882	79.8588
		Quasi-3D[3]	35.1767	58.6432	68.9096	75.7851	77.8811

HSDT[3] (Sayyad and Avhad, 2019), HSDT[4] (Vo et al., 2015b), Quasi-3D[3] (Vo et al., 2015b)

Table 41. Comparison of maximum axial stress $\bar{\sigma}_x$vertical stress $\bar{\sigma}_z$ and shear stress $\bar{\sigma}_{xz}$ of Type A beams (1-2-1)

L/h	BC	Theory	p				
			0	1	2	5	10
5	$\bar{\sigma}_x$	Present	3.8001	1.2313	1.5503	1.9670	2.1786
		HSDT[3]	3.8020	1.2329	1.5527	1.9705	2.1826
		HSDT[4]	3.8025	1.2331	1.5530	1.9707	2.1829
		Quasi-3D[3]	3.8005	1.2315	1.5505	1.9672	2.1788
	$\bar{\sigma}_z$	Present	0.1352	0.0447	0.0564	0.0712	0.0783
		HSDT[4]	0.1352	0.0447	0.0564	0.0712	0.0783
		Quasi-3D[3]	0.7237	0.7994	0.8348	0.8761	0.8978
	$\bar{\sigma}_{xz}$	Present	0.7332	0.8123	0.8493	0.8925	0.9151
		HSDT[4]	0.7285	0.8056	0.8424	0.8851	0.9083
		Quasi-3D[3]	0.7233	0.7993	0.8349	0.8763	0.8980
20	$\bar{\sigma}_x$	Present	15.0109	4.8792	6.1519	7.8177	8.6646
		HSDT[3]	15.0129	4.8801	6.1532	7.8194	8.6665
		HSDT[4]	15.0136	4.8802	6.1534	7.8196	8.6667
		Quasi-3D[3]	15.0125	4.8797	6.1526	7.8185	8.6655
	$\bar{\sigma}_z$	Present	0.0337	0.0111	0.0141	0.0177	0.0195
		HSDT[4]	0.0337	0.0111	0.0141	0.0178	0.0195
		Quasi-3D[3]	0.7436	0.8192	0.8553	0.8980	0.9207
	$\bar{\sigma}_{xz}$	Present	0.7451	0.8215	0.8581	0.9014	0.9243
		HSDT[4]	0.7355	0.8106	0.8486	0.8897	0.9128
		Quasi-3D[3]	0.7432	0.8193	0.8556	0.8986	0.9214

HSDT[3] (Sayyad and Avhad, 2019), HSDT[4] (Vo et al., 2015b), Quasi-3D[3] (Vo et al., 2015b)

Table 42. Comparison of maximum axial stress $\bar{\sigma}_x$vertical stress $\bar{\sigma}_z$ and shear stress $\bar{\sigma}_{xz}$ of Type C beams (1-8-1)

L/h	BC	Theory	p				
			0	1	2	5	10
5	$\bar{\sigma}_x$	Present	4.4610	6.0077	6.5262	6.8939	7.2305
		HSDT[4]	4.4660	6.0130	6.5290	6.8930	7.2270
		Quasi-3D[3]-FEM	4.4620	6.0100	6.5290	6.8970	7.2330
		Quasi-3D[3]-Navier	4.4603	6.0069	6.5253	6.8927	7.2292
	$\bar{\sigma}_z$	Present	0.0873	0.1044	0.1277	0.0620	0.0000
		HSDT[4]	0.0872	0.1043	0.1277	0.0619	-0.0001
		Quasi-3D[3]	0.0873	0.1045	0.1279	0.0622	-0.0001
	$\bar{\sigma}_{xz}$	Present	0.7490	0.7223	0.6370	0.5266	0.5738
		HSDT[4]	0.7611	0.7315	0.6432	0.5316	0.5798
		Quasi-3D[3]	0.7568	0.7272	0.6395	0.5286	0.5766
		Present	0.7486	0.7219	0.6365	0.5262	0.5733
20	$\bar{\sigma}_x$	HSDT[4]	17.6340	23.7103	25.6879	26.9741	28.2341
		Quasi-3D[3]-FEM	17.6400	23.7200	25.7000	26.9800	28.2400
		Quasi-3D[3]-Navier	17.6400	23.7200	25.7000	26.9900	28.2500
		Present	17.6318	23.7073	25.6848	26.9703	28.2298
	$\bar{\sigma}_z$	HSDT[4]	-0.2903	-0.4371	-0.4177	-0.8040	-1.1446
		Quasi-3D[3]	-0.2904	-0.4373	-0.4179	-0.8042	-1.1450
		Present	-0.2901	-0.4367	-0.4170	-0.8032	-1.1440
	$\bar{\sigma}_{xz}$	HSDT[4]	0.7685	0.7422	0.6548	0.5419	0.5905
		Quasi-3D[3]	0.7785	0.7416	0.6452	0.5400	0.5969
		Present	0.7777	0.7412	0.6454	0.5399	0.5963
		HSDT[4]	0.7683	0.7418	0.6543	0.5414	0.5900

HSDT[3] (Sayyad and Avhad, 2019), HSDT[4] (Vo et al., 2015b), Quasi-3D[3] (Vo et al., 2015b)

3.5.2. Porosity Effect

Tables 43 and 44 illustrate the impact of porosity on maximum vertical displacements of the beams subjected to three foundation conditions: no foundation, Winkler, and Pasternak. The analysis includes three core porosity patterns with different porosity coefficient values. Regardless of porosity patterns, BCs, or length-to-thickness ratios, a consistent increase in maximum vertical displacement is observed with increase of porosity coefficient. The observed phenomenon can be explained by the decrease in bending stiffness as porosity increases, which results in enhanced beam deflection. Type A beams consistently exhibit lower maximum vertical displacement than Type C beams under all conditions. This is a direct consequence of the superior bending stiffness

provided by the FG face layers in Type A, which effectively mitigates the negative impact of core porosity on overall beam rigidity. The incorporation of the Winkler parameter results in a reduction of nondimensional vertical displacement by providing additional support and stability. The inclusion of the Pasternak foundation further reduces displacements through increased shear stiffness and bending resistance.

Table 45 presents the variation of nondimensional maximum axial normal, vertical normal, and shear stresses for SS beams with different porosity patterns and varying porosity coefficients. The results indicate a consistent increase in nondimensional maximum axial normal stress with increasing the parameter e_0, regardless of porosity pattern. A positive correlation between vertical normal stress and porosity coefficient is observed for Type A, whereas an inverse relationship is exhibited for Type C. Shear stress consistently decreases with increasing porosity for both types. These stress behaviors are directly linked to the reduction in bending stiffness induced by core porosity. Furthermore, the incorporation of elastic foundation parameters leads to a decrease in all stress components.

The variation in maximum vertical displacement of the beams with respect to the porosity coefficient is depicted in Figures 28 and 29. The figures demonstrate that maximum vertical displacement increases with increasing porosity coefficient across all BCs and porosity distributions. The effect of porosity patterns becomes more pronounced at higher porosity coefficients. SD leads to smaller vertical displacements due to its superior stiffness distribution along the beam length compared to other patterns.

The nondimensional stress distributions through the thickness of SS beams with different porosity patterns are given in Figures 30 and 31. A notable correlation between core porosity and the stress distributions has been observed. A consistent increase in axial normal stress is observed for both Type A and Type C beams as the porosity coefficient increases. This phenomenon is attributed to the reduced bending stiffness resulting from increased core porosity, leading to higher stress levels under identical loading conditions. For Type A beams, vertical normal stresses increase with increase of porosity coefficient due to the graded porosity, which reduces stiffness towards the core, allowing greater deformation in response to the applied load, resulting in elevated vertical normal stresses.

Type C beams demonstrate a decrease in vertical stress with rising porosity. This is attributed to more evenly distributed stresses across the beam's thickness due to the progressive material variation from the dense and homogeneous face sheets to the porous

core. A consistent reduction in shear stresses is observed as the porosity coefficient increases. This is attributed to the lower shear modulus of the porous core relative to the dense face sheets, leading to diminished shear stress transmission through the beam thickness. The observed stress discontinuities at the interfaces between the face sheets and the core layer are a direct result of the material composition gradation. This gradient, induced by porosity variations, leads to abrupt changes in material properties. The magnitude of the stress jump at the face-core interfaces increases with the growing porosity coefficient. This effect is exacerbated in ASD due to their uneven material property gradation, leading to more pronounced property mismatches between layers.

3.5.3. The Effect of Skin-Core-Skin Thickness Ratio

The effect of the skin-core-skin thickness ratio on maximum vertical displacement varies among porosity patterns, as shown in Tables 46 and 47. Type A beams show decreased displacement as this ratio increases due to the enhanced bending stiffness from a thicker porous core. The 2-1-2 ratio yields the lowest displacement for Type A beams, while the 1-2-1 ratio results in the highest. Conversely, Type C beams display increased displacement with a decreasing ratio, exhibiting the opposite trend. This occurs because the functionally graded core amplifies the reduction in bending stiffness caused by increased core thickness.

3.5.4. The Effect of Length-To-Thickness Ratio

Figure 32 displays the effect of the length-to-thickness ratio (L/h) on the maximum vertical displacements of CF beams across three porosity distribution patterns. As L/h increases, the nondimensional maximum vertical displacement consistently decreases for all patterns. The effect of porosity distributions on displacement becomes more significant at higher L/h ratios, as the beam's overall stiffness and mechanical behavior become increasingly sensitive to porosity variations.

Table 43. Variation of maximum vertical displacements of Type A beams for various porosity distributions and elastic foundation models (1-2-1, $p = 2$)

L/h	K_w	K_p	BCs	e_0								
				UD			SD			ASD		
				0.4	0.6	0.8	0.4	0.6	0.8	0.4	0.6	0.8
5	0	0	SS	7.2959	7.6938	8.2313	7.0609	7.2819	7.5439	7.2458	7.5960	8.0245
			CC	1.7792	1.9183	2.1288	1.7378	1.8402	1.9762	1.4145	1.4910	1.5868
			CF	67.7269	71.0884	75.4536	65.4273	67.0986	68.9631	67.2633	70.2395	73.8202
	100	0	SS	4.9083	5.0842	5.3116	4.8007	4.9008	5.0166	4.8856	5.0416	5.2257
			CC	1.5926	1.7028	1.8659	1.5593	1.6409	1.7475	1.5828	1.6784	1.7996
			CF	13.8689	13.9642	14.0638	13.7794	13.8212	13.8579	13.8524	13.9392	14.0295
	100	10	SS	3.7079	3.8067	3.9316	3.6461	3.7030	3.7679	3.6949	3.7829	3.8849
			CC	1.4223	1.5103	1.6387	1.3960	1.4619	1.5471	1.4145	1.4910	1.5868
			CF	10.1261	10.1824	10.2465	10.0819	10.1115	10.1419	10.1175	10.1683	10.2232
20	0	0	SS	6.9421	7.2663	7.6752	6.6986	6.8465	7.0028	6.8944	7.1823	7.5243
			CC	1.4016	1.4701	1.5583	1.3536	1.3869	1.4235	1.3920	1.4527	1.5254
			CF	66.3072	69.3895	73.2660	63.9764	65.3715	66.8364	65.8528	68.5921	71.8420
	100	0	SS	4.7585	4.9085	5.0915	4.6429	4.7134	4.7868	4.7361	4.8701	5.0247
			CC	1.2847	1.3420	1.4151	1.2443	1.2723	1.3031	1.2767	1.3275	1.3879
			CF	13.8711	13.9796	14.1021	13.7808	13.8340	13.8870	13.8540	13.9523	14.0588
	100	10	SS	3.6295	3.7159	3.8196	3.5620	3.6032	3.6458	3.6165	3.6939	3.7820
			CC	1.1652	1.2122	1.2717	1.1319	1.1551	1.1806	1.1586	1.2004	1.2497
			CF	10.0722	10.1279	10.1910	10.0264	10.0542	10.0822	10.0636	10.1141	10.1687

Table 44. Variation of maximum vertical displacements of Type C beams for various porosity distributions and elastic foundation models (1-2-1, p = 2)

L/h	K_w	K_p	BCs	e_0								
				UD			SD			ASD		
				0.4	0.6	0.8	0.4	0.6	0.8	0.4	0.6	0.8
5	0	0	SS	8.4058	8.7952	9.3432	8.3622	8.6906	9.0860	8.4936	8.8991	9.3781
			CC	2.1932	2.3485	2.5814	2.1822	2.3146	2.4807	2.1786	2.3012	2.4464
			CF	76.6794	79.8023	84.0786	76.2715	78.8874	81.9798	77.7728	81.3342	85.5383
	100	0	SS	5.3863	5.5423	5.7529	5.3685	5.5009	5.6552	5.4231	5.5852	5.7696
			CC	1.9149	2.0317	2.2029	1.9065	2.0064	2.1294	1.9040	1.9968	2.1050
			CF	14.0614	14.1185	14.1809	14.0500	14.0980	14.1462	14.1024	14.1800	14.2611
	100	10	SS	3.9739	4.0575	4.1681	3.9643	4.0354	4.1171	3.9944	4.0812	4.1784
			CC	1.6751	1.7647	1.8938	1.6687	1.7454	1.8386	1.6661	1.7370	1.8187
			CF	10.2457	10.2845	10.3317	10.2396	10.2725	10.3079	10.2615	10.3056	10.3523
20	0	0	SS	7.7763	8.0657	8.4537	7.7345	7.9758	8.2572	7.9048	8.2565	8.6714
			CC	1.5830	1.6460	1.7318	1.5746	1.6273	1.6894	1.6066	1.6796	1.7658
			CF	74.2935	77.0353	80.7019	73.8944	76.1807	78.8411	75.5431	78.9000	82.8600
	100	0	SS	5.1359	5.2603	5.4223	5.1176	5.2220	5.3410	5.1916	5.3409	5.5112
			CC	1.4354	1.4870	1.5566	1.4285	1.4717	1.5223	1.4548	1.5144	1.5840
			CF	14.1303	14.2064	14.2988	14.1184	14.1829	14.2526	14.1673	14.2577	14.3539
	100	10	SS	3.8445	3.9137	4.0024	3.8343	3.8925	3.9580	3.8757	3.9580	4.0506
			CC	1.2882	1.3297	1.3853	1.2826	1.3174	1.3580	1.3037	1.3514	1.4066
			CF	10.2071	10.2463	10.2941	10.2011	10.2344	10.2704	10.2254	10.2714	10.3203

Table 45. Variation of maximum stresses in SS beams with different porosity distributions and elastic foundation models (L/h = 5,1-2-1, p = 2)

Type	K_w	K_p	Stress	e_0								
				UD			SD		ASD			
				0.4	0.6	0.8	0.4	0.6	0.4	0.4	0.6	0.8
Type A	0	0	$\bar{\sigma}_x$	1.6770	1.7568	1.8583	1.6191	1.6569	1.6976	1.6186	1.6548	1.6925
			$\bar{\sigma}_z$	0.0612	0.0644	0.0688	0.0596	0.0617	0.0642	0.0482	0.0431	0.0372
			$\bar{\sigma}_{xz}$	0.7841	0.7447	0.6790	0.6490	0.5093	0.3098	0.7604	0.7078	0.6359
	100	0	$\bar{\sigma}_x$	1.1180	1.1498	1.1867	1.0912	1.1049	1.1180	1.0815	1.0878	1.0908
			$\bar{\sigma}_z$	0.0543	0.0568	0.0601	0.0529	0.0544	0.0561	0.0455	0.0426	0.0392
			$\bar{\sigma}_{xz}$	0.5712	0.5352	0.4792	0.4767	0.3712	0.2237	0.5550	0.5104	0.4519
	100	10	$\bar{\sigma}_x$	0.8403	0.8565	0.8739	0.8247	0.8307	0.8356	0.8138	0.8120	0.8066
			$\bar{\sigma}_z$	0.0512	0.0535	0.0564	0.0498	0.0510	0.0525	0.0445	0.0426	0.0406
			$\bar{\sigma}_{xz}$	0.4572	0.4252	0.3771	0.3829	0.2967	0.1778	0.4445	0.4062	0.3570
Type C	0	0	$\bar{\sigma}_x$	6.5434	6.6064	6.6719	6.4772	6.5029	6.5270	6.5873	6.6833	6.7910
			$\bar{\sigma}_z$	0.1792	0.1673	0.1507	0.1859	0.1800	0.1733	0.2186	0.2335	0.2515
			$\bar{\sigma}_{xz}$	0.5246	0.4839	0.4199	0.4268	0.3222	0.1857	0.4823	0.4222	0.3503
	100	0	$\bar{\sigma}_x$	4.1387	4.1056	4.0459	4.1045	4.0595	4.0024	4.1508	4.1359	4.1151
			$\bar{\sigma}_z$	0.1730	0.1661	0.1567	0.1763	0.1725	0.1682	0.1971	0.2060	0.2163
			$\bar{\sigma}_{xz}$	0.3675	0.3346	0.2852	0.2993	0.2235	0.1272	0.3369	0.2911	0.2379
	100	10	$\bar{\sigma}_x$	3.0315	2.9834	2.9090	3.0090	2.9559	2.8914	3.0345	2.9986	2.9557
			$\bar{\sigma}_z$	0.1716	0.1673	0.1613	0.1733	0.1707	0.1678	0.1886	0.1952	0.2027
			$\bar{\sigma}_{xz}$	0.2879	0.2603	0.2198	0.2346	0.1741	0.0984	0.2638	0.2265	0.1838

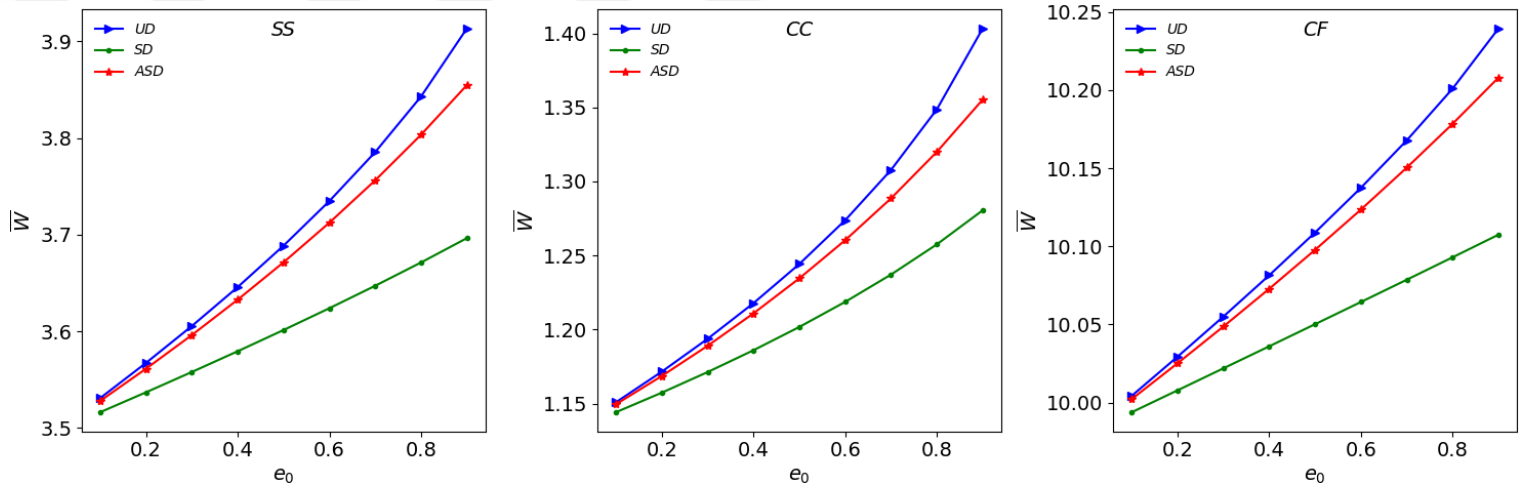

Figure 28. Porosity coefficient effect on the maximum vertical displacement of Type A beams (1-2-1, $L/h = 10$, $p = 2$, $K_w = 100$,$K_p = 10$)

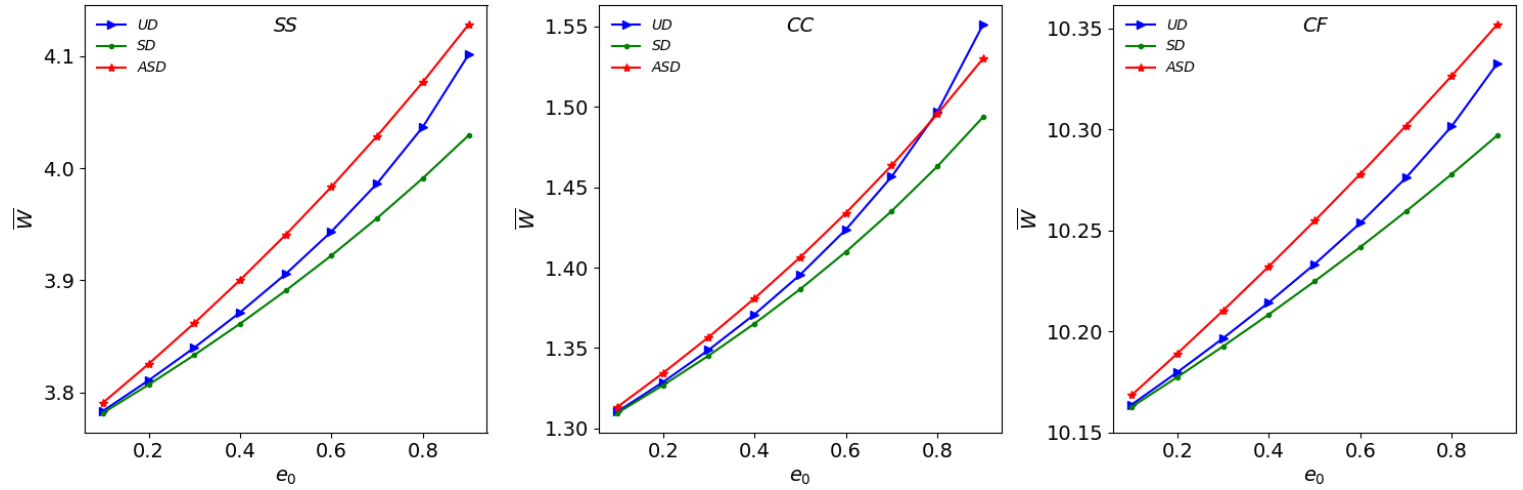

Figure 29. Porosity coefficient effect on the maximum vertical displacement of Type C beams (1-2-1, $L/h = 10$, $p = 2$, $K_w = 100$,$K_p = 10$)

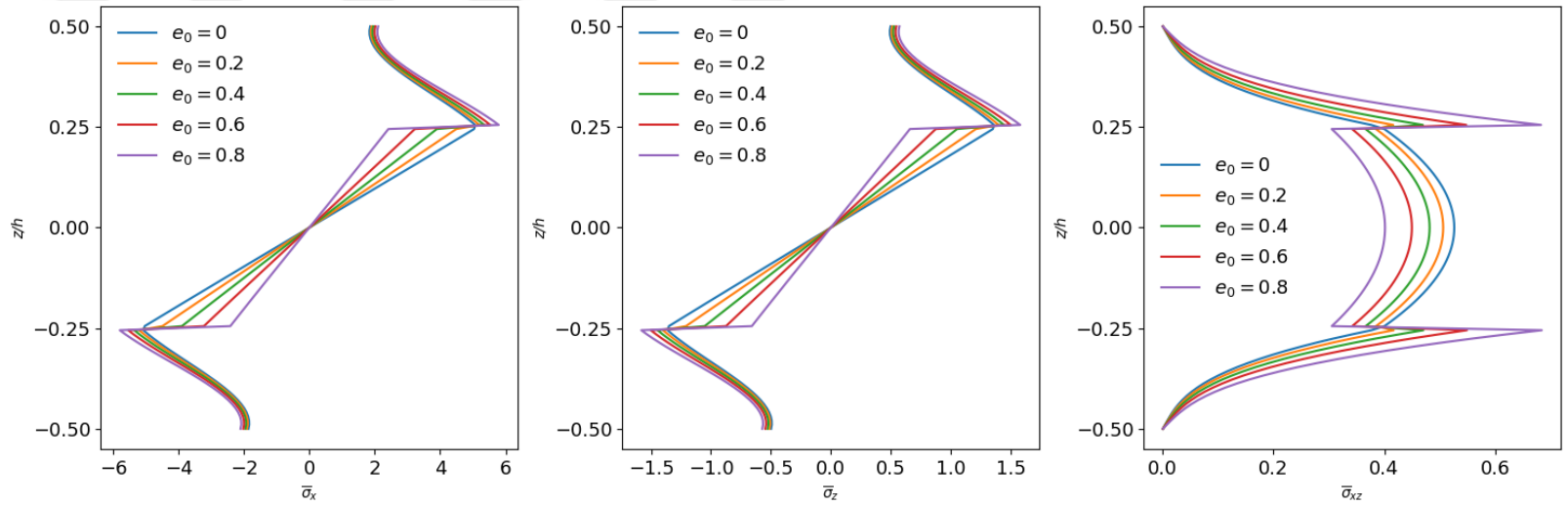

(a) UD

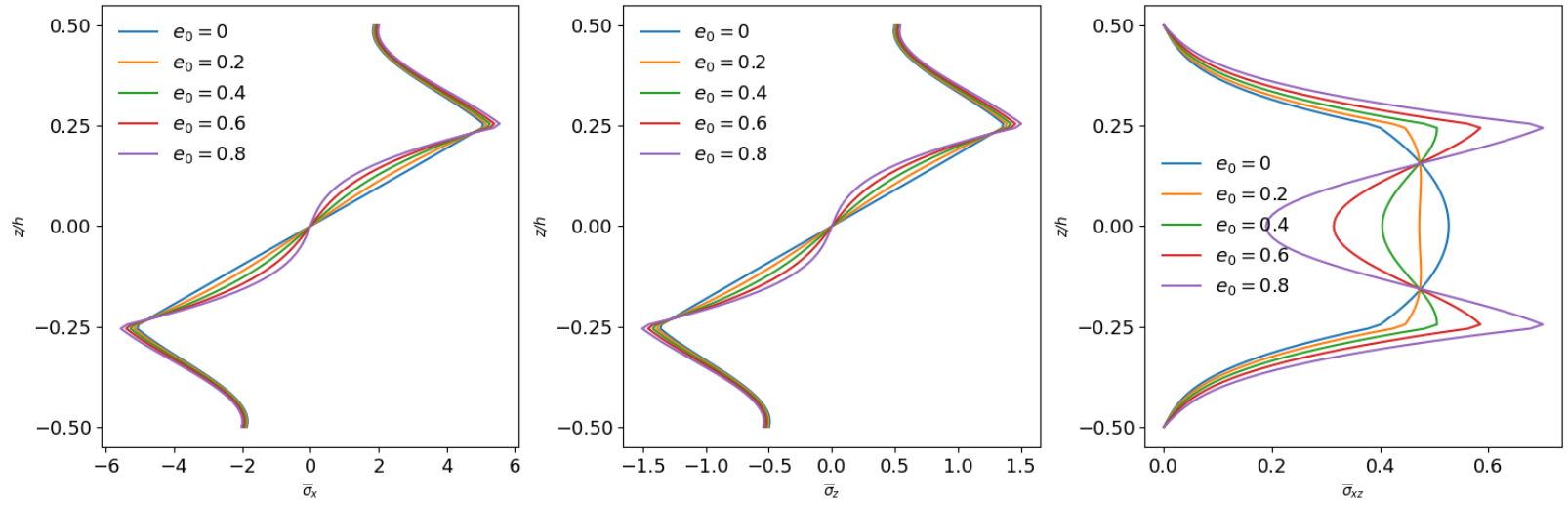

(b) SD

Figure 30. The distribution stresses along z/h of SS Type A with various porosity distributions (1-2-1, L/h = 10, p = 2, K_w = 100 ,K_p = 10)

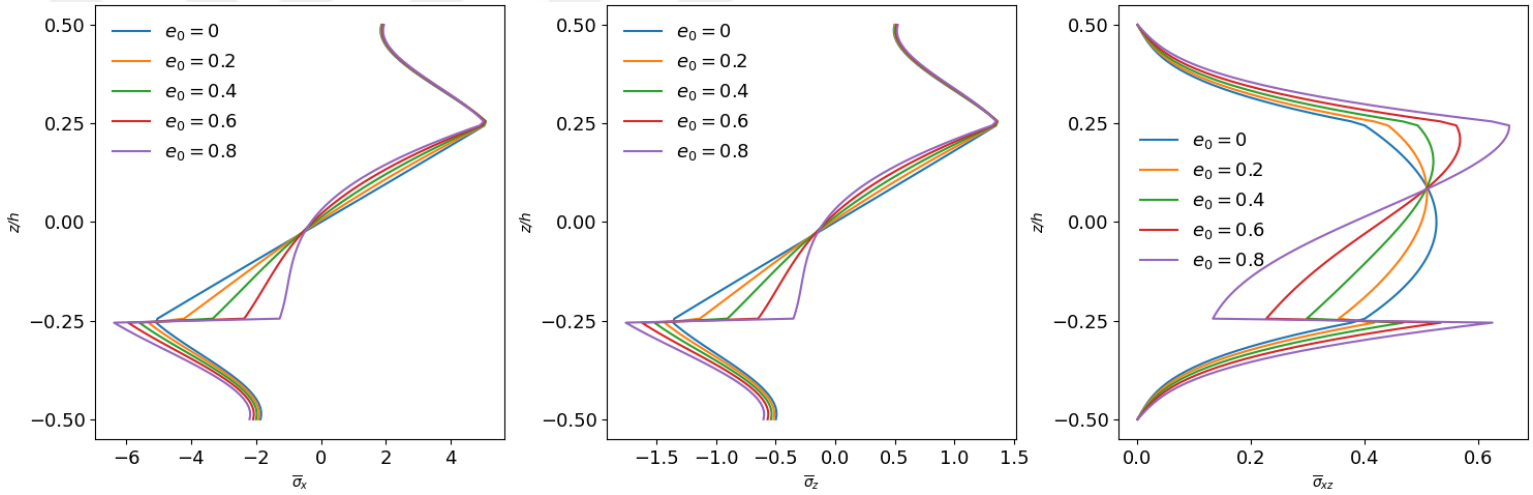

(c) ASD

Figures 30. Continued

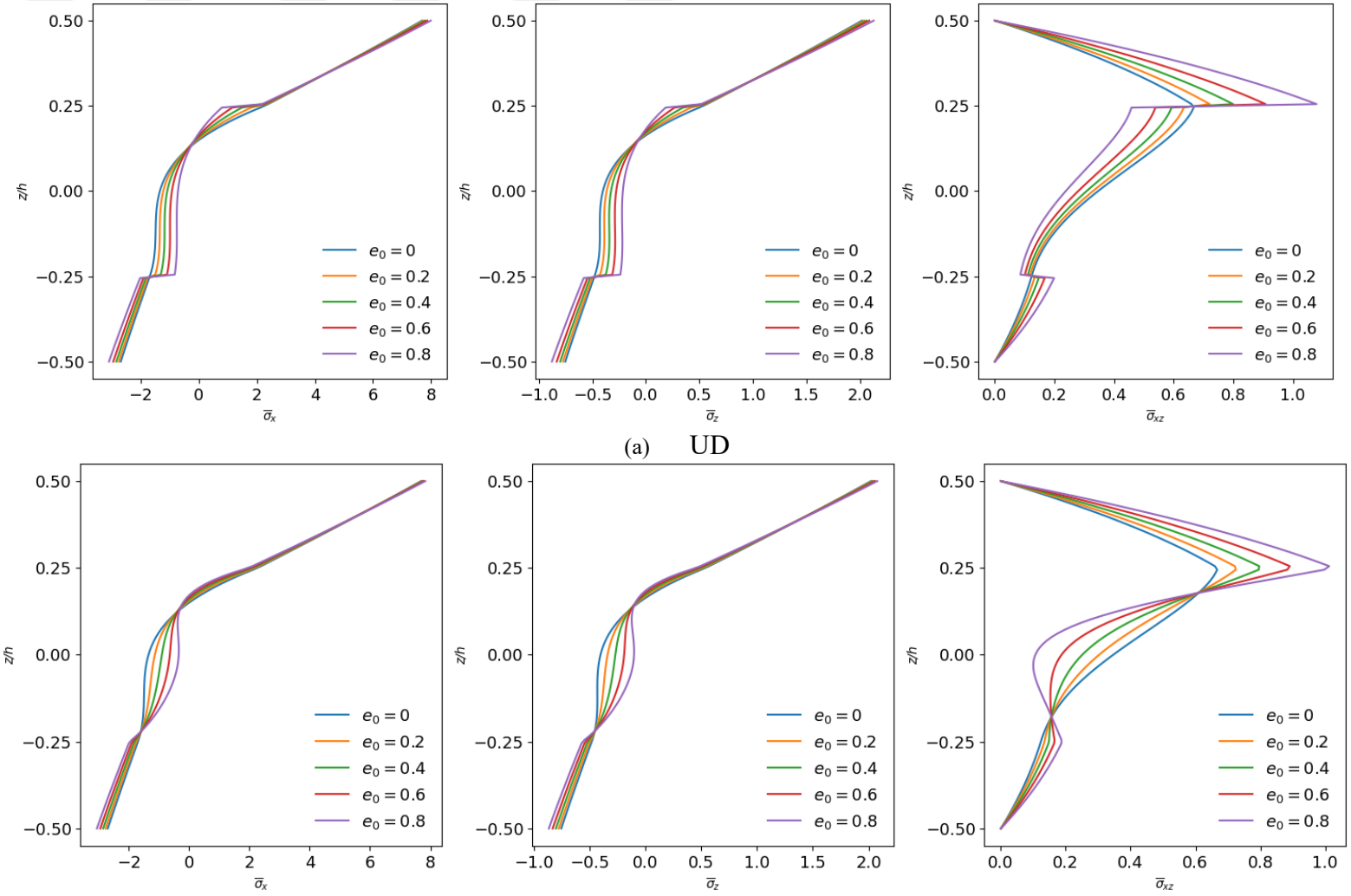

(a) UD

(b) SD

Figure 31. The distribution stresses along z/h of SS Type B with various porosity distributions (1-2-1, $L/h = 10$, $p = 2$, $K_w = 100$,$K_p = 10$)

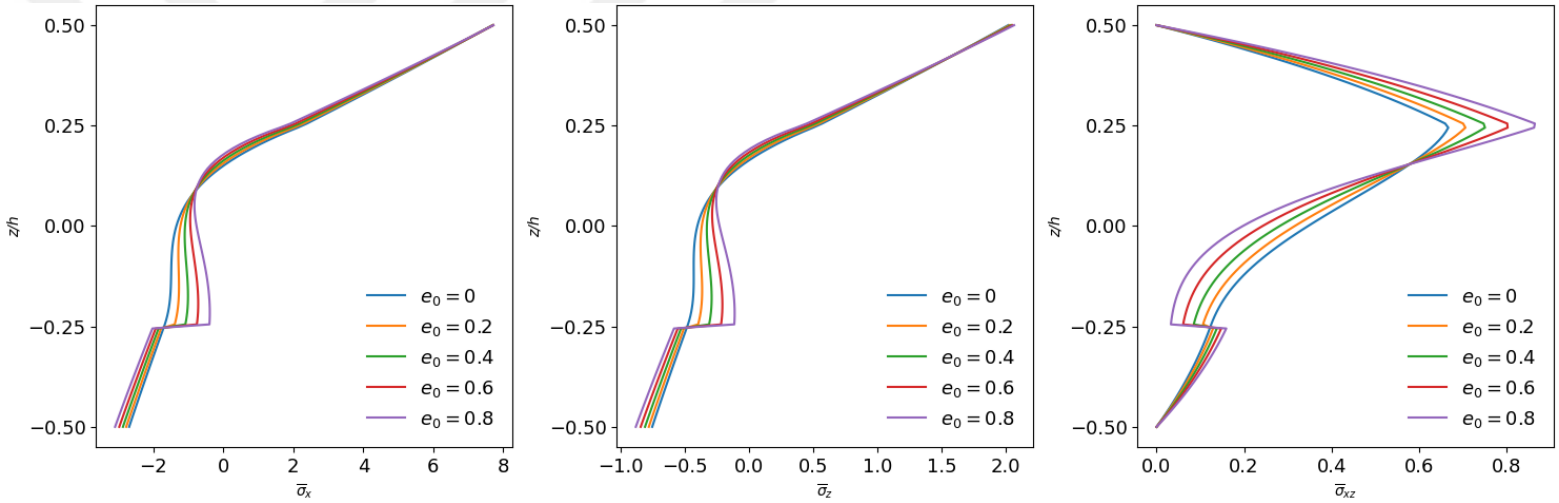

(c) ASD

Figures 31. Continued

Table 46. Maximum vertical displacement of Type A beams with different skin-core-skin thickness ratios, BCs, and porosity distributions ($p = 5$, $K_w = 25$, $K_p = 10$)

L/h	Scheme	BCs	UD			SD			ASD		
			0.4	0.6	0.8	0.4	0.6	0.8	0.4	0.6	0.8
5	2-1-2	SS	6.3394	6.3673	6.4025	6.3263	6.3448	6.3654	6.3358	6.3595	6.3857
		CC	2.3728	2.4159	2.4746	2.3647	2.3990	2.4391	2.3690	2.4055	2.4479
		CF	21.5254	21.5684	21.6237	21.5079	21.5378	21.5714	21.5201	21.5567	21.5976
	1-1-1	SS	5.9375	6.0187	6.1201	5.8872	5.9347	5.9876	5.9262	5.9973	6.0775
		CC	2.1479	2.2266	2.3379	2.1241	2.1822	2.2538	2.1403	2.2078	2.2894
		CF	20.9789	21.0990	21.2500	20.9080	20.9808	21.0627	20.9626	21.0677	21.1862
	1-2-1	SS	5.2883	5.4829	5.7303	5.1599	5.2648	5.3833	5.2636	5.4397	5.6498
		CC	1.8370	1.9693	2.1623	1.7877	1.8795	1.9984	1.8247	1.9411	2.0897
		CF	20.0096	20.3178	20.6996	19.8022	19.9741	20.1663	19.9698	20.2498	20.5748
20	2-1-2	SS	6.2694	6.2862	6.3056	6.2562	6.2648	6.2734	6.2664	6.2807	6.2957
		CC	2.0711	2.0822	2.0957	2.0639	2.0703	2.0771	2.0693	2.0788	2.0890
		CF	21.2717	21.2946	21.3213	21.2547	21.2668	21.2794	21.2677	21.2873	21.3079
	1-1-1	SS	5.8592	5.9256	6.0032	5.8063	5.8388	5.8720	5.8485	5.9070	5.9711
		CC	1.8575	1.8935	1.9373	1.8315	1.8500	1.8698	1.8521	1.8836	1.9190
		CF	20.7244	20.8173	20.9250	20.6511	20.6978	20.7455	20.7095	20.7916	20.8807
	1-2-1	SS	5.1885	5.3664	5.5844	5.0512	5.1338	5.2199	5.1635	5.3256	5.5172
		CC	1.5450	1.6272	1.7334	1.4864	1.5252	1.5675	1.5341	1.6084	1.6996
		CF	19.7366	20.0131	20.3397	19.5179	19.6521	19.7898	19.6973	19.9511	20.2409

Table 47. Maximum vertical displacement of Type C beams with different skin-core-skin thickness ratios, BCs, and porosity distributions ($p = 5$, $K_w = 25$, $K_p = 10$)

L/h	Scheme	BCs	UD			SD			ASD		
			0.4	0.6	0.8	0.4	0.6	0.8	0.4	0.6	0.8
5	2-1-2	SS	4.9014	4.9330	4.9708	4.8941	4.9185	4.9439	4.8986	4.9253	4.9528
		CC	1.7379	1.7620	1.7911	1.7311	1.7490	1.7676	1.7302	1.7474	1.7652
		CF	19.3178	19.3720	19.4365	19.3052	19.3472	19.3906	19.3134	19.3594	19.4067
	1-1-1	SS	5.0025	5.0649	5.1426	4.9888	5.0370	5.0885	5.0100	5.0695	5.1326
		CC	1.8423	1.8937	1.9597	1.8294	1.8676	1.9091	1.8310	1.8693	1.9104
		CF	19.4891	19.5948	19.7248	19.4656	19.5474	19.6340	19.5030	19.6039	19.7099
	1-2-1	SS	5.1427	5.2642	5.4230	5.1119	5.2032	5.3051	5.1722	5.2978	5.4368
		CC	1.9975	2.1036	2.2524	1.9753	2.0549	2.1476	1.9826	2.0640	2.1561
		CF	19.7258	19.9280	20.1876	19.6725	19.8248	19.9925	19.7763	19.9841	20.2093
20	2-1-2	SS	4.7254	4.7513	4.7821	4.7202	4.7406	4.7618	4.7267	4.7505	4.7751
		CC	1.3587	1.3699	1.3835	1.3563	1.3651	1.3743	1.3587	1.3688	1.3792
		CF	18.9837	19.0288	19.0822	18.9744	19.0102	19.0470	18.9858	19.0273	19.0699
	1-1-1	SS	4.7912	4.8408	4.9016	4.7813	4.8204	4.8618	4.8084	4.8623	4.9196
		CC	1.3900	1.4122	1.4398	1.3854	1.4027	1.4213	1.3959	1.4191	1.4439
		CF	19.0982	19.1832	19.2863	19.0810	19.1483	19.2190	19.1276	19.2196	19.3161
	1-2-1	SS	4.8788	4.9740	5.0944	4.8513	4.9221	4.9996	4.9275	5.0440	5.1735
		CC	1.4332	1.4771	1.5346	1.4212	1.4537	1.4901	1.4513	1.5025	1.5608
		CF	19.2480	19.4075	19.6051	19.2013	19.3211	19.4503	19.3296	19.5220	19.7305

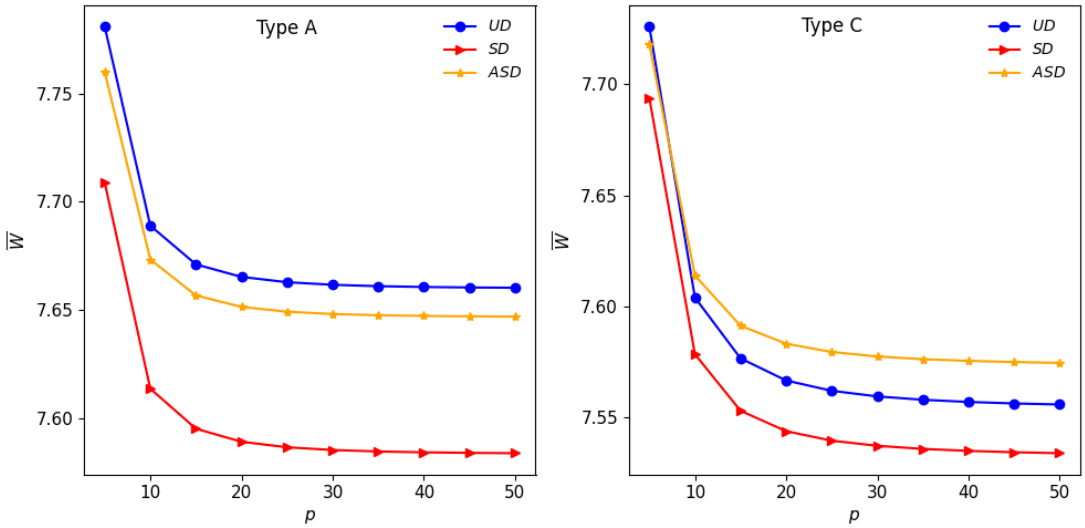

Figure 32. Effect of length-to-thickness ratio on maximum vertical displacement in CF beams across different porosity distributions (1-2-1, e_0 = 0.8, K_w = 100, K_p = 25, p = 5)

3.5.5. Elastic Foundation Effect

The numerical results showcasing the influence of foundation parameters and porosity patterns on maximum vertical displacement and stresses are tabulated in Tables 48 and 49. Increasing foundation parameters uniformly reduces maximum vertical displacement and stresses across all porosity distributions. This enhancement in beam performance is attributed to the boosted bending stiffness provided by the elastic foundation. To assess the impact of Winkler and Pasternak parameters, Figure 33 depicts the maximum vertical displacement variation of Type A beams as a function of K_w and K_p. It deserves to be pointed out that a significant reduction in maximum vertical displacements for FGSBs is observed with increasing foundation parameters, with the Pasternak parameter exerting a more pronounced effect. Furthermore, porosity distributions have minimal impact on CF beams due to the dominant effect of the elastic foundation on bending stiffness. Similarly, Figures 34-36 graphically depict the stress distribution within the thickness of SS Type A beams with respect to K_w and K_p. A consistent reduction in nondimensional axial, vertical, and shear stresses is observed for all porosity distribution patterns as foundation parameters increase, especially with increasing Pasternak parameters. This can be attributed to the strengthened shear interaction between the shear layer and the beam, leading to improved overall stability and stiffness. Therefore, it can be conclusively stated that the Pasternak parameter is more influential than the Winkler parameter in altering the static behavior of FGSBs.

Table 48. Effect of foundation parameters on maximum vertical displacement of FGSBs (1-2-1, $L/h = 5$, $p = 5$, $e_0 = 0.5$)

Type	K_p	BCs	K_w								
			UD			SD			USD		
			0	50	100	0	50	100	0	50	100
Type A	0	SS	9.6704	7.3153	5.8788	9.1348	7.0043	5.6763	9.5639	7.2543	5.8395
		CC	2.2991	2.1377	1.9971	2.2000	2.0517	1.9218	2.2719	2.1142	1.9766
		CF	90.1802	25.4439	14.4665	84.9819	25.0307	14.3526	89.2069	25.3718	14.4484
	10	SS	5.9131	4.9364	4.2347	5.7083	4.7928	4.1288	5.8733	4.9087	4.2145
		CC	1.9597	1.8406	1.7350	1.8881	1.7772	1.6785	1.9398	1.8231	1.7194
		CF	28.7861	15.4406	10.4300	28.2042	15.2920	10.3748	28.6717	15.4125	10.4202
	25	SS	3.7294	3.3133	2.9800	3.6470	3.2482	2.9273	3.7137	3.3010	2.9701
		CC	1.6073	1.5259	1.4521	1.5596	1.4827	1.4130	1.5939	1.5138	1.4411
		CF	15.0635	10.2248	7.6957	14.8773	10.1488	7.6591	15.0230	10.2084	7.6879
Type C	0	SS	9.1064	6.9860	5.6624	8.9715	6.9066	5.6104	9.2048	7.0448	5.7018
		CC	2.5131	2.3194	2.1530	2.4635	2.2772	2.1166	2.4773	2.2892	2.1272
		CF	81.9713	24.6044	14.1376	80.8469	24.5142	14.1166	83.3542	24.7442	14.1891
	10	SS	5.6965	4.7833	4.1206	5.6437	4.7462	4.0932	5.7359	4.8117	4.1420
		CC	2.1201	1.9800	1.8569	2.0843	1.9488	1.8295	2.0933	1.9568	1.8366
		CF	28.1745	15.2212	10.3075	28.0106	15.1813	10.2941	28.2813	15.2563	10.3255
	25	SS	3.6417	3.2434	2.9228	3.6203	3.2265	2.9092	3.6585	3.2570	2.9340
		CC	1.7211	1.6271	1.5426	1.6970	1.6056	1.5233	1.7020	1.6102	1.5275
		CF	15.0119	10.1867	7.6650	14.9481	10.1610	7.6528	15.0198	10.1914	7.6682

Table 49. Effect of foundation parameters on maximum stresses of SS beams (1-2-1, L/h = 5, p = 5, e_0 = 0.5)

Type	K_p	Stress	K_w								
			UD			SD			USD		
			0	50	100	0	50	100	0	50	100
Type A	0	$\bar{\sigma}_x$	2.2377	1.6827	1.3443	2.1071	1.6065	1.2946	2.1205	1.5989	1.2795
		$\bar{\sigma}_z$	0.0809	0.0743	0.0703	0.6238	0.5030	0.4276	0.7831	0.6261	0.5298
		$\bar{\sigma}_{xz}$	0.8162	0.6512	0.5504	0.6238	0.5030	0.4276	0.7831	0.6261	0.5298
	10	$\bar{\sigma}_x$	1.3576	1.1276	0.9625	1.3069	1.0920	0.9362	1.2920	1.0743	0.9177
		$\bar{\sigma}_z$	0.0709	0.0682	0.0663	0.0677	0.0650	0.0631	0.0559	0.0556	0.0553
		$\bar{\sigma}_{xz}$	0.5441	0.4754	0.4260	0.4229	0.3709	0.3331	0.5238	0.4581	0.4107
	25	$\bar{\sigma}_x$	0.8498	0.7519	0.6736	0.8288	0.7353	0.6601	0.8107	0.7176	0.6431
		$\bar{\sigma}_z$	0.0655	0.0643	0.0634	0.0622	0.0611	0.0602	0.0557	0.0555	0.0554
		$\bar{\sigma}_{xz}$	0.3796	0.3502	0.3266	0.2975	0.2747	0.2563	0.3661	0.3379	0.3151
Type C	0	$\bar{\sigma}_x$	7.9023	5.7503	4.4992	7.2368	5.3445	4.2185	7.6549	5.5261	4.3028
		$\bar{\sigma}_z$	0.1478	0.1515	0.1539	0.1571	0.1578	0.1584	0.1942	0.1864	0.1815
		$\bar{\sigma}_{xz}$	0.3455	0.2784	0.2364	0.2522	0.2038	0.1733	0.3116	0.2506	0.2126
	10	$\bar{\sigma}_x$	4.5618	3.7354	3.1542	4.2762	3.5220	2.9864	4.3629	3.5604	2.9987
		$\bar{\sigma}_z$	0.1557	0.1573	0.1585	0.1602	0.1606	0.1609	0.1835	0.1802	0.1778
		$\bar{\sigma}_{xz}$	0.2329	0.2039	0.1828	0.1708	0.1497	0.1343	0.2096	0.1834	0.1644
	25	$\bar{\sigma}_x$	2.7766	2.4408	2.1744	2.6363	2.3230	2.0735	2.6349	2.3123	2.0569
		$\bar{\sigma}_z$	0.1615	0.1623	0.1629	0.1632	0.1634	0.1636	0.1782	0.1768	0.1757
		$\bar{\sigma}_{xz}$	0.1620	0.1493	0.1391	0.1191	0.1098	0.1023	0.1458	0.1344	0.1252

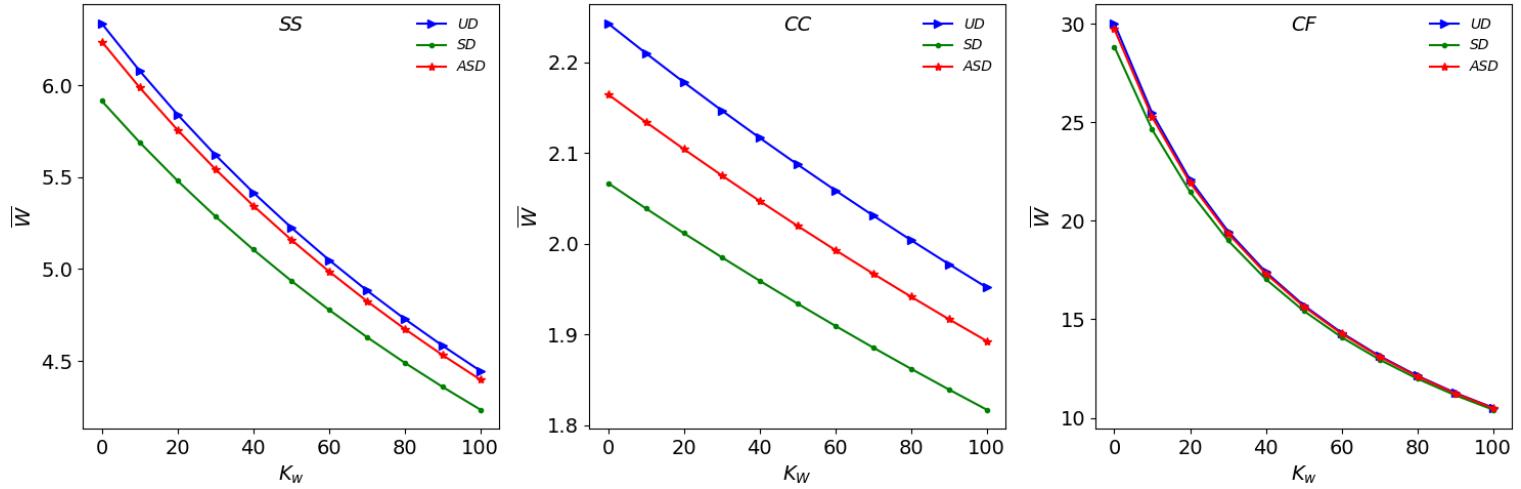

(a) when $K_p = 10$

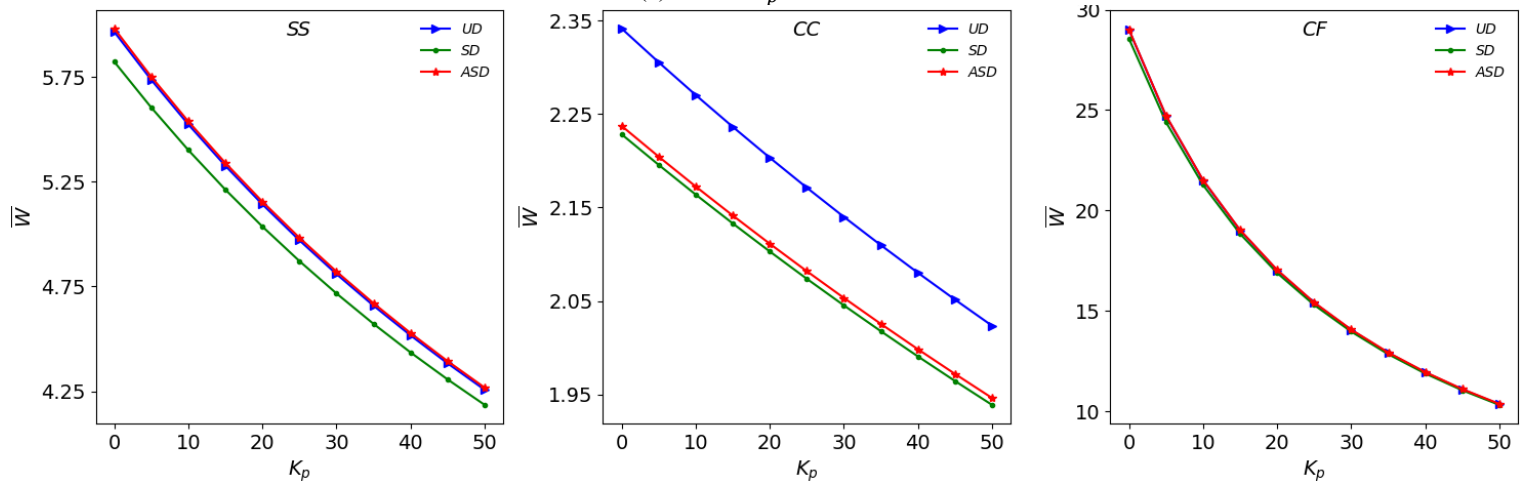

(b) when $K_w = 100$

Figure 33. Effect of K_w and K_p maximum vertical displacement of Type A beam with different BCs and porosity distributions (1-2-1, $L/h = 5$, $p = 5$, $e_0 = 0.8$)

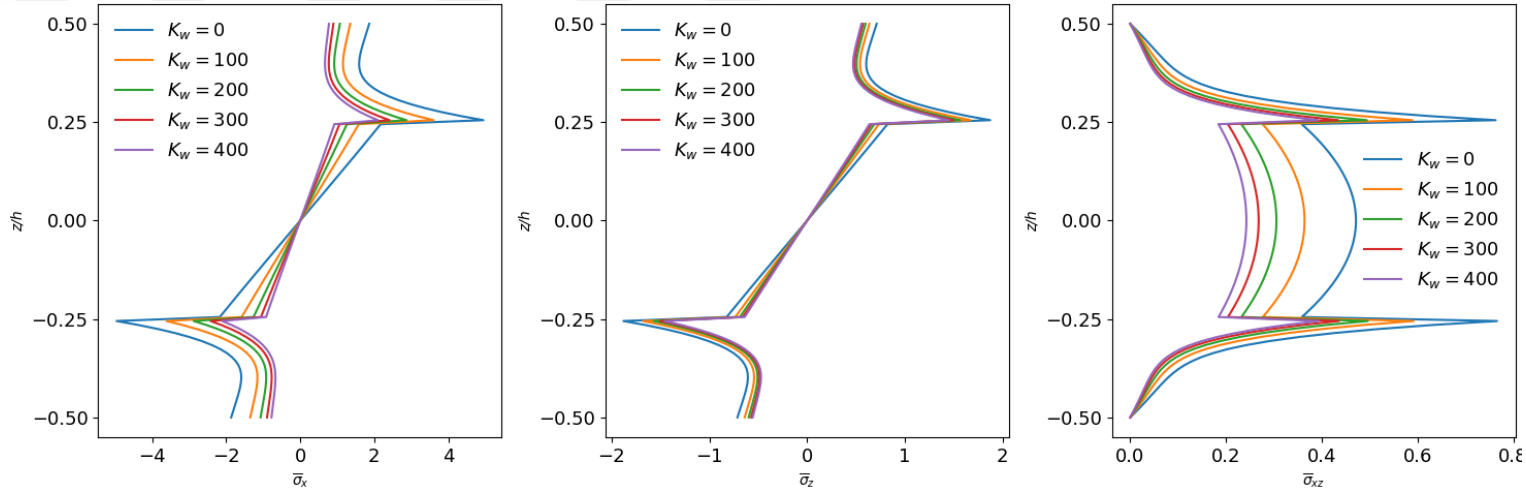

(a) when $K_p = 10$

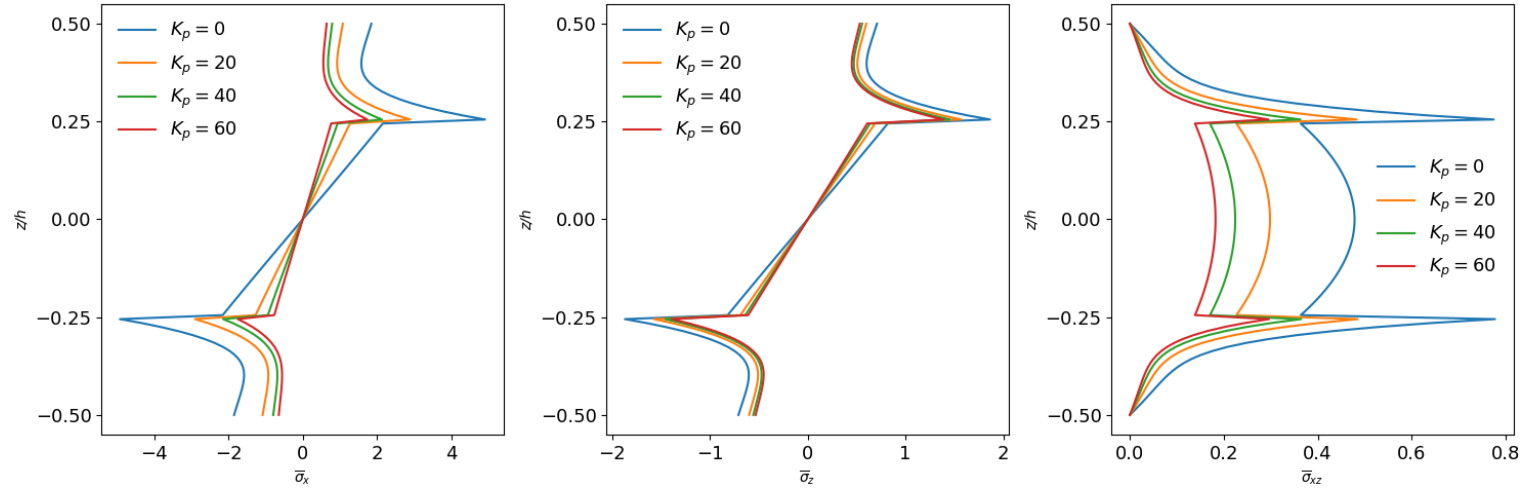

(b) when $K_w = 100$

Figure 34. Effect of K_w and K_p stress distributions along z/h of SS Type A beam with UD (1-2-1,L/h = 5, p = 5, e_0 = 0.8)

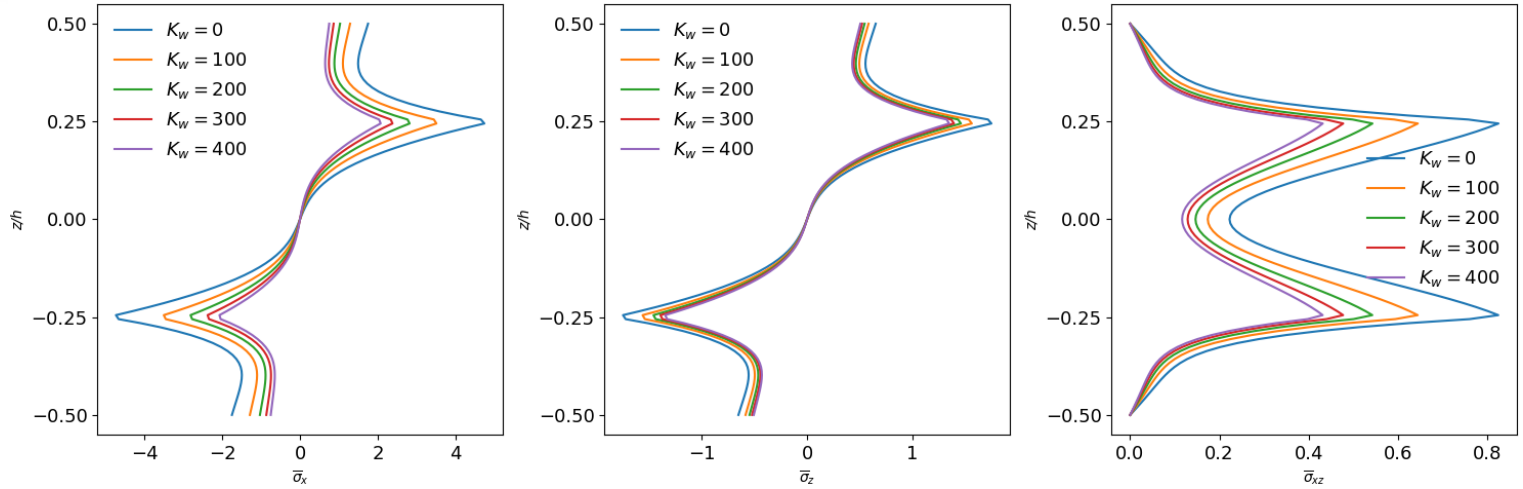

(a) when $K_p = 10$

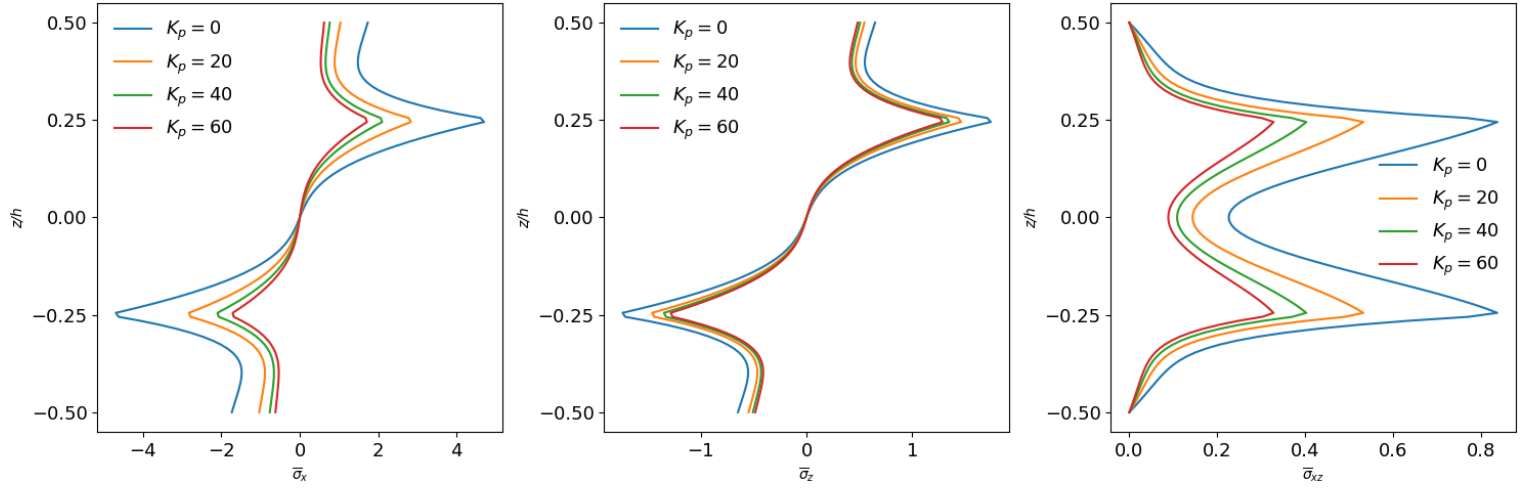

(b) when $K_w = 100$

Figure 35. Effect of K_w and K_p stress distributions along z/h of SS Type A beams with SD (1-2-1,L/h = 5, p = 5, e_0 = 0.8)

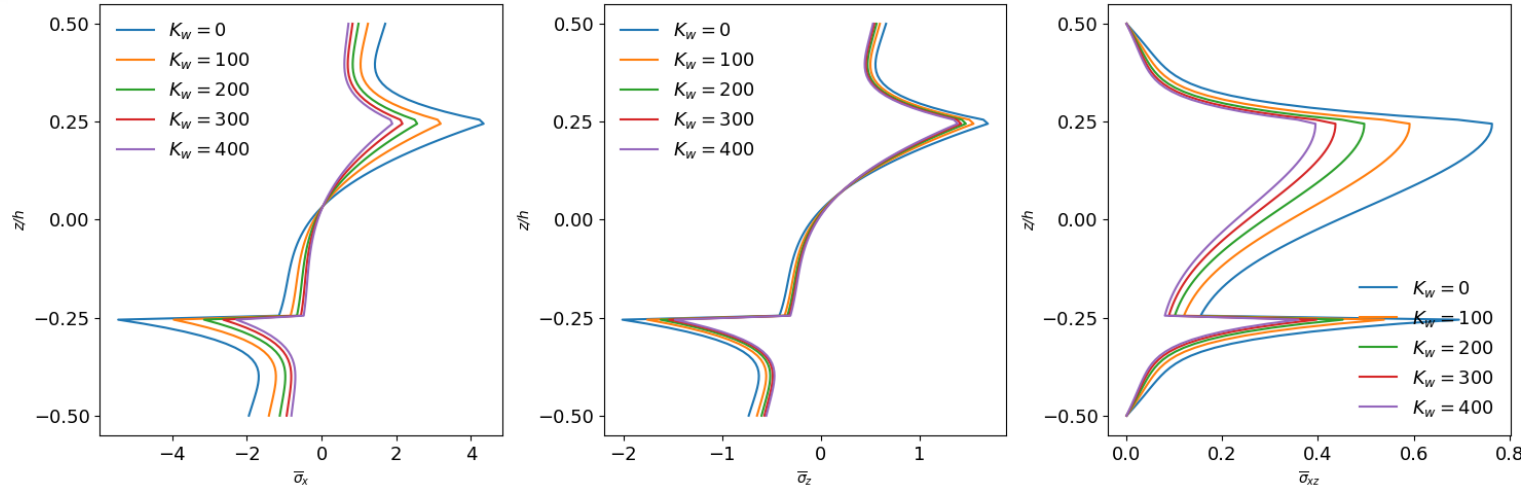

(a) when $K_p = 10$

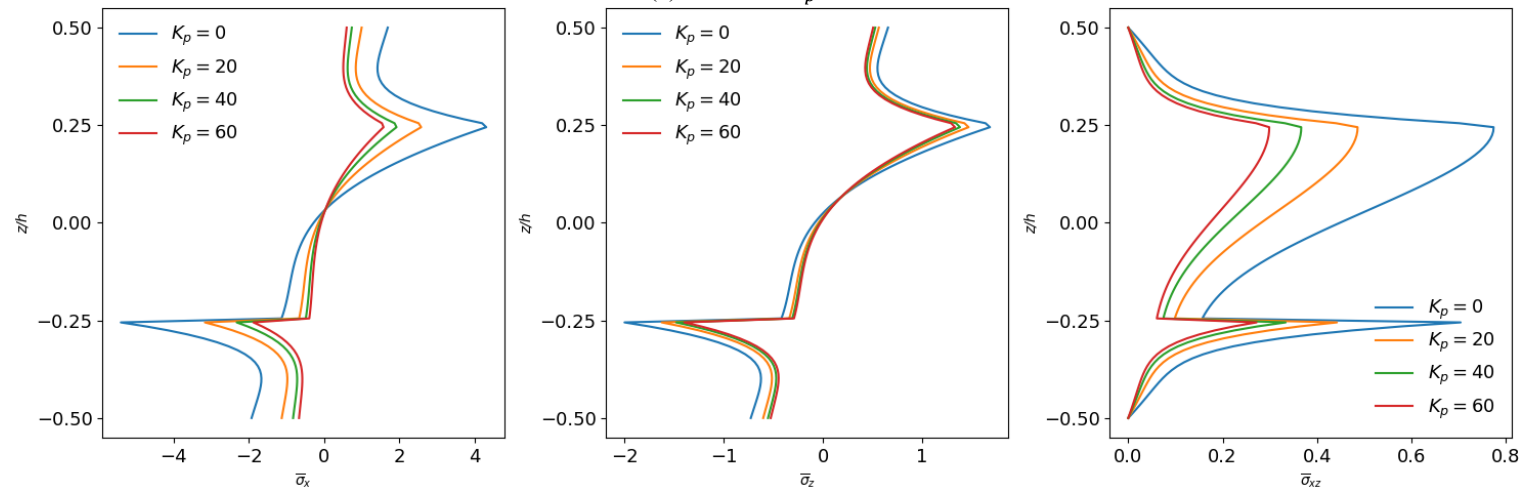

(b) when $K_w = 100$

Figure 36. Effect of K_w and K_p stress distributions along z/h of SS Type A beams with ASD (1-2-1,L/h = 5, p = 5, e_0 = 0.8)

3.6. Computational Modelling of FGSBs with Porous Core Using Ansys APDL

3.6.1. Convergence and Validation Study

The proposed approach is validated by comparing results for non-porous Type A beams with the FE model and the available studies. Tables 50-52 compare nondimensional displacements, buckling loads, and frequencies with FEM results and previous studies using HSDT (Vo et al., 2014, 2015b) and quasi-3D theories (Nguyen et al., 2016; Vo et al., 2015a) The presented approach yields highly accurate results, with less than 1% difference from analytical results across power-index values. This difference is lower for CF beams than CC beams and decreases with increasing the length-to-thickness ratio. Therefore, the new approach proves to be suitable and reliable for studying the mechanical behavior of FGSBs.

To evaluate the accuracy and reliability of the proposed modeling technique, Tables 53 and 54 present a comparison of fundamental natural frequencies derived from both the proposed approach and an FE model for diverse FGSB configurations including 1-0-1, 2-1-2, 1-1-1, and 1-2-1 ratios. The strong correlation between the obtained results provides compelling evidence for the accuracy and robustness of the proposed modeling technique, thus establishing its suitability for diverse FGSB designs.

Table 50. Nondimensional maximum vertical displacements of Type A beams (1-2-1)

L/h	BC	Theory	p				
			0	1	2	5	10
5	CF	ANSYS	28.6720	49.7280	62.6080	79.4080	88.0320
		Quasi-3D-FEM	28.5532	49.7415	62.4630	79.0683	87.4969
		HSDT[4]	28.7555	50.0741	62.8813	79.6213	88.1270
		Quasi-3D[3]	28.5524	49.7281	62.4386	79.0288	87.4501
	CC	ANSYS	0.8366	1.3104	1.5904	1.9488	2.1392
		Quasi-3D-FEM	0.8323	1.3072	1.5852	1.9417	2.1212
		HSDT[4]	0.8501	1.3372	1.6225	1.9896	2.1747
		Quasi-3D[3]	0.8327	1.3077	1.5853	1.9416	2.1211
20	CF	ANSYS	27.6063	48.5625	61.2500	77.8750	86.6250
		Quasi-3D-FEM	27.6219	48.6886	61.3682	77.9597	86.3942
		HSDT[4]	27.7029	48.8489	61.5809	78.2451	86.7178
		Quasi-3D[3]	27.6217	48.6985	61.3855	77.9869	86.4264
	CC	ANSYS	0.5906	1.0281	1.2906	1.6406	1.8200
		Quasi-3D-FEM	0.5893	1.0294	1.2938	1.6394	1.8149
		HSDT[4]	0.5933	1.0365	1.3028	1.6512	1.8282
		Quasi-3D[3]	0.5894	1.0293	1.2936	1.6390	1.8145

HSDT[3] (Sayyad and Avhad, 2019), HSDT[4] (Vo et al., 2015b), Quasi-3D[3] (Vo et al., 2015b)

Table 51. Nondimensional critical buckling loads of Type A beams (1-2-1)

L/h	BCs	Theory	p				
			0	1	2	5	10
5	CF	ANSYS	13.1574	7.5137	5.9550	4.6770	4.2642
		Quasi-3D-FEM	13.1120	7.4938	5.9593	4.7023	4.2475
		HSDT[1]	13.0595	7.4638	5.9347	4.6806	4.2268
		Quasi-3D[1]	13.1138	7.4948	5.9601	4.7028	4.2480
		Quasi-3D[2]	13.1224	7.5028	5.9674	4.7088	4.2533
20	CF	ANSYS	13.4112	7.6149	6.0311	4.7394	4.2649
		Quasi-3D-FEM	13.3958	7.5961	6.0256	4.7424	4.2791
		HSDT[1]	13.3730	7.5815	6.0134	4.7323	4.2698
		Quasi-3D[1]	13.3993	7.5986	6.0278	4.7443	4.2809
		Quasi-3D[2]	13.3981	7.5965	6.0257	4.7423	4.2789

HSDT[1] (Vo et al., 2014); Quasi-3D[1] (Nguyen et al., 2016); Quasi-3D[2] (Vo et al., 2015a)

Table 52. Nondimensional fundamental natural frequencies of Type A beams (1-2-1)

L/h	BCs	Theory	p				
			0	1	2	5	10
5	CF	ANSYS	1.9074	1.5139	1.3706	1.2349	1.1817
		Quasi-3D-FEM	1.9053	1.5094	1.3677	1.2346	1.1820
		HSDT[1]	1.8953	1.4993	1.3582	1.2258	1.1734
		Quasi-3D[1]	1.9053	1.5071	1.3653	1.2323	1.1798
		Quasi-3D[2]	1.9055	1.5075	1.3658	1.2329	1.1804
	CC	ANSYS	10.1700	8.4912	7.8212	7.1521	6.8639
		Quasi-3D-FEM	10.1748	8.4729	7.8087	7.1531	6.8915
		HSDT[1]	10.0726	8.3747	7.7149	7.0723	6.8119
		Quasi-3D[1]	10.1790	8.4653	7.8008	7.1550	6.8934
		Quasi-3D[2]	10.1851	8.4752	7.8114	7.1652	6.9030
20	CF	ANSYS	1.9540	1.5351	1.3865	1.2479	1.1927
		Quasi-3D-FEM	1.9548	1.5347	1.3872	1.2494	1.1952
		HSDT[1]	1.9496	1.5304	1.3831	1.2456	1.1915
		Quasi-3D[1]	1.9530	1.5335	1.3860	1.2484	1.1943
		Quasi-3D[2]	1.9527	1.5329	1.3855	1.2478	1.1937
	CC	ANSYS	12.2798	9.6949	8.7700	7.9025	7.5553
		Quasi-3D-FEM	12.2752	9.6856	8.7679	7.9080	7.5541
		HSDT[1]	12.2243	9.6419	8.7268	7.8696	7.5315
		Quasi-3D[1]	12.2756	9.6866	8.7690	7.9092	7.5700
		Quasi-3D[2]	12.2660	9.6768	8.7593	7.9000	7.5609

HSDT[1] (Vo et al., 2014); Quasi-3D[1] (Nguyen et al., 2016); Quasi-3D[2] (Vo et al., 2015a)

To provide a comprehensive comparison, Table 55 presents the first three natural frequencies of the beams. The results obtained from Ansys simulations and quasi-3D-FEM exhibit excellent agreement across various modes and BCs. The negligible differences

between the results strongly support the accuracy and reliability of the proposed modeling technique in determining the natural frequencies of FGSBs.

Table 53. Comparison of fundamental natural frequencies of CF Type A beams

L/h	Scheme	Theory	p				
			0	1	2	5	10
5	1-0-1	ANSYS	1.9114	1.3152	1.1250	1.0048	0.9875
		Quasi-3D-FEM	1.9073	1.3097	1.1222	1.0043	0.9878
	2-1-2	ANSYS	1.9114	1.3717	1.1861	1.0388	0.9971
		Quasi-3D-FEM	1.9073	1.3670	1.1831	1.0380	0.9983
	1-1-1	ANSYS	1.9114	1.4248	1.2535	1.1028	1.0500
		Quasi-3D-FEM	1.9073	1.4212	1.2505	1.1017	1.0510
	1-2-1	ANSYS	1.9114	1.5139	1.3706	1.2349	1.1817
		Quasi-3D-FEM	1.9073	1.5094	1.3677	1.2346	1.1820
20	1-0-1	ANSYS	1.9540	1.3313	1.1371	1.0179	1.0038
		Quasi-3D-FEM	1.9548	1.3291	1.1364	1.0175	1.0033
	2-1-2	ANSYS	1.9540	1.3883	1.1976	1.0487	1.0082
		Quasi-3D-FEM	1.9548	1.3871	1.1973	1.0486	1.0084
	1-1-1	ANSYS	1.9540	1.4428	1.2660	1.1124	1.0596
		Quasi-3D-FEM	1.9548	1.4430	1.2661	1.1130	1.0612
	1-2-1	ANSYS	1.9540	1.5351	1.3865	1.2479	1.1927
		Quasi-3D-FEM	1.9548	1.5347	1.3872	1.2494	1.1952

Table 54. Comparison of fundamental natural frequencies of CC Type A beams

L/h	Scheme	Theory	p				
			0	1	2	5	10
5	1-0-1	ANSYS	10.1700	7.4712	6.4660	5.7652	5.5809
		Quasi-3D-FEM	10.1748	7.4499	6.4852	5.7931	5.5998
	2-1-2	ANSYS	10.1700	7.7983	6.8626	6.0763	5.8414
		Quasi-3D-FEM	10.1748	7.7828	6.8711	6.1024	5.8752
	1-1-1	ANSYS	10.1700	8.0711	7.2354	6.4309	6.1747
		Quasi-3D-FEM	10.1748	8.0570	7.2298	6.4674	6.1997
	1-2-1	ANSYS	10.1700	8.4912	7.8212	7.1521	6.8639
		Quasi-3D-FEM	10.1748	8.4729	7.8087	7.1531	6.8915
20	1-0-1	ANSYS	12.2798	8.4180	7.1968	6.4335	6.3308
		Quasi-3D-FEM	12.2752	8.3986	7.1908	6.4368	6.3332
	2-1-2	ANSYS	12.2798	8.7789	7.5840	6.6413	6.3787
		Quasi-3D-FEM	12.2752	8.7651	7.5786	6.6446	6.3783
	1-1-1	ANSYS	12.2798	9.1201	8.0155	7.0487	6.7124
		Quasi-3D-FEM	12.2752	9.1147	8.0115	7.0523	6.7132
	1-2-1	ANSYS	12.2798	9.6949	8.7700	7.9025	7.5553
		Quasi-3D-FEM	12.2752	9.6856	8.7679	7.9080	7.5541

Table 55. The first three natural frequencies of Type A beams (1-2-1, $L/h = 10$, $p = 5$)

Mode	CF		CC	
	ANSYS	Quasi-3D-FEM	ANSYS	Quasi-3D-FEM
1	1.2467	1.2471	7.7454	7.7474
2	7.5557	7.6120	20.4820	20.5262
3	20.2623	20.5557	38.2038	38.3320

Visual representations in Figures 37-39 illustrate the changes in maximum vertical displacements, critical buckling loads, and fundamental natural frequencies with respect to power indices for both models. The strong correlation between the numerical and analytical results compellingly demonstrates the accuracy and suitability of the proposed technique for analyzing and designing FGSBs. Consistent with expectations, increasing, the power index leads to higher displacements but lower buckling loads and frequencies.

Figure 40 visualizes stress distribution through the thickness of the CF beam. The remarkable agreement observed between the FE model and Ansys simulation provides robust evidence for the accuracy of the formulated model. As expected, the normal stress distributions are symmetric about the beam mid-plane, with peak values at the core's upper and lower interfaces. This symmetric profile is the direct result of the material's gradual variations across the beam thickness. The shear stress distribution is also symmetric, peaking at the midplane and vanishing at the top and bottom surfaces. The observed hyperbolic stress profile results from smooth material property transitions in the FG layers.

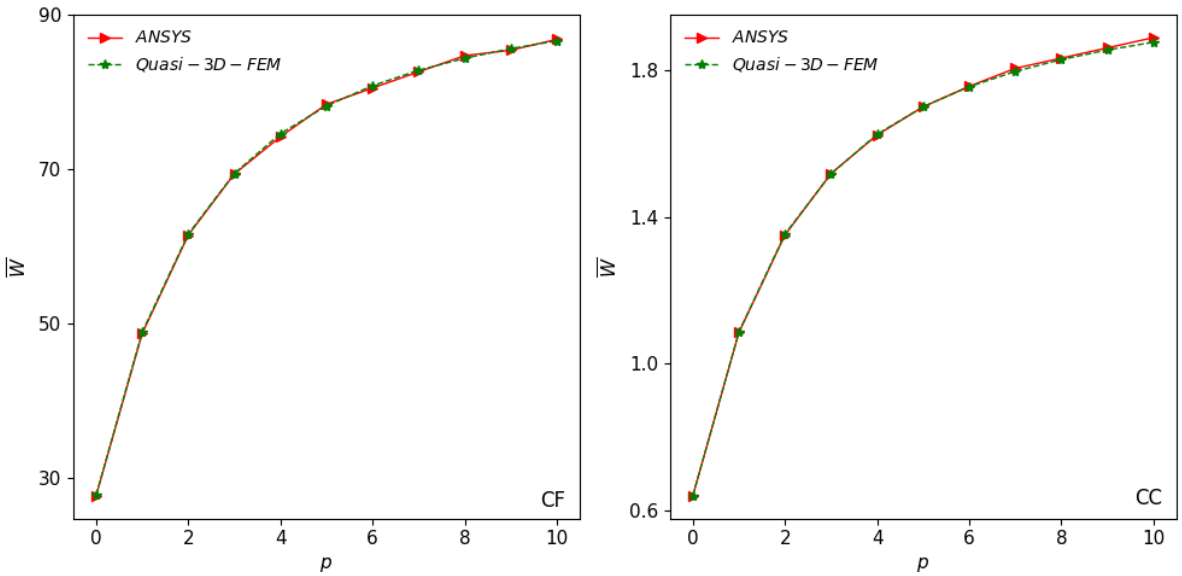

Figure 37. Maximum displacement of beams with power-index (1-2-1, $L/h = 10$)

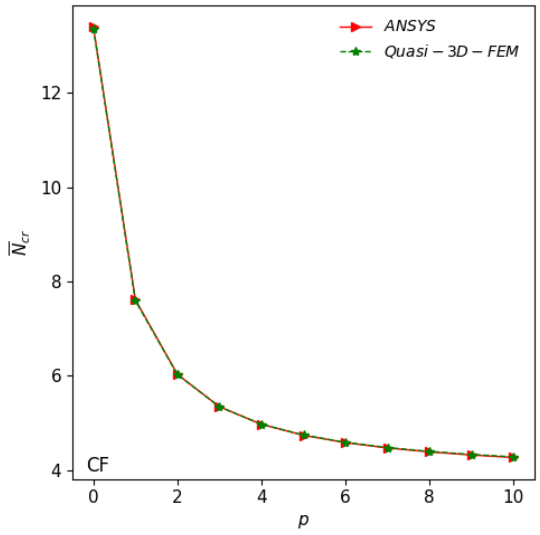

Figure 38. Critical buckling load of CF beam with power-index (1-2-1, L/h = 10)

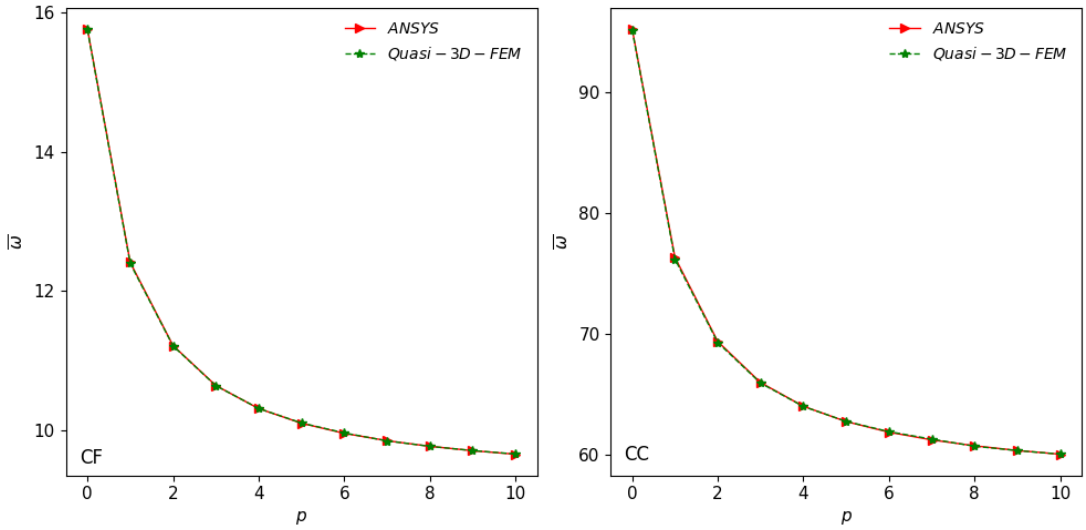

Figure 39. Fundamental natural frequencies of beams with power-index (1-2-1, L/h =10)

3.6.2. Porosity Effect

The maximum vertical displacements, critical buckling loads, and fundamental natural frequencies of Type A beams versus porosity coefficients for different porosity distributions are plotted in Figures 41-43. The observed trends align with previous findings, with increasing porosity coefficient consistently leading to higher displacements and frequencies, and lower buckling loads, for all BCs and porosity patterns. The increasing divergence between Ansys simulation and FE model results as the porosity increases can be attributed to the heightened complexity in modeling material behavior at elevated porosity levels.

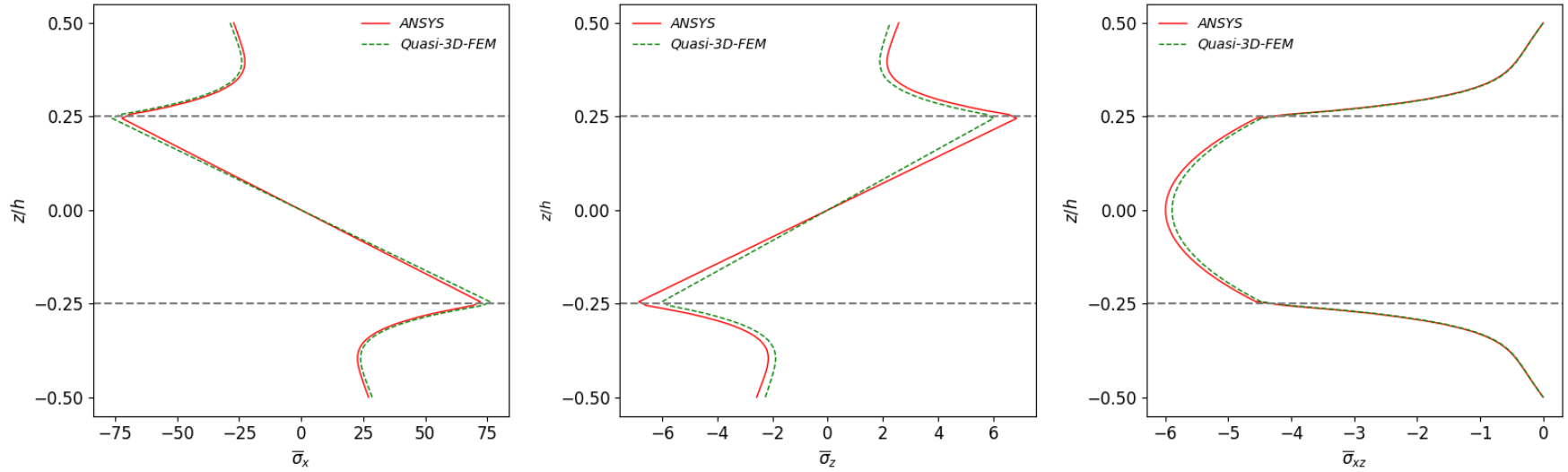

Figure 40. Stresses distribution along z/h of CF beam (1-2-1, L/h = 10, p = 5)

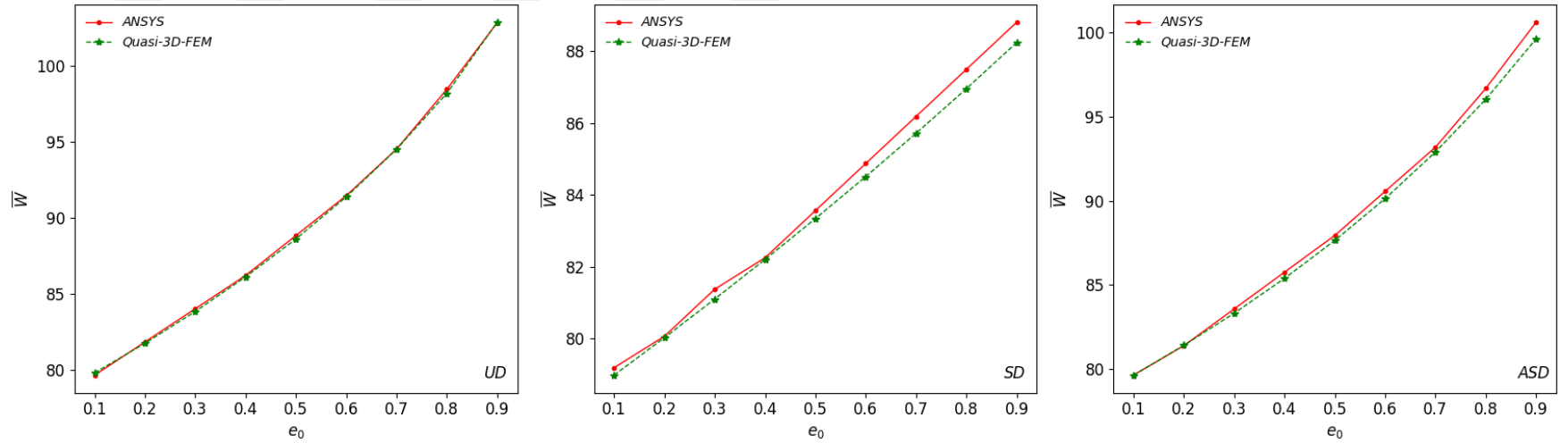

(a) CF

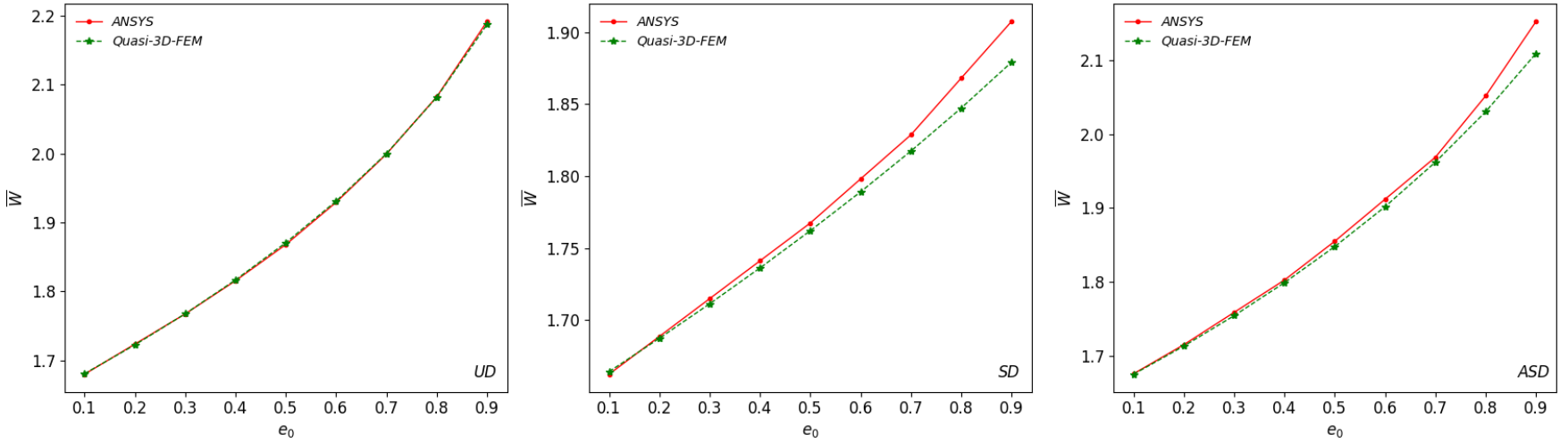

(b) CC

Figure 41. Porosity coefficient effect on maximum vertical displacement of beams with various porosity distributions (1-2-1, $L/h = 20$, $p = 5$)

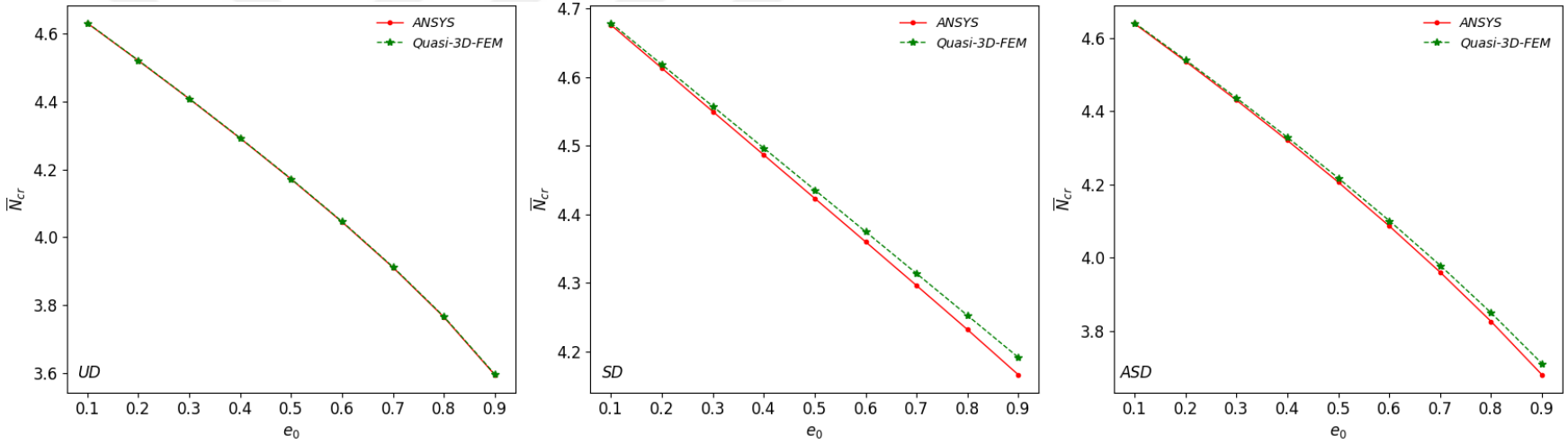

Figure 42. Porosity coefficient effect on critical buckling loads of CF beam with various porosity distributions (1-2-1, $L/h = 20$, $p = 5$)

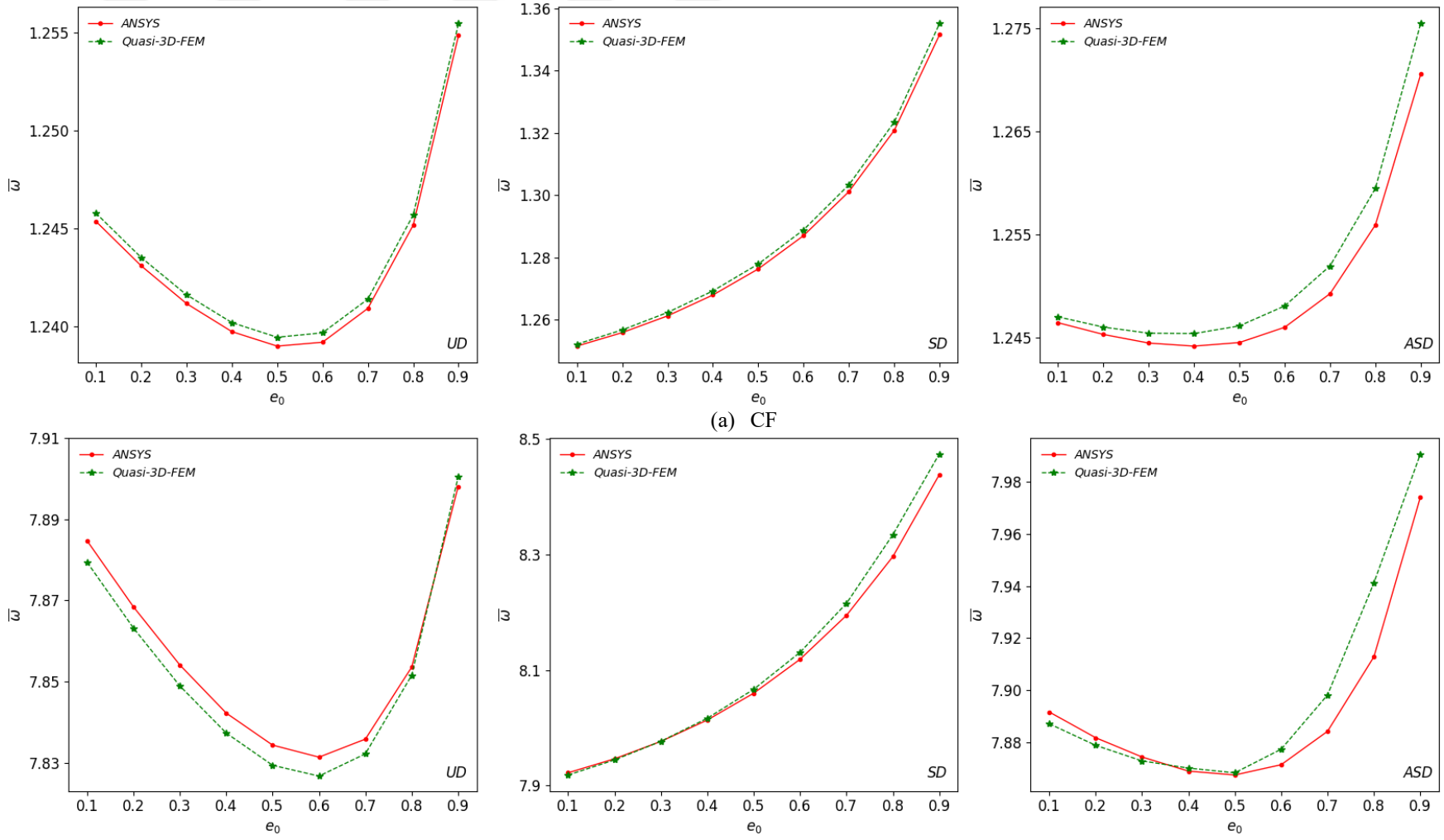

Figure 43. Porosity coefficient effect on fundamental natural frequencies of beams with various porosity distributions (1-2-1, $L/h = 20$, $p = 5$)

4. CONCLUSIONS AND RECOMMENDATIONS

4.1. Conclusions

This thesis presents an in-depth analysis of static, dynamic, and stability characteristics of FGSBs with porous core, supported by a Winkler-Pasternak elastic foundation.

The dissertation began with an overview of FGMs and FGPMs covering briefly their historical development and fundamental concepts. The most commonly used homogenization rules, porosity distributions, theories, and solutions methods for analysis and modeling were also highlighted. An extensive review of recent literature on the mechanical behavior of FGP beam structures was also discussed. The review revealed a limited application of the Ritz method and FEM solutions based on HSNDTs in the analysis of FGSBs. Additionally, it highlights the need for more comprehensive studies on FGSBs with porous core on elastic foundations.

Considering the existing gaps in the literature, this study aimed to comprehensively investigate the combined effects of core porosity and elastic foundation on the free vibration, buckling, and static characteristics of FGSBs with various core configurations. To achieve this, Navier and Ritz-type analytical models and a new FE model based on quasi-3D theory are developed. A power-law function is used to define the gradual variation of material properties across thickness. Three types of porosity patterns in the core are considered: uniform, symmetric, and asymmetric. Additionally, a novel modeling technique for FG sandwich beams with porous cores was introduced using Ansys Mechanical APDL. The accuracy and efficiency of these quasi-3D theory-based solution models in predicting the mechanical responses of FGSBs were demonstrated and validated through comparisons with existing literature, particularly with those based on HSDTs and quasi-3D theories. A comprehensive analysis of various parameters highlighted their impact on FGSBs' performance. Notably, the key findings include:

- Solution models: The proposed quasi-3D theory-based Navier and Ritz-type analytical models, FE and Ansys models predict the mechanical responses of FGSBs with porous cores resting on Winkler-Pasternak elastic foundation more

accurately and efficiently, underscoring the robustness of the developed solution models.

- Material composition: The power-law index significantly influences beam behavior. For ceramic and FG cores, frequencies and buckling loads decrease with increasing power-law index, while the opposite occurs for metal cores. Additionally, vertical displacement increases for ceramic cores.
- Porosity: Porosity significantly influences beam behavior. Higher porosity enhances frequencies and displacements but reduces buckling loads due to reduced stiffness and mass. Symmetric porosity distribution optimizes structural performance.
- Elastic foundation: The Winkler-Pasternak foundation proves beneficial in improving the structural performance of FG sandwich beams by increasing their stiffness and stability, resulting in higher natural frequencies, increased buckling loads, and reduced displacements.

The benchmark results presented in this thesis offer a valuable reference for future research on FGSBs with porous core and their practical applications. These findings can guide the design and optimization of such beams across various engineering fields.

4.2. Recommendations

Although this research offers significant insights into FGSBs with porous core, additional research is necessary to delve deeper into specific areas.

- The current work should be extended to include nonlinear static, dynamic, and stability analysis of these beams. Investigating their performance under dynamic loading conditions, such as impact or cyclic loading, would be valuable for assessing their behavior in more diverse scenarios.
- The foundation effect should be investigated with more sophisticated models, such as the three-parameter Kerr model, to capture the foundation behavior more accurately.
- Mechanical responses of FGSBs with porous core resting on an elastic foundation in a hydro-thermal environment should be explored, considering the potential applications in extreme conditions.

- The behavior of 2D and 3D FGSBs with porous core resting on elastic foundations should be studied.
- Damage detection and evolution in FGSBs with porous core under various loading conditions should be investigated.
- Experimental validation would enhance the understanding of FGSBs with porous core mechanical behavior, complementing existing numerical and analytical results.
- The present thesis can be extended to study the static, dynamic, and stability analysis of other structural elements such as FG sandwich plates and shells with porous core.

5. REFERENCES

Abdelbari, S., Attia, A., Bourada, F., Bousahla, A. A., Tounsi, A., & Ghazwan, M. H. (2023). Investigation of Dynamic Characteristics of Imperfect FG Beams on the Winkler-Pasternak Foundation Under Thermal Loading. *Fizicheskaya Mezomekhanika*, 3. https://doi.org/10.55652/1683-805X_2023_26_3_89

Abed, B., & Anis Bousahla, A. (2022). Investigation of the Mechanical Behavior of Functionally Graded Sandwich Thick Beams. *Steel and Composite Structures*, 44(5), 707–726. https://doi.org/10.12989/scs.2022.44.5.707

Adiyaman, G., & Turan, M. (2024). Bending and Buckling Analysis of Porous 2D Functionally Graded Beams with Exponential Material Property Variation. *Iranian Journal of Science and Technology, Transactions of Civil Engineering*. https://doi.org/10.1007/s40996-024-01508-4

Adıyaman, G. (2022). Free Vibration Analysis of a Porous Functionally Graded Beam Using Higher-Order Shear Deformation Theory. *Journal of Structural Engineering & Applied Mechanics*, 5(4). https://doi.org/10.31462/jseam.2022.04277288

Ahmed, H. M. S., Aicha, B., Tarek, M., Ahmed Amine, D., Aman, G., Abdelouahed, T., A, E. M., & Mohamed-Ouejdi, B. (2024). Shear Correction Factors of a New Exponential Functionally Graded Porous Beams. *Structural Engineering and Mechanics*, 89(1), 1–11. https://doi.org/10.12989/SEM.2024.89.1.001

Ait Atmane, H., Tounsi, A., & Bernard, F. (2017). Effect of Thickness Stretching and Porosity on Mechanical Response of a Functionally Graded Beams Resting on Elastic Foundations. *International Journal of Mechanics and Materials in Design*, 13(1), 71–84. https://doi.org/10.1007/s10999-015-9318-x

Akavci, S. S., & Tanrikulu, A. H. (2008). Buckling and Free Vibration Analyses of Laminated Composite Plates by Using Two New Hyperbolic Shear-Deformation Theories. *Mechanics of Composite Materials*, 44(2), 145–154. https://doi.org/10.1007/s11029-008-9004-2

Akbaş, Ş. D., Fageehi, Y. A., Assie, A. E., & Eltaher, M. A. (2022). Dynamic Analysis of Viscoelastic Functionally Graded Porous Thick Beams Under Pulse Load. *Engineering with Computers*, 38(1), 365–377. https://doi.org/10.1007/s00366-020-01070-3

Alambeigi, K., Mohammadimehr, M., Bamdad, M., & Rabczuk, T. (2020). Free and Forced Vibration Analysis of a Sandwich Beam Considering Porous Core and SMA Hybrid Composite Face Layers on Vlasov's Foundation. *Acta Mechanica*, 231(8), 3199–3218. https://doi.org/10.1007/s00707-020-02697-5

Al-Itbi, S. K., & Noori, A. R. (2022). Finite Element Analysis for the Static Response of Functionally Graded Porous Sandwich Beams. *International Journal of Engineering Technologies IJET*, 8(1), 13–20. https://doi.org/10.19072/ijet.1161612

Alkunte, S., Fidan, I., Naikwadi, V., Gudavasov, S., Ali, M. A., Mahmudov, M., Hasanov, S., & Cheepu, M. (2024). Advancements and Challenges in Additively Manufactured Functionally Graded Materials: A Comprehensive Review. *Journal of Manufacturing and Materials Processing*, 8(1), 23. https://doi.org/10.3390/jmmp8010023

Ambartsumian, S. A. (1960). On the Theory of Bending of Anisotropic Plates and Shallow Shells. *Journal of Applied Mathematics and Mechanics*, 24(2), 500–514. https://doi.org/10.1016/0021-8928(60)90052-6

Amir, M., & Kim, S.W. (2024). A Study of the Natural Frequencies of the Functionally Graded Curved Beams Including Porosities: Deterministic and Stochastic Modeling. *Mechanics Based Design of Structures and Machines*, 52(8), 5970–5987. https://doi.org/10.1080/15397734.2023.2266828

Arefi, M., & Najafitabar, F. (2021). Buckling and Free Vibration Analyses of a Sandwich Beam Made of a Soft Core with FG-GNPS Reinforced Composite Face-Sheets Using Ritz Method. *Thin-Walled Structures*, 158, 107200. https://doi.org/10.1016/j.tws.2020.107200

Arya, H., Shimpi, R. P., & Naik, N. K. (2002). A Zigzag Model for Laminated Composite Beams. *Composite Structures*, 56(1), 21–24. https://doi.org/10.1016/S0263-8223(01)00178-7

Attia, M. A., & Shanab, R. A. (2024). Dynamic Analysis of 2DFGM Porous Nanobeams Under Moving Load with Surface Stress and Microstructure Effects Using Ritz Method. *Acta Mechanica*, 235(1), 1–27. https://doi.org/10.1007/s00707-023-03703-2

Avcar, M., Hadji, L., & Civalek, Ö. (2021). Natural Frequency Analysis of Sigmoid Functionally Graded Sandwich Beams in the Framework of High Order Shear Deformation Theory. *Composite Structures*, 276, 114564. https://doi.org/10.1016/j.compstruct.2021.114564

Babaei, M., Kiarasi, F., Asemi, K., & Hosseini, M. (2022). Functionally Graded Saturated Porous Structures: A Review. *In Journal of Computational Applied Mechanics*, 53(2), 297–308. https://doi.org/10.22059/JCAMECH.2022.342710.719

Bagheri, Z., Fiouz, A., & Seraji, M. (2024). Effect of Porosity on Free Vibration and Buckling of Functionally Graded Porous Beams with Non-Uniform Cross-Section. *Journal of Central South University*, 31(3), 841–857. https://doi.org/10.1007/s11771-023-5302-z

Bamdad, M., Mohammadimehr, M., & Alambeigi, K. (2019). Analysis of Sandwich Timoshenko Porous Beam with Temperature-Dependent Material Properties: Magneto-Electro-Elastic Vibration and Buckling Solution. *Journal of Vibration and Control*, 25(23–24), 2875–2893. https://doi.org/10.1177/1077546319860314

Bang, S.-O., & Cho, J.-U. (2015). A Study on the Compression Property of Sandwich Composite with Porous Core. *International Journal of Precision Engineering and Manufacturing*, 16(6), 1117–1122. https://doi.org/10.1007/s12541-015-0144-8

Belabed, Z., Tounsi, A., Al-Osta, M. A., Tounsi, A., & Minh, H. Le. (2024). On the Elastic Stability and Free Vibration Responses of Functionally Graded Porous Beams Resting on Winkler-Pasternak Foundations Via Finite Element Computation. *Geomechanics and Engineering*, 36(2), 183–204. https://doi.org/10.12989/gae.2024.36.2.183

Belarbi, M.-O., Houari, M. S. A., Hirane, H., Daikh, A. A., & Bordas, S. P. A. (2022). On the Finite Element Analysis of Functionally Graded Sandwich Curved Beams Via a New Refined Higher Order Shear Deformation Theory. *Composite Structures*, 279, 114715. https://doi.org/10.1016/j.compstruct.2021.114715

Belarbi, M.-O., Khechai, A., Bessaim, A., Houari, M.-S.-A., Garg, A., Hirane, H., & Chalak, H. (2021). Finite Element Bending Analysis of Symmetric and Non-Symmetric Functionally Graded Sandwich Beams Using a Novel Parabolic Shear Deformation Theory. *Proceedings of the Institution of Mechanical Engineers, Part L: Journal of Materials: Design and Applications*, 235(11), 2482–2504. https://doi.org/10.1177/14644207211005096

Betts, C. (2012). Benefits of Metal Foams and Developments in Modelling Techniques to Assess Their Materials Behaviour: A Review. *Materials Science and Technology*, 28(2), 129–143. https://doi.org/10.1179/026708311X13135950699290

Bever, M. B., & Duwez, P. E. (1972). Gradients in Composite Materials. *Materials Science and Engineering*, 10, 1–8. https://doi.org/10.1016/0025-5416(72)90059-6

Bhavar, V., Kattire, P., Thakare, S., Patil, S., & Singh, R. (2017). A Review on Functionally Gradient Materials (FGMs) and Their Applications. *IOP Conference Series: Materials Science and Engineering*, 229, 012021. https://doi.org/10.1088/1757-899X/229/1/012021

Birman, V., & Kardomateas, G. A. (2018). Review of Current Trends in Research and Applications of Sandwich Structures. *Composites Part B: Engineering*, 142, 221–240. https://doi.org/10.1016/J.COMPOSITESB.2018.01.027

Burlayenko, V. N., Altenbach, H., & Dimitrova, S. D. (2024). Modal Characteristics of Functionally Graded Porous Timoshenko Beams with Variable Cross-Sections. *Composite Structures*, 342, 118273. https://doi.org/10.1016/j.compstruct.2024.118273

Chen, D., Gao, K., Yang, J., & Zhang, L. (2023). Functionally Graded Porous Structures: Analyses, Performances, and Applications-A Review. *Thin-Walled Structures*, 191, 111046. https://doi.org/10.1016/j.tws.2023.111046

Chen, D., Kitipornchai, S., & Yang, J. (2016). Nonlinear Free Vibration of Shear Deformable Sandwich Beam with a Functionally Graded Porous Core. *Thin-Walled Structures*, 107, 39–48. https://doi.org/10.1016/j.tws.2016.05.025

Chen, D., Kitipornchai, S., & Yang, J. (2018). Dynamic Response and Energy Absorption of Functionally Graded Porous Structures. *Materials & Design*, 140, 473–487. https://doi.org/10.1016/j.matdes.2017.12.019

Chen, D., Rezaei, S., Rosendahl, P. L., Xu, B.-X., & Schneider, J. (2022). Multiscale Modelling of Functionally Graded Porous Beams: Buckling and Vibration Analyses. *Engineering Structures*, 266, 114568. https://doi.org/10.1016/j.engstruct.2022.114568

Chi, S.-H., & Chung, Y.-L. (2006). Mechanical Behavior of Functionally Graded Material Plates Under Transverse Load-Part I: Analysis. *International Journal of Solids and Structures*, 43(13), 3657–3674. https://doi.org/10.1016/j.ijsolstr.2005.04.011

Chinh, T. H., Tu, T. M., Duc, D. M., & Hung, T. Q. (2021). Static Flexural Analysis of Sandwich Beam with Functionally Graded Face Sheets and Porous Core Via Point Interpolation Meshfree Method Based on Polynomial Basic Function. *Archive of Applied Mechanics*, 91(3), 933–947. https://doi.org/10.1007/s00419-020-01797-x

Conde, Y., Pollien, A., & Mortensen, A. (2006). Functional Grading of Metal Foam Cores for Yield-Limited Lightweight Sandwich Beams. *Scripta Materialia*, 54(4), 539–543. https://doi.org/10.1016/j.scriptamat.2005.10.050

Dahmane, M., Benadouda, M., Fellah, A., Saimi, A., Hassen, A. A., & Bensaid, I. (2023). Porosities-Dependent Wave Propagation in Bi-Directional Functionally Graded Cantilever Beam with Higher-Order Shear Model. *Mechanics of Advanced Materials and Structures*, 1–11. https://doi.org/10.1080/15376494.2023.2253546

Delale, F., & Erdogan, F. (1983). The Crack Problem for a Nonhomogeneous Plane. *Journal of Applied Mechanics*, 50(3), 609–614. https://doi.org/10.1115/1.3167098

Demir, E., Çallioğlu, H., & Sayer, M. (2013). Vibration Analysis of Sandwich Beams with Variable Cross Section on Variable Winkler Elastic Foundation. *Sci Eng Compos Mater*, 20(4), 359–370. https://doi.org/10.1515/secm-2012-0151

Derikvand, M., Farhatnia, F., & Hodges, D. H. (2023). Functionally Graded Thick Sandwich Beams with Porous Core: Buckling Analysis Via Differential Transform Method. *Mechanics Based Design of Structures and Machines*, 51(7), 3650–3677. https://doi.org/10.1080/15397734.2021.1931309

Djilali Djebbour, K., Mokhtar, N., Hassen, A. A., Alghanmi, R. A., Hadji, L., & Riadh, B. (2024). An Enhanced Quasi-3D HSDT for Free Vibration Analysis of Porous FG-CNT Beams on a New Concept of Orthotropic VE-Foundations. *Mechanics of Advanced Materials and Structures*, 1–17. https://doi.org/10.1080/15376494.2024.2356728

Eiadtrong, S., Nguyen, T. N., & Wattanasakulpong, N. (2024). Nonlinear Vibration of Sandwich Beams Made of FGM Faces and FGP Core Under Multiple Moving Loads Using a Quasi-3D Theory. *Engineering Structures*, 316, 118575. https://doi.org/10.1016/j.engstruct.2024.118575

El-Galy, I. M., Saleh, B. I., & Ahmed, M. H. (2019). Functionally Graded Materials Classifications and Development Trends from Industrial Point of View. *In SN Applied Sciences*, 1(11). https://doi.org/10.1007/s42452-019-1413-4

Ermis, M., Dorduncu, M., & Kutlu, A. (2024). Peridynamic Differential Operator for Stress Analysis of Imperfect Functionally Graded Porous Sandwich Beams Based on Refined Zigzag Theory. *Applied Mathematical Modelling*, 133, 414–435. https://doi.org/10.1016/j.apm.2024.05.032

Fahsi, B., Bouiadjra, R. B., Mahmoudi, A., Benyoucef, S., & Tounsi, A. (2019). Assessing the Effects of Porosity on the Bending, Buckling, and Vibrations of Functionally Graded Beams Resting on an Elastic Foundation by Using a New Refined Quasi-3D Theory. *Mechanics of Composite Materials*, 55(2), 219–230. https://doi.org/10.1007/s11029-019-09805-0

Fallah, A., & Aghdam, M. M. (2024). Physics-Informed Neural Network for Bending and Free Vibration Analysis of Three-Dimensional Functionally Graded Porous Beam Resting on Elastic Foundation. *Engineering with Computers*, 40(1), 437–454. https://doi.org/10.1007/s00366-023-01799-7

Fang, W., Yu, T., Van Lich, L., & Bui, T. Q. (2019). Analysis of Thick Porous Beams by a Quasi-3D Theory and Isogeometric Analysis. *Composite Structures*, 221, 110890. https://doi.org/10.1016/j.compstruct.2019.04.062

Fazzolari, F. A. (2018). Generalized Exponential, Polynomial and Trigonometric Theories for Vibration and Stability Analysis of Porous FG Sandwich Beams Resting on Elastic Foundations. *Composites Part B: Engineering*, 136, 254–271. https://doi.org/10.1016/j.compositesb.2017.10.022

Ferreira, A. J. M., Roque, C. M. C., & Jorge, R. M. N. (2005). Analysis of Composite Plates by Trigonometric Shear Deformation Theory and Multiquadrics. *Computers & Structures*, 83(27), 2225–2237. https://doi.org/10.1016/j.compstruc.2005.04.002

Garg, A., Belarbi, M.-O., Chalak, H. D., & Chakrabarti, A. (2021). A Review of the Analysis of Sandwich FGM Structures. *Composite Structures*, 258, 113427. https://doi.org/10.1016/j.compstruct.2020.113427

Garg, A., & Chalak, H. D. (2019). A Review on Analysis of Laminated Composite and Sandwich Structures Under Hygrothermal Conditions. *Thin-Walled Structures*, 142, 205–226. https://doi.org/10.1016/j.tws.2019.05.005

Garg, A., Chalak, H. D., Belarbi, M.-O., Chakrabarti, A., & Houari, M.-S.-A. (2021). Finite Element-based Free Vibration Analysis of Power-Law, Exponential and Sigmoidal Functionally Graded Sandwich Beams. *Journal of the Institution of Engineers (India): Series C*, 102(5), 1167–1201. https://doi.org/10.1007/s40032-021-00740-5

Garg, A., Chalak, H. D., & Chakrabarti, A. (2020). Comparative Study on the Bending of Sandwich FGM Beams Made up of Different Material Variation Laws Using Refined Layerwise Theory. *Mechanics of Materials*, 151, 103634. https://doi.org/10.1016/j.mechmat.2020.103634

Geetha, N. K., Bridjesh, P., Yelamasetti, B., Saxena, K. K., & Gupta, N. (2023). Analytical Modelling of a Multifunctional Heterogeneous Beam-Bending Analysis. *Proceedings of the Institution of Mechanical Engineers, Part E: Journal of Process Mechanical Engineering*. https://doi.org/10.1177/09544089231207421

Grover, N., Singh, B. N., & Maiti, D. K. (2013). Analytical and Finite Element Modeling of Laminated Composite and Sandwich Plates: An Assessment of a New Shear Deformation Theory for Free Vibration Response. *International Journal of Mechanical Sciences*, 67, 89–99. https://doi.org/10.1016/j.ijmecsci.2012.12.010

Grygorowicz, M., Magnucki, K., & Malinowski, M. (2015). Elastic Buckling of a Sandwich Beam with Variable Mechanical Properties of the Core. *Thin-Walled Structures*, 87, 127–132. https://doi.org/10.1016/j.tws.2014.11.014

Gupta, A., & Talha, M. (2015). Recent Development in Modeling and Analysis of Functionally Graded Materials and Structures. *Progress in Aerospace Sciences*, 79, 1–14. https://doi.org/10.1016/j.paerosci.2015.07.001

Hadj Mostefa, A., Merdaci, S., & Mahmoudi, N. (2018). An Overview of Functionally Graded Materials «FGM». *In Proceedings of the Third International Symposium on Materials and Sustainable Development*, 267–278. https://doi.org/10.1007/978-3-319-89707-3_30

Hadji, L., Bernard, F., & Zouatnia, N. (2023). Bending and Free Vibration Analysis of Porous-Functionally-Graded (PFG) Beams Resting on Elastic Foundations. *Fluid Dynamics & Materials Processing*, 19(4), 1043–1054. https://doi.org/10.32604/fdmp.2022.022327

Hadji, L., Plevris, V., & Madan, R. (2023). A Static and Free Vibration Analysis of Porous Functionally Graded Beams. *Proceedings of the International Conference on Civil Infrastructure and Construction (CIC)*, 433–441. https://doi.org/10.29117/cic.2023.0059

Hadji, L., Zouatnia, N., & Bernard, F. (2019). An Analytical Solution for Bending and Free Vibration Responses of Functionally Graded Beams with Porosities: Effect of the Micromechanical Models. *Structural Engineering and Mechanics*, 69(2), 231–241. https://doi.org/10.12989/sem.2019.69.2.231

Hamed, M. A., Abo-bakr, R. M., Mohamed, S. A., & Eltaher, M. A. (2020). Influence of Axial Load Function and Optimization on Static Stability of Sandwich Functionally Graded Beams with Porous Core. *Engineering with Computers*, 36(4), 1929–1946. https://doi.org/10.1007/s00366-020-01023-w

Harsha, B. P., Jeyaraj, P., & Lenin, B. M. C. (2021). Effect of Porosity and Profile Axial Loading on Elastic Buckling and Free Vibration of Functionally Graded Porous Beam. *IOP Conference Series: Materials Science and Engineering*, 1128(1), 012025. https://doi.org/10.1088/1757-899X/1128/1/012025

Heshmati, M., Jalali, S. K., & Pugno, N. M. (2024). Wave Propagation in Beams with Functionally Graded Porosity Distribution Under Highly Transient Axial and Transverse Impacts. *Thin-Walled Structures*, 196, 111548. https://doi.org/10.1016/j.tws.2023.111548

Hirai, T. (2006). *Functional Gradient Materials*. In Materials Science and Technology. Wiley. https://doi.org/10.1002/9783527603978.mst0205

Hoang That Ton, L. (2022). Three Kinds of Porosity on Functionally Graded Porous Beams. *Journal of Architectural and Engineering Research*, 2, 28–35. https://doi.org/10.54338/27382656-2022.2-005

Hung, D. X., & Truong, H. Q. (2018). Free Vibration Analysis of Sandwich Beams with FG Porous Core and FGM Faces Resting on Winkler Elastic Foundation by Various Shear Deformation Theories. *Journal of Science and Technology in Civil Engineering (STCE) - NUCE*, 12(3), 23–33. https://doi.org/10.31814/stce.nuce2018-12(3)-03

Hung, T. Q., Tu, T. M., & Duc, D. M. (2022). Free Vibration Analysis of Sandwich Beam with Porous FGM Core in Thermal Environment Using Mesh-Free Approach. *Archive of Mechanical Engineering*, 471–496. https://doi.org/10.24425/ame.2022.140422

K. Wakashima, T. Hiratio, & M. Niino. (1990). Functionally Gradient Materials (FGM) Architecture: A New Type of Ceramic/Metal Assemblage Designed for Hot Structural Components. *International Symposium on Space Applications of Advanced Structural Materials*, 97–103.

Kahya, V., & Turan, M. (2018). Vibration and Stability Analysis of Functionally Graded Sandwich Beams by a Multi-Layer Finite Element. *Composites Part B: Engineering*, 146, 198–212. https://doi.org/10.1016/j.compositesb.2018.04.011

Karama, M., Afaq, K. S., & Mistou, S. (2009). A New Theory for Laminated Composite Plates. *Proceedings of the Institution of Mechanical Engineers, Part L: Journal of Materials: Design and Applications*, 223(2), 53–62. https://doi.org/10.1243/14644207JMDA189

Karamanli, A., & Aydogdu, M. (2020). Free Vibration and Buckling Analysis of Laminated Composites and Sandwich Microbeams Using a Transverse Shear-Normal Deformable Beam Theory. *Journal of Vibration and Control*, 26(3–4), 214–228. https://doi.org/10.1177/1077546319878538

Karamanlı, A. (2018). Bending Analysis of Composite and Sandwich Beams Using Ritz Method. *Anadolu University Journal of Science and Technology A - Applied Sciences and Engineering*, 1–1. https://doi.org/10.18038/aubtda.320144

Kiarasi, F., Babaei, M., Sarvi, P., Asemi, K., Hosseini, M., & Bidgoli, M. O. (2021). A Review on Functionally Graded Porous Structures Reinforced by Graphene Platelets. *In Journal of Computational Applied Mechanics*, 52(4), 731–750. https://doi.org/10.22059/JCAMECH.2021.335739.675

Kneifati, M. C. (1985). Analysis of Plates on a Kerr Foundation Model. *Journal of Engineering Mechanics*, 111(11), 1325–1342. https://doi.org/10.1061/(ASCE)0733-9399(1985)111:11(1325)

Koutoati, K., Mohri, F., & Daya, E. M. (2021). Finite Element Approach of Axial Bending Coupling on Static and Vibration Behaviors of Functionally Graded Material Sandwich Beams. *Mechanics of Advanced Materials and Structures*, 28(15), 1537–1553. https://doi.org/10.1080/15376494.2019.1685144

Kruszewski, E. T. (1949). *Effect of Transverse Shear and Rotary Inertia on the Natural Frequency of a Uniform Beam*. National Advisory Committee for Aeronautics.

Kumar, P., & Harsha, S. P. (2022). Static Analysis of Porous Core Functionally Graded Piezoelectric (PCFGP) Sandwich Plate Resting on the Winkler/Pasternak/Kerr Foundation Under Thermo-Electric Effect. *Materials Today Communications*, 32, 103929. https://doi.org/10.1016/j.mtcomm.2022.103929

Levinson, M. (1980). An Accurate, Simple Theory of the Statics and Dynamics of Elastic Plates. *Mechanics Research Communications*, 7(6), 343–350. https://doi.org/10.1016/0093-6413(80)90049-X

Li, C., Shen, H.-S., & Yang, J. (2023). Nonlinear Vibration Behavior of FG Sandwich Beams with Auxetic Porous Copper Core in Thermal Environments. *International Journal of Structural Stability and Dynamics*, 23(13). https://doi.org/10.1142/S0219455423501444

Li, P. P., Sluijsmans, M. J. C., Brouwers, H. J. H., & Yu, Q. L. (2020). Functionally Graded Ultra-High Performance Cementitious Composite with Enhanced Impact Properties. *Composites Part B: Engineering*, 183, 107680. https://doi.org/10.1016/j.compositesb.2019.107680

Li, W., Ma, H., & Gao, W. (2019). A Higher-Order Shear Deformable Mixed Beam Element Model for Accurate Analysis of Functionally Graded Sandwich Beams. *Composite Structures*, 221, 110830. https://doi.org/10.1016/j.compstruct.2019.04.002

Li, Y., Feng, Z., Hao, L., Huang, L., Xin, C., Wang, Y., Bilotti, E., Essa, K., Zhang, H., Li, Z., Yan, F., & Peijs, T. (2020). A Review on Functionally Graded Materials and Structures Via Additive Manufacturing: From Multi-Scale Design to Versatile Functional Properties. *Advanced Materials Technologies*, 5(6). https://doi.org/10.1002/admt.201900981

Liu, G. R., & Quek, S. S. (2014). Computational Modeling. *In the Finite Element Method*, 1–11. https://doi.org/10.1016/B978-0-08-098356-1.00001-1

Magnucka-Blandzi, E., & Magnucki, K. (2007). Effective Design of a Sandwich Beam with a Metal Foam Core. *Thin-Walled Structures*, 45(4), 432–438. https://doi.org/10.1016/j.tws.2007.03.005

Mahi, A., Adda Bedia, E. A., & Tounsi, A. (2015). A New Hyperbolic Shear Deformation Theory for Bending and Free Vibration Analysis of Isotropic, Functionally Graded, Sandwich and Laminated Composite Plates. *Applied Mathematical Modelling*, 39(9), 2489–2508. https://doi.org/10.1016/j.apm.2014.10.045

Matinfar, M., Shirazi, M. M., & Alipour, M. M. (2019). Analysis of Bi-Directional FG Porous Sandwich Beams in Hygrothermal Environment Resting on Winkler/Pasternak Foundation, Based on the Layerwise Theory and Cheb-Yshev Tau Method. *Journal of Stress Analysis*, 4(1). https://doi.org/10.22084/jrstan.2019.18781.1090

Medjdoubi, B. A., Houari, M. S. A., Sadoun, M., Bessaim, A., Daikh, A. A., Belarbi, M. O., Khechai, A., Garg, A., & Ghazwani, M. H. (2023). On the Effect of Porosity on the Shear Correction Factors of Functionally Graded Porous Beams. *Coupled Systems Mechanics*, 12(3), 199–220. https://doi.org/10.12989/csm.2023.12.3.199

Mellal, F., Bennai, R., Avcar, M., Nebab, M., & Atmane, H. A. (2023). On the Vibration and Buckling Behaviors of Porous FG Beams Resting on Variable Elastic Foundation Utilizing Higher-Order Shear Deformation Theory. *Acta Mechanica*, 234(9), 3955–3977. https://doi.org/10.1007/s00707-023-03603-5

Mesmoudi, S., Hilali, Y., Rammane, M., Askour, O., & Bourihane, O. (2023). Highly Efficient Mesh-Free Approach to Simulate the Non-Linear Bending Analysis of FG Porous Beams and Sandwich Beams with FG Face Sheets. *Thin-Walled Structures*, 185. https://doi.org/10.1016/j.tws.2023.110614

Mesmoudi, S., Rammane, M., Hilali, Y., Askour, O., & Bourihane, O. (2023). Efficient Buckling and Post-Buckling Analysis of Porous FG Sandwich Beams by New RPIM-HOCM Mesh-Free Approach. *Engineering Structures*, 296, 116951. https://doi.org/10.1016/j.engstruct.2023.116951

Mohammadimehr, M. (2022). Buckling and Bending Analyses of a Sandwich Beam Based on Nonlocal Stress-Strain Elasticity Theory with Porous Core and Functionally Graded Facesheets. *Advances in Materials Research (South Korea)*, 11(4), 279–298. https://doi.org/10.12989/amr.2022.11.4.279

Murthy, M. V. V. (1903). *An Improved Transverse Shear Deformation Theory for Laminated Anisotropic Plates*. National Aeronautics and Space Administration, Scientific and Technical Information Branch.

N. K., G., B., V., Makgato, S., & Pappula, B. (2023). FGP Beam Using Higher Order Shear Deformation Theory - Numerical Vibrational Analysis. *In Theory and Applications of Engineering Research*,1 1–12. https://doi.org/10.9734/bpi/taer/v1/1860G

Naebe, M., & Shirvanimoghaddam, K. (2016). Functionally Graded Materials: A Review of Fabrication and Properties. *Applied Materials Today*, 5, 223–245. https://doi.org/10.1016/j.apmt.2016.10.001

Narayanan Kannaiyan, G., Balasubramaniam, V., Pappula, B., & Makgato, S. (2024). Novel Kuhn-Tucker Conditions for Vibration Analysis in a Functionally Graded Porous Beam Using the R-Program. *Results in Engineering*, 22, 102064. https://doi.org/10.1016/j.rineng.2024.102064

Nguyen, N.-D., Nguyen, T.-N., Nguyen, T.-K., & Vo, T. P. (2022). A New Two-Variable Shear Deformation Theory for Bending, Free Vibration and Buckling Analysis of Functionally Graded Porous Beams. *Composite Structures*, 282, 115095. https://doi.org/10.1016/j.compstruct.2021.115095

Nguyen, N.-D., Nguyen, T.-N., Nguyen, T.-K., & Vo, T. P. (2023). A Legendre-Ritz Solution for Bending, Buckling and Free Vibration Behaviours of Porous Beams Resting on the Elastic Foundation. *Structures*, 50, 1934–1950. https://doi.org/10.1016/j.istruc.2023.03.018

Nguyen, T.-K., Truong-Phong Nguyen, T., Vo, T. P., & Thai, H.-T. (2015). Vibration and Buckling Analysis of Functionally Graded Sandwich Beams by a New Higher-Order Shear Deformation Theory. *Composites Part B: Engineering*, 76, 273–285. https://doi.org/10.1016/j.compositesb.2015.02.032

Nguyen, T.-K., Vo, T. P., Nguyen, B.-D., & Lee, J. (2016). An Analytical Solution for Buckling and Vibration Analysis of Functionally Graded Sandwich Beams Using a Quasi-3D Shear Deformation Theory. *Composite Structures*, 156, 238–252. https://doi.org/10.1016/j.compstruct.2015.11.074

Nguyen, V.-H., Nguyen, T.-K., Thai, H.-T., & Vo, T. P. (2014). A New Inverse Trigonometric Shear Deformation Theory for Isotropic and Functionally Graded Sandwich Plates. *Composites Part B: Engineering*, 66, 233–246. https://doi.org/10.1016/j.compositesb.2014.05.012

Nguyen-Xuan, H., Thai, C. H., & Nguyen-Thoi, T. (2013). Isogeometric Finite Element Analysis of Composite Sandwich Plates Using a Higher Order Shear Deformation Theory. *Composites Part B: Engineering*, 55, 558–574. https://doi.org/10.1016/j.compositesb.2013.06.044

Njim, E. K., Bakhy, S. H., & Al-Waily, M. (2022). Analytical and Numerical Flexural Properties of Polymeric Porous Functionally Graded (PFGM) Sandwich Beams. *Journal of Achievements in Materials and Manufacturing Engineering*, 110(1), 5–15. https://doi.org/10.5604/01.3001.0015.7026

Ong, O. Z. S., Ghayesh, M. H., & Losic, D. (2023). Vibrations of Porous Functionally Graded CNT Reinforced Viscoelastic Beams Connected Via a Viscoelastic Layer. *International Journal of Engineering Science*, 191, 103917. https://doi.org/10.1016/j.ijengsci.2023.103917

Osofero, A. I., Vo, T. P., Nguyen, T.-K., & Lee, J. (2016). Analytical Solution for Vibration and Buckling of Functionally Graded Sandwich Beams Using Various Quasi-3D Theories. *Journal of Sandwich Structures & Materials*, 18(1), 3–29. https://doi.org/10.1177/1099636215582217

Panc, V. (1975). *Theories of Elastic Plates*. Springer Science & Business Media.

Pasternak, P. L. (1954). On a New Method of Analysis of an Elastic Foundation by Means of Two Foundation Constants. *Gos. Izd. Lit. po Strait I Arkh*.

Patel, P., Bhingole, P. P., & Makwana, D. (2018). Manufacturing, Characterization and Applications of Lightweight Metallic Foams for Structural Applications: Review. *Materials Today: Proceedings*, 5(9), 20391–20402. https://doi.org/10.1016/j.matpr.2018.06.414

Patil, R., Joladarashi, S., & Kadoli, R. (2023). Bending and Vibration Studies of FG Porous Sandwich Beam with Viscoelastic Boundary Conditions: FE Approach. *Mechanics of Advanced Materials and Structures*, 30(17), 3588–3607. https://doi.org/10.1080/15376494.2022.2079030

Pham, Q.-H., Tran, V. K., & Nguyen, P.-C. (2023). Nonlocal Strain Gradient Finite Element Procedure for Hygro-Thermal Vibration Analysis of Bidirectional Functionally Graded Porous Nanobeams. *Waves in Random and Complex Media*, 1–32. https://doi.org/10.1080/17455030.2023.2186708

Priyanka, R., Twinkle, C. M., & Pitchaimani, J. (2022). Stability and Dynamic Behavior of Porous FGM Beam: Influence of Graded Porosity, Graphene Platelets, and Axially Varying Loads. *Engineering with Computers*, 38(S5), 4347–4366. https://doi.org/10.1007/s00366-021-01478-5

Rasooli, H., Noori, A. R., & Temel, B. (2024). Static Analysis of Functionally Graded Porous Beam-Column Frames by the Complementary Functions Method. *Structures*, 62, 106136. https://doi.org/10.1016/j.istruc.2024.106136

Reddy, J. N. (1984). A Simple Higher Order Theory for Laminated Composite Plates. *ASME Journal of Applied Mechanics*, 51, 745–752.

Reissner, E. (1975). On Transverse Bending of Plates, Including the Effect of Transverse Shear Deformation. *International Journal of Solids and Structures*, 11(5), 569–573. https://doi.org/10.1016/0020-7683(75)90030-X

Rezaiee-Pajand, M., Masoodi, A. R., & Mokhtari, M. (2018). Static Analysis of Functionally Graded Non-Prismatic Sandwich Beams. *Advances in Computational Design*, 3(2), 165–190. https://doi.org/10.12989/acd.2018.3.2.165

Saleh, B., Jiang, J., Fathi, R., Al-hababi, T., Xu, Q., Wang, L., Song, D., & Ma, A. (2020). 30 Years of Functionally Graded Materials: An Overview of Manufacturing Methods, Applications and Future Challenges. *Composites Part B: Engineering*, 201, 108376. https://doi.org/10.1016/J.COMPOSITESB.2020.108376

Saleh, B., Jiang, J., Ma, A., Song, D., Yang, D., & Xu, Q. (2020). Review on the Influence of Different Reinforcements on the Microstructure and Wear Behavior of Functionally Graded Aluminum Matrix Composites by Centrifugal Casting. *In Metals and Materials International*, 26(7), 933–960. https://doi.org/10.1007/s12540-019-00491-0

Sayyad, A. S., & Avhad, P. V. (2019). On Static Bending, Elastic Buckling and Free Vibration Analysis of Symmetric Functionally Graded Sandwich Beams. *Journal of Solid Mechanics*, 11(1), 166–180. https://doi.org/10.22034/JSM.2019.664227

Sayyad, A. S., Avhad, P. V., & Hadji, L. (2022). On the Static Deformation and Frequency Analysis of Functionally Graded Porous Circular Beams. *Forces in Mechanics*, 7, 100093. https://doi.org/10.1016/j.finmec.2022.100093

Sayyad, A. S., & Ghugal, Y. M. (2019a). A Sinusoidal Beam Theory for Functionally Graded Sandwich Curved Beams. *Composite Structures*, 226, 111246. https://doi.org/10.1016/j.compstruct.2019.111246

Sayyad, A. S., & Ghugal, Y. M. (2019b). Modeling and Analysis of Functionally Graded Sandwich Beams: A Review. *Mechanics of Advanced Materials and Structures*, 26(21), 1776–1795. https://doi.org/10.1080/15376494.2018.1447178

Sayyad, A. S., Shinde, B. M., Shinde, B. M., & Sayyad, A. S. (2017). A Quasi-3D Polynomial Shear and Normal Deformation Theory for Laminated Composite, Sandwich, and Functionally Graded Beams. *Mechanics of Advanced Composite Structures*, 4, 139–152. https://doi.org/10.22075/MACS.2017.10806.1105

Shen, M., & Bever, M. B. (1972). Gradients in Polymeric Materials. *Journal of Materials science*, *7*, 741-746. https://doi.org/10.1007/BF00549902

Smith, B. H., Szyniszewski, S., Hajjar, J. F., Schafer, B. W., & Arwade, S. R. (2012). Steel Foam for Structures: A Review of Applications, Manufacturing and Material Properties. *Journal of Constructional Steel Research*, 71, 1–10. https://doi.org/10.1016/j.jcsr.2011.10.028

Soldatos, K. (1992). A Transverse Shear Deformation Theory for Homogeneous Monoclinic Plates. *Acta Mechanica*, *94*(3), 195-220. https://doi.org/10.1007/BF01176650

Soltani, M., & Asgarian, B. (2019). New Hybrid Approach for Free Vibration and Stability Analyses of Axially Functionally Graded Euler-Bernoulli Beams with Variable Cross-Section Resting on Uniform Winkler-Pasternak Foundation. *Latin American Journal of Solids and Structures*, 16(3). https://doi.org/10.1590/1679-78254665

Srikarun, B., Songsuwan, W., & Wattanasakulpong, N. (2021). Linear and Nonlinear Static Bending of Sandwich Beams with Functionally Graded Porous Core Under Different Distributed Loads. *Composite Structures*, 276, 114538. https://doi.org/10.1016/j.compstruct.2021.114538

Stein, M. (1986). Nonlinear Theory for Plates and Shells Including the Effects of Transverse Shearing. *AIAA Journal*, 24(9), 1537–1544. https://doi.org/10.2514/3.9477

Su, J., Xiang, Y., Ke, L.-L., & Wang, Y.-S. (2019). Surface Effect on Static Bending of Functionally Graded Porous Nanobeams Based on Reddy's Beam Theory. *International Journal of Structural Stability and Dynamics*, 19(06), 1950062. https://doi.org/10.1142/S0219455419500627

Taleb, O., Sekkal, M., Bouiadjra, R. B., Benyoucef, S., Khedher, K. M., Salem, M. A., & Tounsi, A. (2024). On the Free Vibration Behavior of Temperature-Dependent Bidirectional Functionally Graded Curved Porous Beams. *International Journal of Structural Stability and Dynamics*, 24(10). https://doi.org/10.1142/S0219455424501128

Taşkin, M., & Demir, Ö. (2023). Effect of Porosity Distribution on Vibration and Damping Behavior of Inhomogeneous Curved Sandwich Beams with Fractional Derivative Viscoelastic Core. *Engineering Computations*, 40(3), 538–563. https://doi.org/10.1108/EC-04-2022-0269

To, L. H. T. (2022). Effect of Porosity on Free Vibration of Functionally Graded Porous Beam Based on Simple Beam Theory. *Technical Journal of Daukeyev University*, 2(1), 1–10. https://doi.org/10.52542/tjdu.2.1.1-10

Turan, M., & Adiyaman, G. (2023). A New Higher-Order Finite Element for Static Analysis of Two-Directional Functionally Graded Porous Beams. *Arabian Journal for Science and Engineering*. https://doi.org/10.1007/s13369-023-07742-8

Turan, M., & Kahya, V. (2021). Fonksiyonel Derecelendirilmiş Sandviç Kirişlerin Navier Yöntemiyle Serbest Titreşim ve Burkulma Analizi. *Gazi Üniversitesi Mühendislik Mimarlık Fakültesi Dergisi*, 36(2), 743–758. https://doi.org/10.17341/gazimmfd.599928

Turan, M., Uzun Yaylacı, E., & Yaylacı, M. (2023). Free Vibration and Buckling of Functionally Graded Porous Beams Using Analytical, Finite Element, and Artificial Neural Network Methods. *Archive of Applied Mechanics*, 93(4), 1351–1372. https://doi.org/10.1007/s00419-022-02332-w

Uzun, B., & Yayli, M. Ö. (2024). Porosity and Deformable Boundary Effects on the Dynamic of Nonlocal Sigmoid and Power-Law FG Nanobeams Embedded in the Winkler–Pasternak Medium. *Journal of Vibration Engineering and Technologies*, 12(3), 3193–3212. https://doi.org/10.1007/s42417-023-01039-8

Uzun, B., & Yaylı, M. Ö. (2024). Porosity Effects on the Dynamic Response of Arbitrary Restrained FG Nanobeam Based on the MCST. *Zeitschrift Für Naturforschung A*, 79(2), 183–197. https://doi.org/10.1515/zna-2023-0261

Van Vinh, P. (2021). Static Bending Analysis of Functionally Graded Sandwich Beams Using a Novel Mixed Beam Element Based on First-Order Shear Deformation Theory. *Forces in Mechanics*, 4, 100039. https://doi.org/10.1016/j.finmec.2021.100039

Van Vinh, P., Duoc, N. Q., & Phuong, N. D. (2022). A New Enhanced First-Order Beam Element Based on Neutral Surface Position for Bending Analysis of Functionally Graded Porous Beams. *Iranian Journal of Science and Technology, Transactions of Mechanical Engineering*, 46(4), 1141–1156. https://doi.org/10.1007/s40997-022-00485-1

Vikrant, R., & Sarangi, S. K. (2024). Analysis of Elastic Buckling and Static Bending Properties of Smart Functionally Graded Porous Beam. *Recent Patents on Mechanical Engineering*, 17. https://doi.org/10.2174/0122127976316874240702072614

Vo, T. P., Osofero, A. I., Corradi, M., & Inam, F. (2014). Free Vibration of Axially Loaded Functionally Graded Sandwich Beams Using Refined Shear Deformation Theory. *In ECCM-16th European Conference on Composite Materials*.

Vo, T. P., Thai, H.-T., Nguyen, T.-K., Inam, F., & Lee, J. (2015a). A Quasi-3D Theory for Vibration and Buckling of Functionally Graded Sandwich Beams. *Composite Structures*, 119, 1–12. https://doi.org/10.1016/j.compstruct.2014.08.006

Vo, T. P., Thai, H.-T., Nguyen, T.-K., Inam, F., & Lee, J. (2015b). Static Behaviour of Functionally Graded Sandwich Beams Using a Quasi-3D Theory. *Composites Part B: Engineering*, 68, 59–74. https://doi.org/10.1016/j.compositesb.2014.08.030

Vo, T. P., Thai, H.-T., Nguyen, T.-K., Maheri, A., & Lee, J. (2014). Finite Element Model for Vibration and Buckling of Functionally Graded Sandwich Beams Based on a Refined Shear Deformation Theory. *Engineering Structures*, 64, 12–22. https://doi.org/10.1016/j.engstruct.2014.01.029

Winkler, E. (1867). Theory of Elasticity and Strength. *Dominicus Prague*, *36*.

Wu, H., Yang, J., & Kitipornchai, S. (2020). Mechanical Analysis of Functionally Graded Porous Structures: A Review. *In International Journal of Structural Stability and Dynamics*, 20 (13). https://doi.org/10.1142/S0219455420410151

Wu, S., Li, Y., Bao, Y., Zhu, J., & Wu, H. (2024). Examination of Beam Theories for Buckling and Free Vibration of Functionally Graded Porous Beams. *Materials*, 17(13), 3080. https://doi.org/10.3390/ma17133080

Xin, L., & Kiani, Y. (2023). Vibration Characteristics of Arbitrary Thick Sandwich Beam with Metal Foam Core Resting on Elastic Medium. *Structures*, 49, 1–11. https://doi.org/10.1016/j.istruc.2023.01.108

Yang, Q., B. Zheng, B., & Zhu, J. (2013). Analytical Solution of a Bilayer Functionally Graded Cantilever Beam with Concentrated Loads. *Archive of Applied Mechanics*, 83, 455–466. https://doi.org/10.1007/s00419-012-0693-6

Zghal, S., Ataoui, D., & Dammak, F. (2022). Static Bending Analysis of Beams Made of Functionally Graded Porous Materials. *Mechanics Based Design of Structures and Machines*, 50(3), 1012–1029. https://doi.org/10.1080/15397734.2020.1748053

Zhang, Ch., Savaidis, A., Savaidis, G., & Zhu, H. (2003). Transient Dynamic Analysis of a Cracked Functionally Graded Material by a BIEM. *Computational Materials Science*, 26, 167–174. https://doi.org/10.1016/S0927-0256(02)00395-6

Zhang, N., Khan, T., Guo, H., Shi, S., Zhong, W., & Zhang, W. (2019). Functionally Graded Materials: An Overview of Stability, Buckling, and Free Vibration Analysis. *Advances in Materials Science and Engineering*, 2019, 1–18. https://doi.org/10.1155/2019/1354150

Zhang, Q., Zhang, R., Su, J., & Jiang, Y. (2023). A Unified Variational Method for Vibration of Functionally Graded Porous Beams with Variable Curvature Under Arbitrary Boundary Condition. *Engineering Structures*, 284, 115948. https://doi.org/10.1016/j.engstruct.2023.115948

Zhang, Y., Li, Y., & Li, S. (2024). Free Vibration of Porous FG Magneto-Electro-Elastic Microbeams in the Hygrothermal Environment Based on Differential Transformation Method. *Journal of Intelligent Material Systems and Structures*, 35(3), 253–269. https://doi.org/10.1177/1045389X231197731

RESUME

Ibrahim Ali Mohamed completed his primary, secondary, and high school education in Djibouti. He earned a master's degree in civil engineering from the University of Djibouti, Faculty of Engineering, in 2020. Following his graduation, he gained valuable professional experience as a site engineer, working with private construction companies from 2020 to 2021. In 2021, Ibrahim embarked on his doctoral studies in Civil Engineering at Karadeniz Technical University, in Trabzon, Turkey.

Articles Published in Web of Science-Indexed Journals Derived from the Dissertation

Mohamed, I., Şimşek, S., Kahya, V., & Lanc, D. (2025). Computational Modeling of Functionally Graded Sandwich Beams with Porous Core Using an Ansys APDL-Based Approach. *Mechanics Based Design of Structures and Machines*, 1–22. https://doi.org/10.1080/15397734.2024.2448715

Mohamed, I., Kahya, V., & Şimşek, S. (2024). Finite Element Static Analysis of Functionally Graded Sandwich Beams with Porous Core Resting on a Two-Parameter Elastic Foundation Based on Quasi-3D Theory. *Proceedings of the Institution of Mechanical Engineers, Part C: Journal of Mechanical Engineering Science*. https://doi.org/10.1177/09544062241297120

Mohamed, I., Kahya, V., & Şimşek, S. (2024). A New Higher-Order Finite Element Model for Free Vibration and Buckling of Functionally Graded Sandwich Beams with Porous Core Resting on a Two-Parameter Elastic Foundation Using Quasi-3D Theory. *Iranian Journal of Science and Technology, Transactions of Civil Engineering*. https://doi.org/10.1007/s40996-024-01482-x

Mohamed, I., Kahya, V., & Şimşek, S. (2024). Ritz-Type Quasi-3D Solution for Free Vibration and Buckling of Functionally Graded Sandwich Beams with Porous Core Resting on a Two-Parameter Elastic Foundation. *Arabian Journal for Science and Engineering*. https://doi.org/10.1007/s13369-024-09729-5

Mohamed, I., Şimşek, S., & Kahya, V. (2025). Free Vibration and Buckling Analysis of Functionally Graded Sandwich Beams Resting on A Two-Parameter Elastic Foundation Using A Quasi-3D Theory. *Sigma J Eng Nat Sci;* 43(1): 47-61